2000

Perturbative Quantum Chromodynamics Predictions for Very High Energy Atmospheric Neutrinos and Muons

Gabriele U. Varieschi
Loyola Marymount University, gvarieschi@lmu.edu

UNIVERSITY OF CALIFORNIA

Los Angeles

Perturbative Quantum Chromodynamics Predictions for Very High Energy Atmospheric Neutrinos and Muons

A dissertation submitted in partial satisfaction of the requirements for the degree Doctor of Philosophy in Physics

by

Gabriele Umberto Varieschi

2000

Contents

List of Figures

List of Tables

ACKNOWLEDGEMENTS

My deepest thanks and gratitude go to Professor Graciela B. Gelmini and Dr. Paolo Gondolo. Prof. Gelmini patiently and carefully guided me through many interesting topics, as early as my second year in graduate school. She is chiefly responsible for formulating my research project which eventually became this dissertation. Dr. Gondolo is the main motivator of many of the ideas behind this dissertation. Their constant attention and great spirit have helped me overcome many obstacles in the course of my work. I truly thank my thesis advisors for showing me clearly both the spirit and the practice of scientific research. Chapter Two is a version of "Prompt atmospheric neutrinos and muons: NLO versus LO QCD predictions", G. Gelmini, P. Gondolo, and G. Varieschi, Phys. Rev. D61, 036005, 2000. Chapter Three is a version of "Prompt atmospheric neutrinos and muons: Dependence on the gluon distribution function", G. Gelmini, P. Gondolo, and G. Varieschi, Phys. Rev. D61, 056011, 2000. Chapter Four is a version of "Measurement of the gluon PDF at small x with neutrino telescopes", G. Gelmini, P. Gondolo, and G. Varieschi, preprint hep-ph/0003307, submitted to Phys. Rev. D. This research was supported in part by the US Department of Energy under grant DE-FG03-91ER40662 Task C.

VITA

November 18, 1961	Born, Milano, Italy
1989	B.S., Physics University of Milano, Italy
1996	M.S., Physics University of California, Los Angeles
1994–1998	Teaching Assistant Department of Physics and Astronomy University of California, Los Angeles
1998–2000	Research Assistant Department of Physics and Astronomy University of California, Los Angeles

PUBLICATIONS

Graciela Gelmini, Paolo Gondolo, and Gabriele Varieschi, "Prompt atmospheric neutrinos and muons: NLO versus LO QCD predictions", Phys. Rev. D61, 036005 (2000).

Graciela Gelmini, Paolo Gondolo, and Gabriele Varieschi, "Prompt atmospheric neutrinos and muons: Dependence on the gluon distribution function", Phys. Rev. D61, 056011 (2000).

ABSTRACT OF THE DISSERTATION

Perturbative Quantum Chromodynamics Predictions for Very High Energy Atmospheric Neutrinos and Muons

by

Gabriele Umberto Varieschi

Doctor of Philosophy in Physics

University of California, Los Angeles, 2000

Professor Graciela B. Gelmini, Chair

We compare the leading and next-to-leading order Quantum Chromodynamics predictions for the flux of atmospheric muons and neutrinos from decays of charmed particles. We then compute this flux for different Partonic Distribution Functions (PDF's) and different extrapolations of these at small partonic momentum fraction x. We find that the predicted fluxes vary up to almost two orders of magnitude at the largest energies studied, depending on the chosen extrapolation of the PDF's. We show that the spectral index of the atmospheric leptonic fluxes depends linearly on the slope of the gluon distribution function at very small x. Finally, we analyze the uncertainties of our model and we consider the dependence of our simulation on the primary cosmic ray flux.

Chapter 1

Introduction

Atmospheric neutrinos and muons are the result of interactions of primary cosmic rays in the atmosphere. These usually generate a large number of secondary particles, which subsequently interact and decay, while streaming down in the atmosphere, creating very complex particle cascades with a large number of muons and neutrinos that can reach sea level and eventually penetrate throughout our planet.

The flux of these atmospheric leptons is the most important source of background for present and future "neutrino telescopes", which are supposed to open soon a new window in astronomy by detecting neutrinos from astrophysical sources like Active Galactic Nuclei and others. The current and future projects for these types of detector arrays, like AMANDA [1], Baikal [2], NESTOR [3] and ANTARES [4], will ultimately reach the km^3 volume of detection, allowing to observe neutrinos and muons at energies as high as $10^{12}\ GeV$. To evaluate the atmospheric background at energies above 1 TeV, it is necessary to consider the "prompt" component of this flux, i.e. the neutrinos (and muons) created from semileptonic decays of charmed particles, as opposed to the "conventional" neutrinos coming from decays of pions and kaons. The purpose of this dissertation is to produce a state-of-the-art evalu-

ation of the atmospheric "prompt" flux, which might be interesting not only as a background for neutrino telescopes, but also to address specific problems of High Energy Particle Physics. To achieve this objective we have implemented a full computer simulation of the particle cascades in the atmosphere, which is based on the following points.

- We have built our model on the general framework of the existing TIG model (after Thunman, Ingelman and Gondolo, 1996) which was the first to employ perturbative Quantum Chromodynamics (pQCD) for the charm production model, but only at leading-order (LO). We have kept the general approach of TIG to the modeling of the primary cosmic ray flux, of the atmosphere and of the cascade evolution.

- We have completely redesigned the simulation of charm production in the atmosphere, implementing the full next-to-leading order (NLO) pQCD calculations of M. Mangano, P. Nason and G. Ridolfi (MNR model and computer program).

- We have included particular features in the charm production module, related to important issues of Particle Physics. In particular all the NLO processes can be calculated using the most recent Partonic Distribution Functions (PDF's), like the CTEQ or MRS sets. Also, for our extreme energies, we needed extrapolations of these PDF's beyond experimental ranges: for the gluon PDF (by far the most important) we have implemented the extrapolation at very low momentum fraction x ($x \leq 10^{-5}$) as $x \cdot g(x) \sim x^{-\lambda}$, where λ can be varied in the theoretically reasonable interval between 0 and 0.5 . The determination of λ, which is not known experimentally, is a critical issue in Quantum Chromodynamics.

- Following the charm production module, we have included a full simulation of particle cascades, done with the PYTHIA program, which handles parton shower evolution, hadronization, interactions and decays, down to the final leptons. Several runs of the program have produced fluxes consistent with previous calculations, for the "prompt" component, existing in the literature and have tested different options and features of our model.

We subdivide our analysis in four main parts corresponding to the following chapters.

Part One (Chapter 2): NLO versus LO QCD Predictions.

We describe here how we calibrate our model for charm production. We use the most recent experimental data of total and differential cross sections to determine the best choice of QCD parameters and PDF's, needed in our program to extrapolate the cross sections beyond the range accessible to accelerator physics. We give full details of our simulation, including the model for the primary cosmic rays, the atmosphere, charm production and cascade evolution, describing different possible operative modes and arguing the reliability of the different options. We then show the results for the lepton fluxes, comparing in particular the difference between a LO and a NLO calculation.

Part Two (Chapter 3): Dependence on the Gluon Distribution Function.

We consider the existing possible theoretical extrapolations of the gluon PDF at very low x and we discuss how the leptonic fluxes are affected by such choice, which is related to the value of the parameter λ. We then justify theoretically the results obtained. From a detailed analysis of the dominant process, the gluon fusion, we derive the dependence of the charm and leptonic fluxes on λ and, from this analysis, we notice the possibility of measuring λ with neutrino telescopes.

Part Three (Chapter 4): Error Analysis and Measurement of the Gluon PDF at very low x.

We consider all possible sources of uncertainty, concentrating in particular on the charm production model. We estimate the overall errors on cross sections and fluxes. Using this error analysis, we return in more detail on the possibility of an experimental measure of λ. Such determination might be possible through the spectral index of the fluxes, rather than their absolute value. We give an estimate of the overall theoretical uncertainty for λ.

Part Four (Chapter 5): Dependence on the Cosmic Ray Model.

We discuss different models for primary cosmic rays and how they affect the final leptonic fluxes and related spectral indices. This dependence constitutes an additional source of uncertainty of our model and affects the measure of λ as well.

Chapter 2

Part One: NLO versus LO QCD Predictions

2.1 Introduction to Part One

The flux of atmospheric neutrinos and muons at very high energies, above 1 TeV, passes from being originated in the decays of pions and kaons to being predominantly generated in semileptonic decays of charmed particles (see for example [5]). This flux is of importance for large area detectors of high energy cosmic neutrinos. Future km^3 arrays would be able to observe muons and neutrinos with energies that may reach 10^{12} GeV. Atmospheric muons and neutrinos would be one of the most important backgrounds, limiting the sensitivity of any "neutrino telescope" to astrophysical signals. Besides, they might be used for detector calibration and perhaps, more interestingly, be exploited to do physics, e.g. study neutrino masses.

Present experimental attempts to detect atmospheric muons from charm are spoiled by systematic errors. Theoretical predictions depend strongly on the reliability of the model adopted for charm production and decay and differ by orders of

magnitude, due to the necessity of extrapolating present accelerator data on open charm production in fixed target experiments, at laboratory energies of about 200 GeV, to the larger energies needed for atmospheric neutrinos, from 10^3 to 10^8 GeV (at about 10^8 GeV the rates become too small for a km^3 detector). These energies, from 40 GeV to 14 TeV in the center of mass, are comparable to the energies of the future RHIC at Brookhaven, 200 GeV, and LHC at CERN, 7 TeV.

The theoretically preferred model, perturbative QCD (pQCD), was thought to be inadequate because it could not account for several aspects of some of the early data on open charm production (in conflict with each other, on the other hand [6]), and because of a sensitivity of the leading-order (LO) calculation, the only existing until recently, to the charm quark mass, to the low partonic momentum fraction, x, behavior of the parton distributions and to higher order corrections. So, even if some now-obsolete pQCD calculations have appeared [7, 8], the models for charm production traditionally favored in studies of atmospheric fluxes have been non-perturbative: for example, besides semi-empirical parametrizations of the cross section, the quark-gluon string model (QGSM, a.k.a. dual parton model), based on Regge asymptotics, and the recombination quark-parton model (RQPM), incorporating the assumption of an intrinsic charm component in the nucleon (see [9]).

Today, however, pQCD predictions and experimental data are known to be compatible [10, 11, 12, 13, 14]: charm production experiments form a consistent set of data, and the inclusion of next-to-leading order (NLO) terms has been a major improvement over the leading-order treatment. Quoting from Appel [10], "the success of these calculations has removed the impetus to look for unconventional sources of charm production beyond the basic QCD".

A study based on pQCD was therefore performed in Ref. [15] (called TIG from

now on). CLEO and HERA results were incorporated, but for simplicity the LO charm production cross section was adopted, multiplied by a constant K factor of 2 to bring it in line with the next-to-leading order values, and supplemented by parton shower evolution and hadronization according to the Lund model. The neutrino and muon fluxes from charm were found to be lower than the lowest previous prediction, namely a factor of 20 below the RQPM [16], of 5 below the QGSM [17, 18], and of 3 below the lowest curve in Ref. [8].

Here we use the same treatment of TIG, except for the very important difference of using the actual next-to-leading order pQCD calculations of Mangano, Nason and Ridolfi [19] (called MNR from now on), as contained in the program we obtained from them (see also [20]), to compute the charm production cross sections. These are the same calculations used currently to compare pQCD predictions with experimental data in accelerator experiments. The main goal of this part is to compare the fluxes obtained with the NLO and with the LO, i.e. we will compute the K factor for the neutrino and muon fluxes. This K factor is necessarily different from the K factor for charm production (which can be found in the literature), because only the forward going leptons contribute significantly to the atmospheric fluxes.

A similar comparison was very recently made in [21], using the approximate analytical solutions introduced by TIG to the cascade equations in the atmosphere. We make instead a full simulation of the cascades, using the combined MNR and PYTHIA programs. These two treatments of the problem are complementary. For comparison, we include results obtained with the CTEQ 3M gluon structure function used in Ref. [21]. We find our CTEQ 3M results to be close to those of the PRS study, in spite of the very different approaches used in the two calculations.

Addressing right away a concern that has been expressed to us several times, about the applicability of perturbative QCD calculations, mostly done for accel-

erator physics, to the different kinematic domain of cosmic rays, we would like to point out that, since the characteristic charm momentum in our simulations is of the order of the charm mass, $k \simeq O(m_c)$, we do not have here the uncertainty present in the differential cross sections [19], when k_T is much larger than m_c (as is the case in accelerators), due to the presence of large logarithms of $(k_T^2 + m_c^2)/m_c^2$. Depending on the steepness of the gluon structure function we take, we do have, however, large logarithms, known as "ln(1/x)" terms, where $x \simeq \sqrt{4m_c^2/s}$ (s is the hadronic center of mass energy squared) is the average value of the hadron energy fraction needed to produce the $c\bar{c}$ pair. These should not be important for steep enough gluon structure functions, but we have not made any attempt to deal with this issue.

In the next section of this chapter we explain our normalization of the NLO charm production cross section in the MNR program. In Sect. 2.3 we describe the computer simulations used to calculate the neutrino and muon fluxes. In Sect. 2.4 we show the results of our simulations, we discuss the differences between a NLO and a LO approach and we make a comparison with the fluxes of the TIG model.

In this work we consider only vertical showers for simplicity (the same was done by TIG).

2.2 Charm production in perturbative QCD

In this section, we show evidence that perturbative QCD gives a fair description of the present accelerator data on open charm production in the kinematic region most important for cosmic ray collisions in the atmosphere.

There are still not many experiments on open charm production with good enough statistics, despite the recent improvements, but many are expected in the

near future.

We use a NLO approach which is based on the MNR calculation, for which we have obtained the computer code. The NLO cross section for charm production depends on the choice of the parton distribution functions (PDF's) and on three parameters: the charm quark mass m_c, the renormalization scale μ_R, and the factorization scale μ_F.

2.2.1 Choice of m_c, μ_R, μ_F

MNR have two default choices of m_c, μ_R and μ_F: for total cross sections they choose $m_c = 1.5$ GeV, $\mu_R = m_c$, $\mu_F = 2m_c$; for differential cross sections they choose instead $m_c = 1.5$ GeV, $\mu_R = m_T$, $\mu_F = 2m_T$, where $m_T = \sqrt{k_T^2 + m_c^2}$ is the transverse mass.

The current procedure to reproduce the measured differential cross sections [12, 13, 14] is to use the MNR default choices for these three parameters and multiply the result by the global factor of about 2 or 3 necessary to match the predicted and measured total inclusive cross sections. Although this procedure might be acceptable in face of the uncertainties in the pQCD predictions, we find it unsatisfactory from a theoretical point of view. We prefer to fit the differential and total cross sections with one and the same combination of m_c, μ_R, and μ_F.

We make separate fits of m_c, μ_R, and μ_F for each of the following sets of PDF's: MRS R1, MRS R2 [22], CTEQ 3M [23] and CTEQ 4M [24] (see the next subsection for details).

We are aware that several choices of m_c, μ_R and μ_F may work equally well. In fact the cross sections increase by decreasing μ_F, μ_R or m_c, so changes in the three variables can be played against each other to obtain practically the same results.

We present here just one such choice.

We choose $\mu_R = m_T$, $\mu_F = 2m_T$ for all sets, and

$$m_c = 1.185 \text{ GeV} \quad \text{for MRS R1,} \tag{2.1}$$

$$m_c = 1.31 \text{ GeV} \quad \text{for MRS R2,} \tag{2.2}$$

$$m_c = 1.24 \text{ GeV} \quad \text{for CTEQ 3M,} \tag{2.3}$$

$$m_c = 1.27 \text{ GeV} \quad \text{for CTEQ 4M.} \tag{2.4}$$

We fit m_c, μ_R, and μ_F to the latest available data on charm production [11, 12, 13, 14] in proton-nucleon and pion-nucleon collisions. We use mainly the data on pN collisions, which are more relevant to us, but examine also the πN data to see how well our choice of parameters works there.

The MNR program calculates the total cross section for $c\bar{c}$ pair production, $\sigma_{c\bar{c}}$. We converted the experimental data on D^+ or D^- production $\sigma(D^+, D^-)$, D^0 or $\bar{D}^0$ production $\sigma(D^0, \bar{D}^0)$, or the same cross sections just for $x_F > 0$ (x_F is the Feynman x), $\sigma_+(D^+, D^-)$ and $\sigma_+(D^0, \bar{D}^0)$, into $\sigma_{c\bar{c}}$ values following [14].

The data we used for the 'calibration' of the MNR program are shown in Table 2.1 and Table 2.2 [11, 12, 13, 14]. These tables also present a comparison of experimental data on total inclusive D-production cross sections (converted to $\sigma_{c\bar{c}}$ total cross sections) with those calculated with the MNR program.

For the data of Table 2.1, for pN collisions, the conversion is done using

$$\sigma_{c\bar{c}} = 1.5 \times \frac{1}{2} \times [\sigma(D^+, D^-) + \sigma(D^0, \bar{D}^0)] \tag{2.5}$$

if cross sections are measured for any x_F, or

$$\sigma_{c\bar{c}} = 1.5 \times 2 \times \frac{1}{2} \left[\sigma_+(D^+, D^-) + \sigma_+(D^0, \bar{D}^0)\right] , \tag{2.6}$$

if experimental data are given for $x_F > 0$ only. The explanation of the factors in Eqs. (2.5),(2.6) is as follows. The $\frac{1}{2}$ factors convert single D inclusive into $D\bar{D}$ pair inclusive cross sections. The 1.5 factors are required to take into account the production of D_S and Λ_c (which is included in $\sigma_{c\bar{c}}$) through the ratios [14]

$$\frac{\sigma(D_S)}{\sigma(D^+, D^0)} \simeq 0.2, \qquad \frac{\sigma(\Lambda_c)}{\sigma(D^+, D^0)} \simeq 0.3, \tag{2.7}$$

(the same relation also for antiparticles). The factor 2 in Eq. (2.6) converts from $x_F > 0$ to all x_F (i.e. it is $\sigma_{c\bar{c}}/\sigma_{c\bar{c}}(x_F > 0)$ for the pN case).

In the case of πN collisions (Table 2.2) the factor 2 in equation (2.6) is replaced by 1.6, which is the value of $\sigma_{c\bar{c}}/\sigma_{c\bar{c}}(x_F > 0)$ when a pion beam is used.

Table 2.1 explains our choice of m_c values. The m_c values in Eqs.(2.1),(2.2),(2.3) and (2.4) reproduce well the central values of the pN charm inclusive total cross sections [11], using the program with the four different PDF's.

In Table 2.2 we also present a similar analysis for πN collisions, using only MRS R1 for simplicity. In this case slightly higher values of m_c fit the πN data [11, 14] a bit better, while $m_c = 1.185$ GeV, the value we take with the MRS R1 PDF, fits the pN data [11, 12, 14] a bit better. Notice that for the pions we used a different PDF, SMR2 [25], the same used in Refs. [11, 12] (obviously not used in our calculations of atmospheric fluxes). We present the πN data just for completeness, to show that they too are reasonably well fitted with our choice of parameters. These other values of m_c in Table 2.2 well reproduce the $\pi^{\pm}N$ data at 250 GeV [11] and the

$\pi^- N$ data at 350 GeV [13] (which seem a bit too low with respect to the data at 250 GeV). Even if each value of m_c reproduces best each total cross section, all three provide reasonable fits to all data, as can be seen also in the Figs. 2.1-2.3.

In Figs. 2.1-2.3 we present total and differential cross sections calculated with the MNR program and compared to the experimental data. As a way of example, we describe our fits for MRS R1 only.

Fig. 2.1a shows the fit to pN total cross sections (converted into $\sigma_{c\bar{c}}$ values as described above). In addition to the experimental value of Table 2.1 — which is the fundamental one, since it's the experiment whose differential cross sections we want also to fit — we added other experimental points coming from previous experiments (for details see [14]). For pN the $m_c = 1.185$ GeV is the best choice.

Fig. 2.1b shows the same for πN collisions. Here, as explained before, values of $m_c = 1.25$ GeV or $m_c = 1.31$ GeV are a better choice. Again we added here for completeness other experimental points coming from previous experiments [14].

Fig. 2.2ab shows fits to D-inclusive differential cross sections. In this figure the theoretically obtained $d\sigma_{c\bar{c}}/dx_F$ and $d\sigma_{c\bar{c}}/dp_T^2$ were converted into D-cross sections, with no extra factors. Fig. 2.2ab presents the data of the E769 collaboration [12] for pN and πN at 250 GeV. In these cases the differential $\sigma_{c\bar{c}}$ cross sections are converted into single inclusive ones (by a factor of 2) and then into cross sections for production of $D^{\pm}, D^0, \bar{D}^0$ and $D_S^{\pm}$ (by a factor of 1.2/1.5, see Eq. (2.7)) for the E769 data. For example,

$$\frac{d\sigma}{dx_F}(D^{\pm}, D^0, \bar{D}^0, D_S^{\pm}) \simeq \frac{1.2}{1.5} \times 2 \times \frac{d\sigma_{c\bar{c}}}{dx_F} \tag{2.8}$$

for Fig. 2.2a (and similar factors for $d\sigma/dp_T^2$ for Fig. 2.2b). The fit to the $d\sigma/dp_T^2$ pN data in Fig. 2.2b seems to be a bit too low, but it is not very different from the

fit shown in Fig. 2.2 of reference [12]. The predicted $d\sigma/dp_T^2$ are not sensitive to differences in m_c that are instead more noticeable in $d\sigma/dx_F$.

Fig. 2.3ab presents the πN data at 350 GeV of the WA92 collaboration [13] in a way similar to Fig. 2.2ab. In these cases the differential $\sigma_{c\bar{c}}$ cross sections are converted into a single inclusive ones (by a factor of 2) and then into cross sections for production of $D^{\pm}$, D^0 and $\bar{D}^0$ only (by a factor of 1.0/1.5, see Eq. (2.7)) for the WA92 data. Similar conclusions can be drawn: for pions $m_c = 1.31$ GeV is the best choice in this case.

We have performed the same analysis with MRS R2, CTEQ 4M and CTEQ 3M, even if we do not show here any of the fits. The results for total and differential cross sections were similar to those shown for the MRS R1, the only difference being the choice of m_c.

In conclusion, we obtain good fits to all data on charm production with one choice of μ_R, μ_F and m_c for each PDF, without other normalizations.

2.2.2 Choice of PDF's

Consider the collision of a cosmic ray nucleus of energy E per nucleon, with a nucleus of the atmosphere in which charm quarks of energy E_c are produced, which decay into leptons of energy E_l (in the lab. frame, namely the atmosphere rest frame). Due to the steep decrease with increasing energy of the incoming flux of cosmic rays, only the most energetic charm quarks produced count for the final lepton flux, and these c quarks come from the interactions of projectile partons carrying a large fraction of the incoming nucleon momentum. Thus, the characteristic x of the projectile parton, that we call x_1, is large. It is $x_1 \simeq O(10^{-1})$. We can, then, immediately understand that very small parton momentum fractions are needed in

our calculation, because typical partonic center of mass energies $\sqrt{\hat{s}}$ are close to the $c\bar{c}$ threshold, $2m_c \simeq 2$ GeV (since the differential cross section decreases with increasing $\hat{s}$), while the total center of mass energy squared is $s = 2m_N E$ (with m_N the nucleon mass, $m_N \simeq 1$ GeV). Calling x_2 the momentum fraction of the target parton (in the nuclei of the atmosphere), then, $x_1 x_2 \equiv \hat{s}/s = 4m_c^2/(2m_N E) \simeq$ GeV$/E$. Thus, $x_2 \simeq O(\text{GeV}/0.1\ E)$, where E is the energy per nucleon of the incoming cosmic ray in the lab. frame. The characteristic energy E_c of the charm quark and the dominant leptonic energy E_l in the fluxes are $E_l \simeq E_c \simeq 0.1E$, thus $x_2 \simeq O(\text{GeV}/\ E_l)$, as mentioned above.

For $x > 10^{-5}$ ($E \lesssim 10^3$ TeV), PDF's are available from global analyses of existing data. We use four sets of PDF's. MRS R1, MRS R2 [22] and CTEQ 4M [24], incorporate most of the latest HERA data and cover the range of parton momentum fractions $x \geq 10^{-5}$ and momentum transfers $Q^2 \geq 1.25 - 2.56$ GeV^2. MRS R1 and MRS R2 differ only in the value of the strong coupling constant α_s at the Z boson mass: in MRS R1 $\alpha_s(M_Z^2) = 0.113$, and in MRS R2 $\alpha_s(M_Z^2) = 0.120$. The former value is suggested by "deep inelastic scattering" experiments, and the latter by LEP measurements. This difference leads to different values of the PDF parameters at the reference momentum $Q_0^2 = 1.25$ GeV^2 where the QCD evolution of the MRS R1 and R2 PDF's is started. The CTEQ 4M is the standard choice in the $\overline{MS}$ scheme in the most recent group of PDF's from the CTEQ group ($\alpha_s(M_Z^2) = 0.116$ for CTEQ 4M). We also use an older PDF by the CTEQ group, namely the CTEQ 3M [23], only for comparisons with [21], where it is used as the main PDF.

For $x < 10^{-5}$ ($E \gtrsim 10^3$ TeV), we need to extrapolate the available PDF's. For $x \ll 1$, all these PDF's go as

$$x f_i(x, Q^2) \simeq A_i x^{-\lambda_i(Q^2)}, \tag{2.9}$$

where i denotes valence quarks u_v, d_v, sea quarks S, or gluons g . The PDF's we used (except the older CTEQ 3M) have $\lambda_S(Q_0^2) \neq \lambda_g(Q_0^2)$, in contrast to older sets of PDF's which assumed an equality. As x decreases the density of gluons grows rapidly. At $x \simeq 0.3$ it is comparable to the quark densities but, as x decreases it increasingly dominates over the quark densities, which become negligible at $x \lesssim 10^{-3}$.

We need, therefore, to extrapolate the gluon PDF's to $x < 10^{-5}$. Extrapolations based on Regge analysis usually propose $xg(x) \sim x^{-\lambda}$ with $\lambda \simeq 0.08$ [26], while evolution equations used to resum the large logarithms $\alpha_s \ln(1/x)$ mentioned above, such as the BFKL (Balitsky, Fadin, Kuraev, Lipatov [27]) find also $xg(x) \sim x^{-\lambda}$ but with $\lambda \simeq 0.5$ [26]. A detailed analysis of the dependence of the neutrino fluxes on the low x behavior of the PDF's will be given in the next chapter. As mentioned above, in the present part our goal is to compare NLO to BORN simulations, for which we use a simplified extrapolation at low x of the gluon PDF, which is somewhat in between the two extreme theoretical behaviors described above. For MRS R1-R2 and CTEQ 4M we take a linear extrapolation of $\ln g(x)$ as a function of $\ln x$, in which we took $\ln g(x) = -(\lambda_g(Q^2) + 1) \ln x + \ln A_g$, where $\lambda_g(Q^2)$ was taken as its value at $x = 10^{-5}$, the smallest x for which the PDF's are provided; for the CTEQ 3M we used a polynomial approximation which is included in the PDF package.

2.3 Simulation of particle cascades in the atmosphere

We simulate the charm production process in the atmosphere and the subsequent particle cascades, by modifying and combining together two different programs: the

MNR routines [19] and PYTHIA 6.115 [28].

The MNR program was modified to become an event generator for charm production at different heights in the atmosphere and for different energies of the incoming primary cosmic rays.

The charm quarks (and antiquarks) generated by this first stage of the program are then fed into a second part which handles quark showering, fragmentation and the interactions and decays of the particles down to the final leptons. The cascade evolution is therefore followed throughout the atmosphere: the muon and neutrino fluxes at sea level are the final output of the process.

In this section we give a brief description of the main parts of the simulation. Even if our program is completely different from the one used by TIG, because it is constructed around the MNR main routines, nevertheless we keep the same modeling of the atmosphere and of the primary cosmic ray flux as in TIG and the same treatment of particle interactions and decays in the cascade.

Our main improvement is the inclusion of a true NLO contribution for charm production (and updated PDF's), so we keep all other assumptions of the TIG model in order to make our results comparable to those of TIG. We study the effect of modifying some of their other assumptions in the next chapters.

2.3.1 The model for the atmosphere

We assume a simple isothermal model for the atmosphere. Its density at vertical height h is

$$\rho(h) = \frac{X_0}{h_0} e^{-h/h_0}, \tag{2.10}$$

where the scale height $h_0 = 6.4$ km and the column density $X_0 = 1300$ g/cm^2 at $h = 0$ are chosen as in TIG, to fit the actual density in the range 3 km $< h <$ 40 km,

important for cosmic ray interactions. Along the vertical direction, the amount of atmosphere traversed by a particle, the depth X, is related to the height h simply by

$$X = \int_h^\infty \rho(h')dh' = X_0 e^{-h/h_0}. \tag{2.11}$$

The atmospheric composition at the important heights is approximately constant: 78.4% nitrogen, 21.1% oxygen and 0.5% argon with average atomic number $\langle A \rangle = 14.5$.

2.3.2 The primary cosmic ray flux

Following TIG [15], we neglect the detailed cosmic ray composition and consider all primaries to be nucleons with energy spectrum

$$\phi_N(E,0)\left[\frac{nucleons}{cm^2\ s\ sr\ GeV\ /\ A}\right] = \left\{ \begin{array}{ll} 1.7\ (E/GeV)^{-2.7} & for\ E < 5\ 10^6\ GeV \\ 174\ (E/GeV)^{-3.0} & for\ E > 5\ 10^6\ GeV \end{array} \right\} \tag{2.12}$$

The primary flux is attenuated as it penetrates into the atmosphere by collisions against the air nuclei. An approximate expression for the intensity of the primary flux at a depth X is (see [15] again)

$$\phi_N(E,X) = e^{-X/\Lambda_N(E)}\ \phi_N(E,0)\ . \tag{2.13}$$

The nuclear attenuation length Λ_N, defined as

$$\Lambda_N(E) = \frac{\lambda_N(E)}{1 - Z_{NN}(E)}\ , \tag{2.14}$$

has a mild energy dependence through Z_{NN} and λ_N. Here Z_{NN} is the spectrum-weighted moment for nucleon regeneration in nucleon-nucleon collisions, for which we use the values in Fig. 4 of Ref. [15]. And λ_N is the interaction thickness

$$\lambda_N(E,h) = \frac{\rho(h)}{\sum_A \sigma_{NA}(E) n_A(h)} , \tag{2.15}$$

where $n_A(h)$ is the number density of air nuclei of atomic weight A at height h and $\sigma_{NA}(E)$ is the total inelastic cross section for collisions of a nucleon N with a nucleus A.[1] This cross section scales essentially as $A^{2/3}$, since for the large nucleon-nucleon cross sections we deal with, the projectiles do not penetrate the nucleus. So we set $\sigma_{NA}(E) = A^{2/3}\sigma_{NN}(E)$. For $\sigma_{NN}(E)$ we use the fit to the available data in Ref. [30]. Using our height independent atmospheric composition, we simplify Eq. (2.15) as follows,

$$\lambda_N(E,h) = \frac{\langle A \rangle}{\langle A^{2/3} \rangle} \frac{\mathrm{u}}{\sigma_{NN}(E)} = 2.44 \frac{\mathrm{u}}{\sigma_{NN}(E)} . \tag{2.16}$$

Here $\langle\ \rangle$ denotes average and u is the atomic mass unit, that we write as

$$\mathrm{u} = 1660.54 \text{ mb g/cm}^2. \tag{2.17}$$

We therefore find that in our approximations $\lambda_N(E)$ is independent of height.

---

[1] We recall that the elastic cross section contributes negligibly to the primary flux attenuation because the average elastic energy loss is very small, less than 1 GeV at the high energies we consider. This can be seen using the differential elastic cross section $d\sigma_{el}/dQ^2 = (d\sigma_{el}/dQ^2)_{Q^2=0} \exp(-bQ^2)$ with $b = [7.9 + 0.9 \ln p_{lab}]\mathrm{GeV}^{-2}$, with p_{lab} in GeV [29]. Here Q is the momentum transfer of the colliding proton of incoming momentum p_{lab} and mass M. The mean energy loss is the mean value of $Q^2/2M$ (here M is the target proton mass) namely $(1/2Mb) = 67\mathrm{MeV}/(1 + 0.1 \ln(p_{lab}/\mathrm{GeV}))$. This is 46 MeV at $E = 100\mathrm{GeV}$, and smaller at higher energies.

2.3.3 Charm production with MNR routines

As we remarked before, the modified MNR routines are the first stage of our simulation. For a given energy E of a primary incoming proton in the lab system, i.e. in the atmosphere reference frame, we generate a collision with a nuclear target at rest in the atmosphere, activating the MNR routines (primary event, pN collision, with $N = (p+n)/2$) .

These routines generate total and differential cross sections through a VEGAS integration, which creates a large number of 'subevents', each one with a particular weight, which in the original MNR program are summed together to calculate the final cross sections.

It is easy to modify the program so that each of these subevents (together with its weight) can represent the production of a charm c (or of a $c\bar{c}$ pair, or $c\bar{c}$ gluon, etc.) with given kinematics in any particular reference frame of interest. The original MNR routines can calculate single differential cross sections, in which the kinematics of only one final c quark is available, and double differential cross sections, in which the full kinematics of the $c\bar{c}$ pair (plus an additional parton in NLO processes) becomes available, for each subprocess. We have used both these possibilities. We will refer to them as 'single' and 'double' modes. The 'single' is the mode we use to obtain all our results. We use the 'double' mode only to compare the results of the independent fragmentation model used in the evolution of cascades in the 'single' mode, with the more reliable string fragmentation model, which can only be used in the 'double' mode, as we explain below.

The MNR program [19, 20] contains all BORN and NLO processes. In the 'single' mode we can generate the following processes, with only the kinematics of

the c quark available,

$$gg \to cX;\ \ q\bar{q} \to cX \text{ (BORN)} \quad gg \to cX;\ \ q\bar{q} \to cX;\ \ qg \to cX \text{ (NLO)} \qquad (2.18)$$

where q represents any light quark or antiquark. In the 'double' mode we have the following processes

$$gg \to c\bar{c};\ \ q\bar{q} \to c\bar{c} \text{ (BORN)} \quad gg \to c\bar{c}g;\ \ q\bar{q} \to c\bar{c}g;\ \ qg \to c\bar{c}q \text{ (NLO)} \qquad (2.19)$$

for which the kinematics of all the outgoing partons is fully determined for each 'subevent'.

All the kinematical variables of the partons in the final state constitute the input for the next stage of the program, described in the next subsection.

An important characteristic of the first stage is that, besides m_c, μ_R, and μ_F, we can select any desired PDF to be used with the charm production routines. We have updated the set of PDF's in the original MNR program.

According to the discussion of Sect. 2.2, we use the MRS R1, MRS R2, CTEQ 3M and CTEQ 4M parton distribution functions, together with the values of m_c, μ_R, and μ_F in Eqs. (2.1–2.4).

As a concrete example of the integrals performed in our program, here we write the differential flux ϕ_μ of muons (namely of $\mu^+ + \mu^-$) with energy E_μ (μ stands here for μ^+ or μ^-) in the 'single' mode (ϕ_μ has units cm^{-2} s^{-1} sr^{-1} GeV $^{-1}$)

$$\begin{aligned}\phi_\mu(E_\mu) &= \int_{E_\mu}^{\infty} dE \int_0^{\infty} dh\ \phi_N(E, X(h)) \sum_A n_A(h) \times \\ &\int_{E_\mu}^{E} dE_c \left[\frac{d\sigma(pA \to cY; E, E_c)}{dE_c}\right]_{MNR} \left[\frac{dN_\mu(c \to \mu; E_c, E_\mu, h)}{dE_\mu}\right]_{PYTHIA} \\ &+ \ (c \to \bar{c}). \end{aligned} \qquad (2.20)$$

Here $n_A(h)$ is the number density of nuclei of atomic number A in the atmosphere, E is the energy of the primary cosmic ray proton, E_c the energy of the charm produced in the collision $pA \rightarrow cY$ (Y here stands for anything else). Using the relation $d\sigma(pA \rightarrow cY)/dE_c = A\, d\sigma(pN \rightarrow cY)/dE_c$, the sum over A becomes $\sum_A n_A(h)A = \rho(h)/u$. Using $dX = -\rho(h)dh$, Eq. (2.13), and normalizing to one the distribution in depth X, ϕ_μ becomes

$$\phi_\mu(E_\mu) = \int_{E_\mu}^{\infty} dE \int_{X_0}^{\infty} dX\ \phi_N(E, X=0)\ \frac{e^{-X/\Lambda_N(E)}}{\Lambda_N(E)}\ \left[\frac{f(h)\Lambda_N(E)}{u}\right], \qquad (2.21)$$

where, from Eqs.(2.14) and (2.16), $\Lambda_N/u = 2.44[\sigma_{NN}(1 - Z_{NN})]^{-1}$ and

$$f(h) = 2\int_{E_\mu}^{E} dE_c \left[\frac{d\sigma(pN \rightarrow cY; E, E_c)}{dE_c}\right]_{MNR} \left[\frac{dN_\mu(c \rightarrow \mu; E_c, E_\mu, h)}{dE_\mu}\right]_{PYTHIA}. \qquad (2.22)$$

Here the factor of 2 accounts for the muons produced by $\bar{c}$ (only c quarks are used in the program for simplicity); the pN inclusive charm production cross section is computed with the MNR program (here are the integrations over the PDF's and partonic cross sections) and the last square bracket is the number of muons of energy E_μ which reach sea level, produced in the cascades simulated by PYTHIA. Each cascade is initiated by a c quark (in the 'single' case) of energy E_c and momentum k (provided by the MNR routines) at a height h chosen through a random number R homogeneously distributed between 0 and 1, which gives the value of the X probability distribution in Eq. (2.21), namely $R = e^{-X/\Lambda_N(E)}$. The cancellation of soft and collinear singularities is performed in the MNR program under the integral sign. This process requires the generation of six correlated events for each randomly generated final-state configuration. In our program we make sure that also the height of the event, the only additional parameter of each event, is chosen

to have one common value for all correlated events.

2.3.4 Cascade evolution with PYTHIA routines

The parton c (or partons in the 'double' case) generated by the first stage, namely by the MNR routines, are entered in the event list of PYTHIA and they become the starting point of the cascade generation.

PYTHIA first fragments the c quark (in the 'single' mode, or all the partons in the 'double' mode) into hadrons, after showering, which can be optionally shut off. The charm quarks hadronize into D^0, $\bar{D}^0$, $D^{\pm}$, $D_s^{\pm}$ and Λ_c. We used here the Peterson fragmentation function option. For each hadron produced, a simple routine added to PYTHIA decides if the hadron interacts in the atmosphere (loosing some energy) or decays. This is the same approach as in TIG. PYTHIA follows in this way the cascade in the atmosphere and populates the histograms of muons and neutrinos as a function of their different energies. We mention here a few important technical details. The 'single' and 'double' modes described before use different fragmentation models. In the 'single' mode only one c quark is available and is entered at the beginning of the event list (with its energy and momentum in the partonic CM reference frame). In this case PYTHIA uses the 'independent fragmentation' model (see [28] for details). We only include c quarks and at the end multiply the result by a factor of two to account for initial $\bar{c}$ quarks.

In the 'double' mode, instead, which we only use at the LO, we start with two ($c\bar{c}$) partons in the event list. In this case we opt to use the 'string fragmentation' model (Lund model, [28]). This model generally gives better results than the independent fragmentation, in which energy and momentum conservation have to be imposed a posteriori and whose results depend on the reference frame used, which empirically is

chosen to be the partonic CM frame. To impose energy and momentum conservation in the independent fragmentation, we used the option (MSTJ(3)=1, see again [28]) in which particles share momentum imbalance compensation according to their energy (roughly equivalent to boosting events to CM frame) but we have convinced ourselves that the results do not depend much on the way of imposing energy and/or momentum conservation, because trial runs with different options have given similar results for the fluxes.

Even if independent fragmentation is in general less desirable than string fragmentation, we use the 'single' mode as our main choice. The main reason to use the 'single' mode is that the simulations run in acceptably short times (4-5 days) on a few SUN workstations that we use, while giving results practically identical to the 'double' mode in the comparisons we have made (see Fig. 2.6c). The simulation of the cascades in the 'double' mode takes between five and ten times longer. We tested the goodness of the independent fragmentation by comparing the outcome of fluxes computed at the Born level, in which the charm fluxes at production are identical (we put one c in the atmosphere and multiply the outcome by two to account for the $\bar{c}$ in one case, and we put $c\bar{c}$ in the atmosphere, instead, in the second case) and the sole difference in both modes is due to the different fragmentation models used. The results were extremely close (at Born level the difference is less than 5%, at energies above $10^5 GeV$), as can be seen in Fig. 2.6c.

Apart from the mentioned differences between the 'single' and 'double' modes, the simulations then proceed basically in the same way in both modes. For each of the 'subevents', i.e. for each set of initial parton(s) put in the event list, a certain height in the atmosphere is randomly chosen as explained above, this being the position at which the partons are generated from the initial proton-nucleon collision. This random height h is generated in a way similar to TIG (see Ref.

[15]), but different, because we include a correction for nucleon regeneration in nucleon-nucleon collisions by using Λ_N, the nuclear attenuation length, in Eq. (2.13) instead of λ_N , the interaction thickness (see Eqs. (2.14),(2.15) and (2.16)).The only difference compared to TIG (see Eq. (15) in the last paper of Ref. [15]) is the inclusion of the $(1 - Z_{NN})$ correction term. This was done because we could not include regenerated protons directly in our simulation of the cascades, since events and subevents are now created by the MNR routines and not by PYTHIA, as it was in TIG.

When parton showering is included at the beginning of the cascade simulation performed by PYTHIA, some double counting is present. The double counting appears when a LO diagram, for example $gg \rightarrow c\bar{c}$, with a subsequent splitting contained in PYTHIA, for example $c \rightarrow gc$ is summed to NLO diagram, $gg \rightarrow gc\bar{c}$ with the same topology, as if both diagram were independent, when actually the NLO contains the first contribution when the intermediate c quark on mass shell. We have not tried to correct this double counting but have instead confronted the results obtained including showering (our standard option) with those excluding showering (in which case there is no double counting) and found very similar leptonic fluxes (see Fig. 2.6b).

The particles generated after the initial hadronization are then followed throughout the atmosphere and PYTHIA evolves the cascade with the same treatment of interactions and decays proposed by TIG. The final number of muons and neutrinos at sea level is therefore calculated considering all the 'subevents', each with its respective weight W_i from the MNR program, which produce the final particles through all the possible decay channels of charmed particles decaying into prompt leptons. Since only the decay modes of charmed hadrons going into μ or ν_μ or ν_e are left open in the simulation, and there are essentially just 2 modes for each charmed

particle (for example: $D^+ \rightarrow e^+ \nu_e + anything$, with branching ratio = 0.172; $D^+ \rightarrow \mu^+ \nu_\mu + anything$, with branching ratio = 0.172; all other channels closed), the branching ratios for each of these modes is fictitiously taken by PYTHIA to be 1/2 and need to be normalized by multiplying by the actual branching ratio (0.172 for the example above) and dividing by 1/2. Besides, since not all events are accepted by PYTHIA to generate a complete cascade, the result is normalized by dividing by the sum of all the weights of accepted events and multiplying it by the total c inclusive cross section.

2.3.5 Summary

To summarize, our computation of the final fluxes is organized as follows.

• An external loop over the primary energy E generates an integration over E in the range $10^1 - 10^{11} GeV$.

• For each primary energy E, the MNR routines generate 'subevents' with weight W_i, for all the LO and NLO processes.

• Each subevent is assigned a random height (so that implicitly an integration over h is performed) and all this is passed to PYTHIA as a definite set of parton(s) to be put at the beginning of the event list.

• For each of these 'subevents', PYTHIA treats showering (in our standard option), hadronization and evolution of the cascade in the atmosphere, and generates the final leptons.

• For each decay channel of interest, the produced leptons are weighted with W_i and then summed into the final fluxes.

2.4 Neutrino and muon fluxes

Figs. 2.4-2.6 show the results of our simulations. Fig. 2.4 shows the total inclusive charm-anticharm production cross sections $\sigma_{c\bar{c}}$, and the K factor for c production, namely the ratio between the NLO and Born cross sections, $K_c = \sigma_{c\bar{c}}^{NLO}/\sigma_{c\bar{c}}^{Born}$, for the four PDF's we consider and for TIG. Fig. 2.5 shows our main results obtained with our default choice of options: a 'single' mode calculation including the contributions from all processes in Eq. (2.18) and with parton showering included in the cascade simulation performed by PYTHIA). Finally Fig. 2.6 shows the relative importance of the processes included in the fluxes and a comparison of the 'single' and 'double' modes and of the 'on' and 'off' showering options.

In Fig. 2.4a, the total inclusive charm-anticharm production cross sections $\sigma_{c\bar{c}}$ are plotted over the energy range needed by our program, $E \leq 10^{11}$ GeV, for our four different PDF's. They were calculated using the MNR program, with the 'calibration' described in Sect. 2.2, up to the NLO contribution. For comparison, we also show the cross section used by TIG and the Born (LO) contribution for one of the PDF's, MRS R1. We see in the figure that all our cross sections agree at low energies, as expected due to our 'calibration' at 250 GeV, and are very similar for energies up to $10^6 - 10^7$ GeV. At higher energies they diverge, differing by at most 50% at the highest energy we use, 10^{11} GeV. In fact, at energies beyond 10^7 GeV, the CTEQ 3M cross section becomes progressively larger than the CTEQ 4M and MRS R2 cross sections, which are very close to each other. The MRS R1 becomes on the contrary progressively lower than the other three.

We see in Fig. 2.4a that for energies above 10^4 GeV our cross sections are considerably higher than the one used by TIG. This difference can be traced in part to the use by TIG of an option of PYTHIA by which the gluon PDF is extrapolated

to $x \leq 10^{-4}$ with $\lambda = 0.08$, while all the PDF's we use have a higher value of $\lambda \simeq 0.2 - 0.3$. And in part to TIG scaling the LO cross sections obtained with PYTHIA by a constant K factor of 2, while at large energies the K factor is actually larger than 2 by about 10-15% (see Fig. 2.4b).

In Fig. 2.4b we explicitly show the K factor for c production, namely the ratio between the NLO and Born cross sections, $K_c = \sigma_{c\bar{c}}^{NLO}/\sigma_{c\bar{c}}^{Born}$, for our PDF's and for TIG. All the K_c values are around the usually cited value of 2 for most of the intermediate energies, but are larger at the lowest energies and also at the highest energies (except for CTEQ 3M), and they all are within about 15% of each other.

Fig. 2.5 contains three sets of figures, one for each lepton: μ, ν_μ and ν_e. The left figure of each set shows the E^3-weighted vertical prompt fluxes, for all our PDF's up to NLO (labelled 'NLO') and, as an example, the LO (labelled 'BORN') for MRS R1, together with the total fluxes up to NLO of TIG, both from prompt and conventional sources (dotted lines). The right part of each set shows the corresponding K_l value (where $l = \mu, \nu_\mu, \nu_e$), i.e. the ratio of the total NLO flux to the Born flux of the figure on the left. The figures show that our fluxes are higher than those of TIG for $E > 10^3$ GeV. Leaving apart differences in the two simulations that cannot be easily quantified, this discrepancy can largely be explained by the different cross sections used by TIG and us: the TIG cross section is lower than ours for $E > 10^4$ GeV. Using a value of λ similar to TIG ($\lambda \simeq 0$) at small x, we obtain fluxes similar to those of TIG at energies above 10^6 GeV (see next chapter).

In particular, our fluxes are all larger than TIG by factors of 3 to 10 at the highest energies, what puts our fluxes in the bulk-part of previous estimates (see Refs. [16, 17, 18, 8]). There is an evident dependence of the fluxes on the choice of PDF. It is remarkable that MRS R2 and CTEQ 4M give very similar results. Those of the MRS R1 become lower and those of the older CTEQ 3M PDF become higher

as the energy increases (both differing by about 30-50% at the highest energies with respect to the MRS R2-CTEQ 4M fluxes). This is due to the intrinsic differences of the PDF packages used and the consequent different extrapolated values of λ at small x or high energies.

The CTEQ 3M fluxes were included to compare our results with those of Ref. [21]. We find our CTEQ 3M results to be close to those of Ref. [21], in spite of the very different approaches used in the two calculations. Our fluxes lie between the two curves for CTEQ 3M shown in Fig.8 of Ref. [21], corresponding to different choices of renormalization and factorization scales. Our fluxes are lower (by 30-40% at 10^7GeV), than the main CTEQ 3M choice of Ref. [21] (solid line of their Fig.8), which is calculated using values of μ_R, μ_F and m_c similar to ours. Our cross section for charm production, for the CTEQ 3M case, is essentially equal to the one used in Ref. [21] (shown in their Fig. 2), so the discrepancies in the final fluxes are to be explained in terms of the differences in the cascade treatment. It is very difficult to trace the reasons for these differences.

We also see in the figures that, for each PDF, the fluxes for the different leptons are very similar: those for ν_μ neutrinos and ν_e are essentially the same, those for muons are only slightly lower (about 10% less at the energies of interest). Also the K_l's don't differ much for the three leptons, apart from some unphysical fluctuations especially evident at the highest energies. Even if they vary slightly, for different PDF's, they all show a similar energy dependence, namely they increase at low energies and sometimes at high energies also. This behavior is also similar to that of the K_c factors in Fig. 2.4b, but with a weaker overall energy dependence, as expected, since the leptons of a given energy result from c quarks with a range of higher energies.

The K_l factors are all within the range $2.1 - 2.5$: they are approximately 2.2 for

MRS R1, 2.4 for MRS R2 and CTEQ 4M, and 2.3 for CTEQ 3M. Thus, our analysis shows that evaluating the lepton fluxes only at the Born level, and multiplying them by an overall K_l factor of about $2.2 - 2.4$ (i.e. 10 to 20% larger than the value of 2 used by TIG[2]), can be good enough to evaluate the NLO fluxes within about 10%. Thus we find the approach used by TIG, who multiplied the LO fluxes obtained with PYTHIA by two, essentially correct, except for their relatively low K factor and the discrepancies existing even at Born level between our fluxes and those of TIG. In fact, as we mentioned previously, the differences between our final results and those of TIG depend mostly on the different total inclusive c cross sections, which can be traced to the extrapolation of the gluon PDF at small x rather than to the K factor. Possible causes of the different results due to the intrinsic differences of the computer simulations cannot be easily quantified.

In Fig. 2.6 we address three issues. First, we show that the fluxes can be obtained within about 30% with just the gluon-gluon process. This would speed up the simulations and, when using the MNR program, would give (contrary to intuition) higher fluxes than those actually derived from all processes. Secondly, we show that the fluxes obtained including or excluding showering in the simulation made by PYTHIA (we included showering in our standard options) do not differ significantly. The third issue we deal with is the difference between the 'single' and 'double' modes described before. We show that at LO the results from a 'double' mode calculation coincide with those of the much shorter 'single' mode, that we use in all our calculations. Let us deal with these three issues in turn.

In Fig. 2.6a we show, for a given PDF, the MRS R1, the relative importance of

[2]We note that in the original TIG model there is no distinction between K_c and K_l factors since only the Born level is considered. Their $K = 2$ factor is just a multiplicative constant which can be considered either a K_c or a K_l.

the different processes contributing to the final fluxes. The solid line is the total flux obtained as the sum of all the processes of Eq. (2.18) and the dotted line shows the result of only gluon-gluon fusion (gg), the sum of Born (gg) and pure NLO (excluding Born) gg processes. Also shown are the separate contributions only at the Born and at the NLO (excluding LO) of both gg and quark-antiquark ($q\bar{q}$) fusion, which clearly shows that gg dominates. This is to be expected because the gluon PDF is either much larger than (for $x < 0.1$) or comparable to (for $x \simeq \mathcal{O}(0.1)$) the quark PDF's. The figure plots the absolute value of the quark-gluon (qg) terms because, for the values of the factorization scale that we employ in our calculations, these terms are negative. This is due to the way the original MNR calculation is subdivided into processes. In fact, in the MNR program, a part of the quark-gluon contribution to the cross sections is already contained in other processes, and must be subtracted in the processes labelled as qg. The amount subtracted depends on the factorization scale μ_F and may drive the qg contribution negative. Roughly speaking, if μ_F is small the qg term is positive, otherwise (as in our case) the term is negative. The absolute value of the qg term is in between the $q\bar{q}$ and the gg terms, what makes negative the sum of all the processes different from gg. Thus, gluon-gluon processes alone give a result slightly larger than the total, by about 30%.

In Fig. 2.6b we check the effect of shutting off the showering option available in PYTHIA. We study only one specific case, the MRS R1. The overall effect is minimal: the exclusion of showering slightly increases the energy of the parent charmed hadrons and therefore causes the final fluxes of lepton daughters to move towards higher energies; the effect is barely noticeable and just slightly more important for the Born fluxes (the overall difference is about 5%). When showering is included some double counting occurs, whose effect must be smaller than the difference be-

tween the results with showering on and off (since in this case no double counting occurs).

Finally in Fig. 2.6c we confront the 'single' and 'double' modes of the program, for just one PDF, MRS R1, at Born level. At this level, the calculation of the charm flux at production is identical (we obtain the fluxes from c and multiply by two at the end to account for the $\bar{c}$ in one case, and we obtain the fluxes directly from $c\bar{c}$ in the other). So, what is actually compared in the two modes at the Born level is the fragmentation model: independent fragmentation in the 'single' mode and string (Lund) fragmentation in the 'double' mode. The results from both modes at the Born level are almost identical: as already remarked the difference is less than 5% for energies above 10^6 GeV.

2.5 Conclusions for Part One

We have used the actual next-to-leading order perturbative QCD calculations of charm production cross sections, together with a full simulation of the atmospheric cascades, to obtain the vertical prompt fluxes of neutrinos and muons.

Our treatment is similar to the one used by TIG, except for the very important difference of including the true NLO contribution, while TIG used the LO charm production cross section multiplied by a constant K factor of 2 to bring it in line with the next-to-leading order values. The main goal of this part is to examine the validity of TIG's procedure by computing the ratio of the fluxes obtained with the NLO charm production cross section versus those obtained with the LO cross section.

These ratios, the K_l factors are between 2.1 and 2.5 for the different gluon PDF's in the energy range from 10^2 to 10^9 GeV (see Fig. 2.5). Consequently, our analysis

shows that evaluating the lepton fluxes only at the Born level, and multiplying them by an overall factor of about $2.2 - 2.4$, slightly dependent on the PDF, can be good enough to evaluate the NLO fluxes within about 10%. Therefore, we find the approach used by TIG (i.e. multiplying the LO fluxes by two) essentially correct, except for their relatively low K factor. We find different lepton fluxes than TIG, but this is mostly due to the discrepancies, even at Born level, between our charm production cross sections and TIG's.

In fact, the prompt neutrino and muon fluxes found by TIG were lower than the lowest previous prediction. We find here instead fluxes in the bulk part of those previous predictions. This difference can be traced largely to the use by TIG of an option of PYTHIA by which the gluon PDF is extrapolated for $x \leq 10^{-4}$ with $\lambda = 0.08$, while all the PDF's in this paper have a higher value of $\lambda \simeq 0.2 - 0.3$. Using a value of λ similar to TIG ($\lambda \simeq 0$) we obtain fluxes similar to those of TIG, at energies above 10^6 GeV (see next chapter).

	Beam Energy (GeV)	$\sigma_+(x_F > 0)$ (μb)	$\sigma_{c\bar{c}}$(EXP.) (μb)	$\sigma_{c\bar{c}}$(MNR) (μb)	PDF
pN E769 [11]	250	$\sigma_+(D^+, D^-) = 3.3 \pm 0.4 \pm 0.3$ $\sigma_+(D^0, \bar{D}^0) = 5.7 \pm 1.3 \pm 0.5$	13.5 ± 2.2	13.54 $m_c = 1.185$ GeV	MRS R1
pN E769 [11]	250	$\sigma_+(D^+, D^-) = 3.3 \pm 0.4 \pm 0.3$ $\sigma_+(D^0, \bar{D}^0) = 5.7 \pm 1.3 \pm 0.5$	13.5 ± 2.2	13.43 $m_c = 1.31$ GeV	MRS R2
pN E769 [11]	250	$\sigma_+(D^+, D^-) = 3.3 \pm 0.4 \pm 0.3$ $\sigma_+(D^0, \bar{D}^0) = 5.7 \pm 1.3 \pm 0.5$	13.5 ± 2.2	13.59 $m_c = 1.27$ GeV	CTEQ4M
pN E769 [11]	250	$\sigma_+(D^+, D^-) = 3.3 \pm 0.4 \pm 0.3$ $\sigma_+(D^0, \bar{D}^0) = 5.7 \pm 1.3 \pm 0.5$	13.5 ± 2.2	13.45 $m_c = 1.24$ GeV	CTEQ3M

Table 2.1: Data on total cross sections for charm production for pN collisions, from E769 experiment, have been converted to $c\bar{c}$ cross sections and compared to the predictions of the MNR program running at slightly different values of the charm mass m_c, using different PDF's.

	Beam Energy (GeV)	$\sigma_+(x_F > 0)$ (μb)	$\sigma_{c\bar{c}}$(EXP.) (μb)	$\sigma_{c\bar{c}}$(MNR) (μb) $m_c =$ 1.185 GeV	$\sigma_{c\bar{c}}$(MNR) (μb) $m_c =$ 1.250 GeV
$\pi^- N$ E769 [11]	210	$\sigma_+(D^+, D^-) =$ $1.7 \pm 0.3 \pm 0.1$ $\sigma_+(D^0, \bar{D}^0) =$ $6.4 \pm 0.9 \pm 0.3$	9.7 ± 1.2	14.08	10.64
$\pi^- N$ E769 [11]	250	$\sigma_+(D^+, D^-) =$ $3.6 \pm 0.2 \pm 0.2$ $\sigma_+(D^0, \bar{D}^0) =$ $8.2 \pm 0.7 \pm 0.5$	14.2 ± 1.1	16.54	12.56
$\pi^+ N$ E769 [11]	250	$\sigma_+(D^+, D^-) =$ $2.6 \pm 0.3 \pm 0.2$ $\sigma_+(D^0, \bar{D}^0) =$ $5.7 \pm 0.8 \pm 0.4$	10.0 ± 1.2	16.54	12.56
$\pi^\pm N$ E769 [11]	250	$\sigma_+(D^+, D^-) =$ $3.2 \pm 0.2 \pm 0.2$ $\sigma_+(D^0, \bar{D}^0) =$ $7.2 \pm 0.5 \pm 0.4$	12.5 ± 0.8	16.54	12.56
$\pi^- N$ WA92 [13]	350	$\sigma_+(D^+, D^-) =$ $3.28 \pm 0.08 \pm 0.29$ $\sigma_+(D^0, \bar{D}^0) =$ $7.78 \pm 0.14 \pm 0.52$	13.3 ± 0.7	22.22	17.06 (13.5 for $m_c = 1.31$ GeV)

Table 2.2: Data on total cross sections for charm production for πN collisions, from E769 and WA92 experiments, have been converted to $c\bar{c}$ cross sections and compared to the predictions of the MNR program running at slightly different values of the charm mass m_c, using MRS R1.

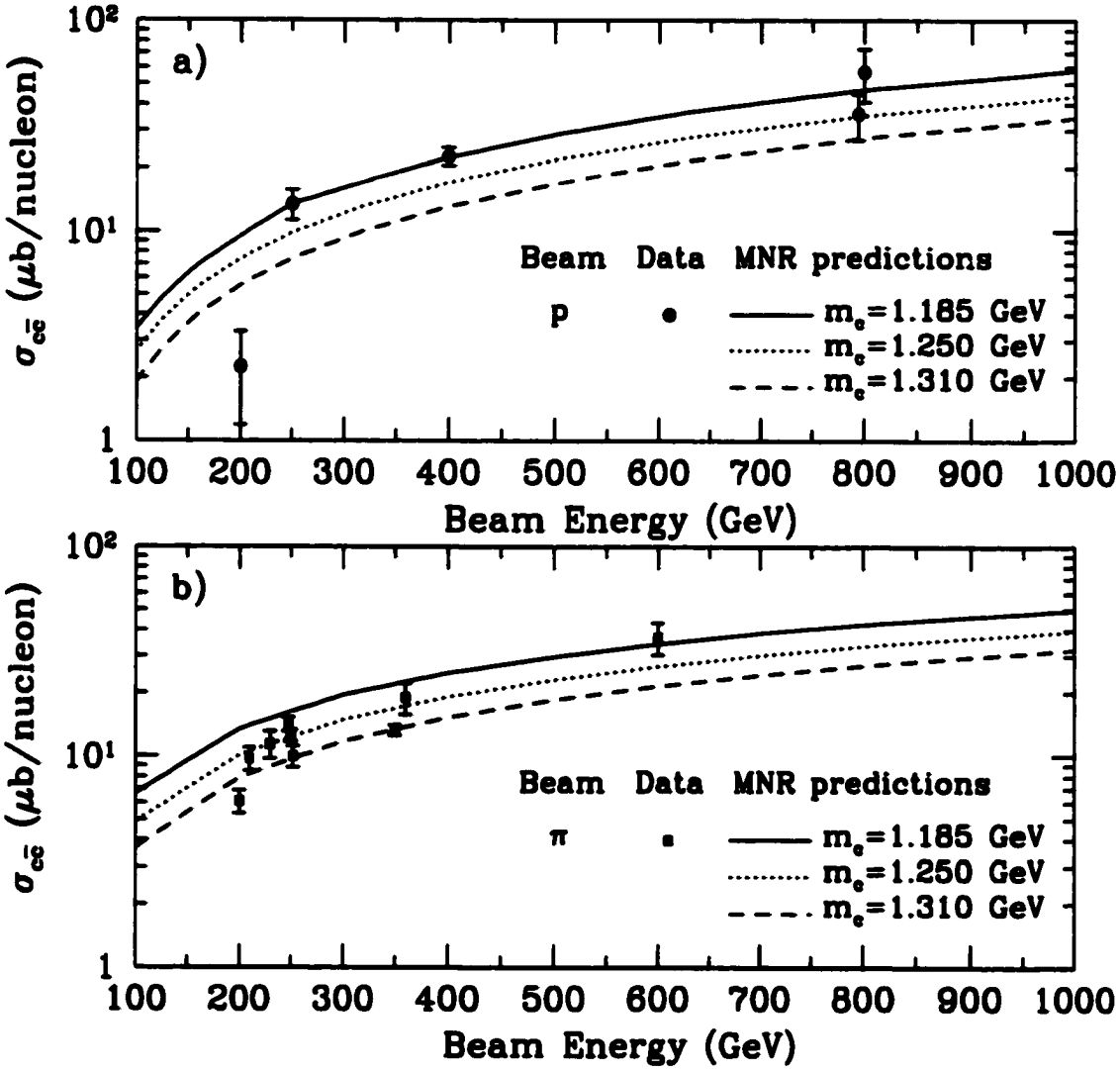

Figure 2.1: Comparison of experimental data for $\sigma_{c\bar{c}}$ with MNR predictions for different m_c values: (a) in pN collisions ([14], Table 2.1), (b) in πN collisions ([14], Table 2.2) (PDF: MRS R1).

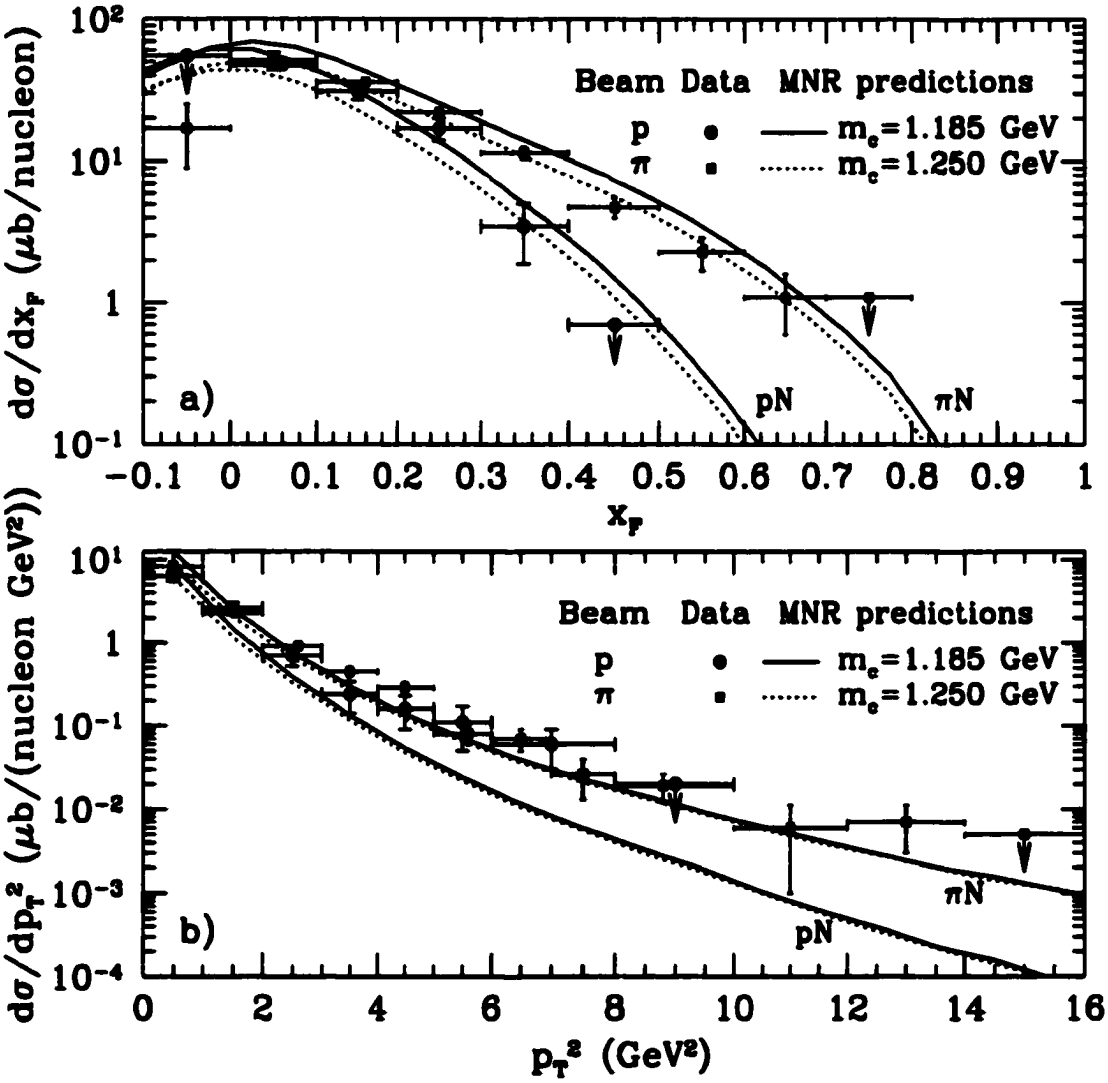

Figure 2.2: Comparison of differential cross sections for ($D^+, D^-, D^0, \bar{D}^0, D_S^+$ and D_S^-) production, calculated using MNR at different m_c values, with E769 data for pN and πN [12]: (a) $d\sigma/dx_F$, (b) $d\sigma/dp_T^2$ ($x_F > 0$) (PDF:MRS R1).

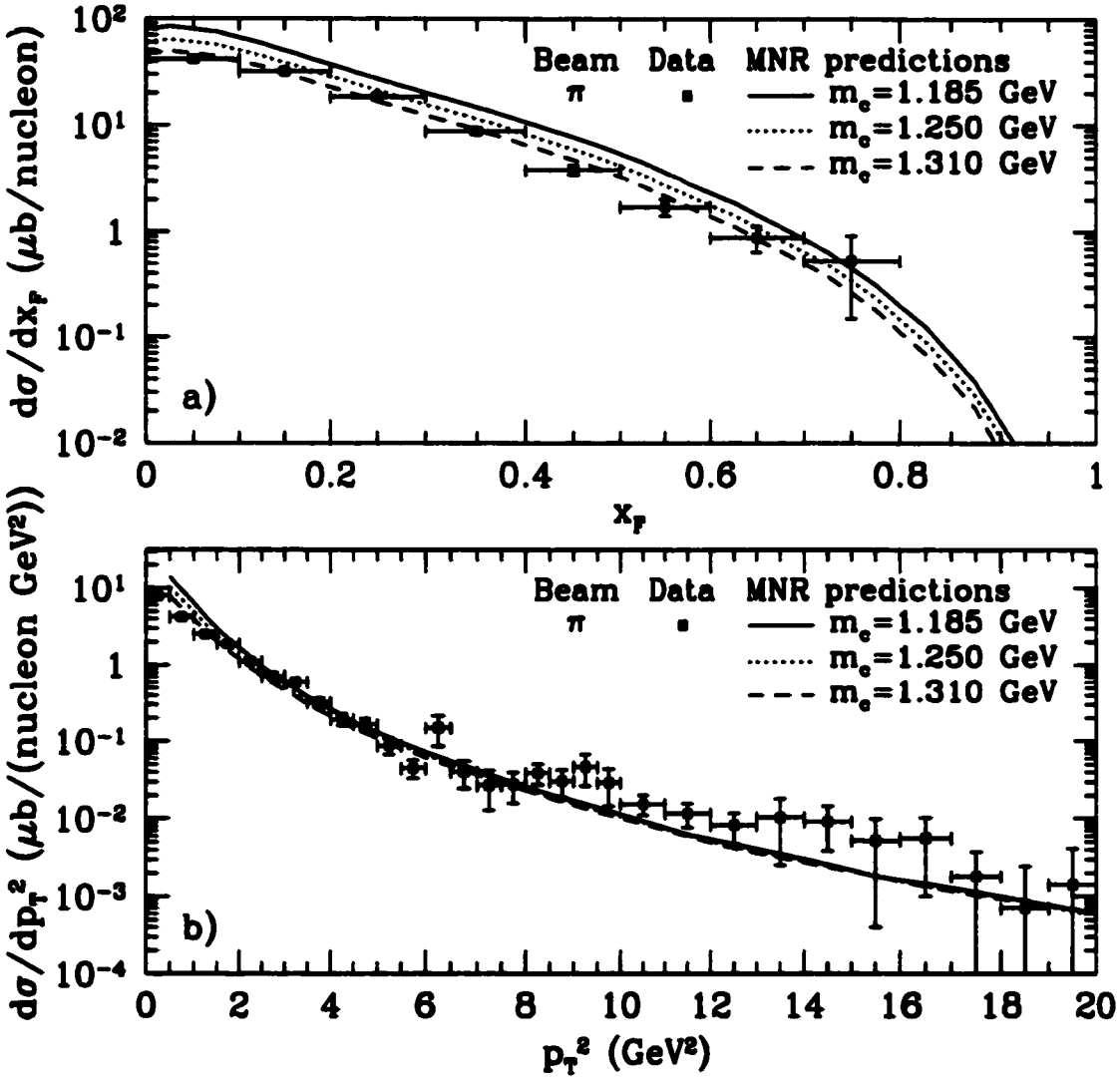

Figure 2.3: Comparison of differential cross sections for $(D^+, D^-, D^0, \bar{D}^0)$ production, calculated using MNR at different m_c values, with WA92 data for πN [13]: (a) $d\sigma/dx_F$, (b) $d\sigma/dp_T^2$ $(x_F > 0)$ (PDF: MRS R1).

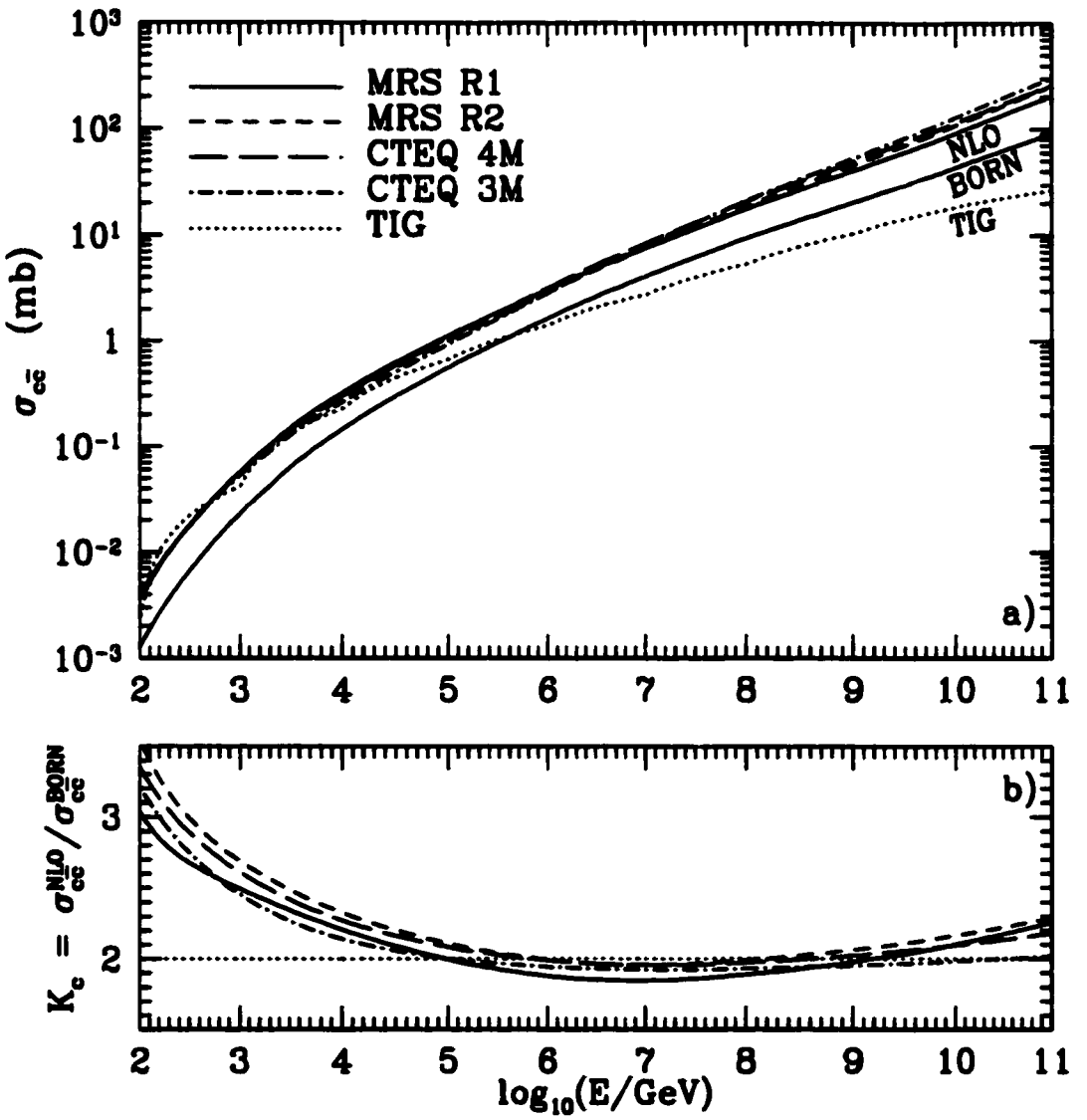

Figure 2.4: (a) Total cross sections for charm production $\sigma_{c\bar{c}}$ up to NLO, for different PDF's, compared to the one used in the TIG model [15] (for MRS R1 we also show the Born cross section). (b) Related K_c factors.

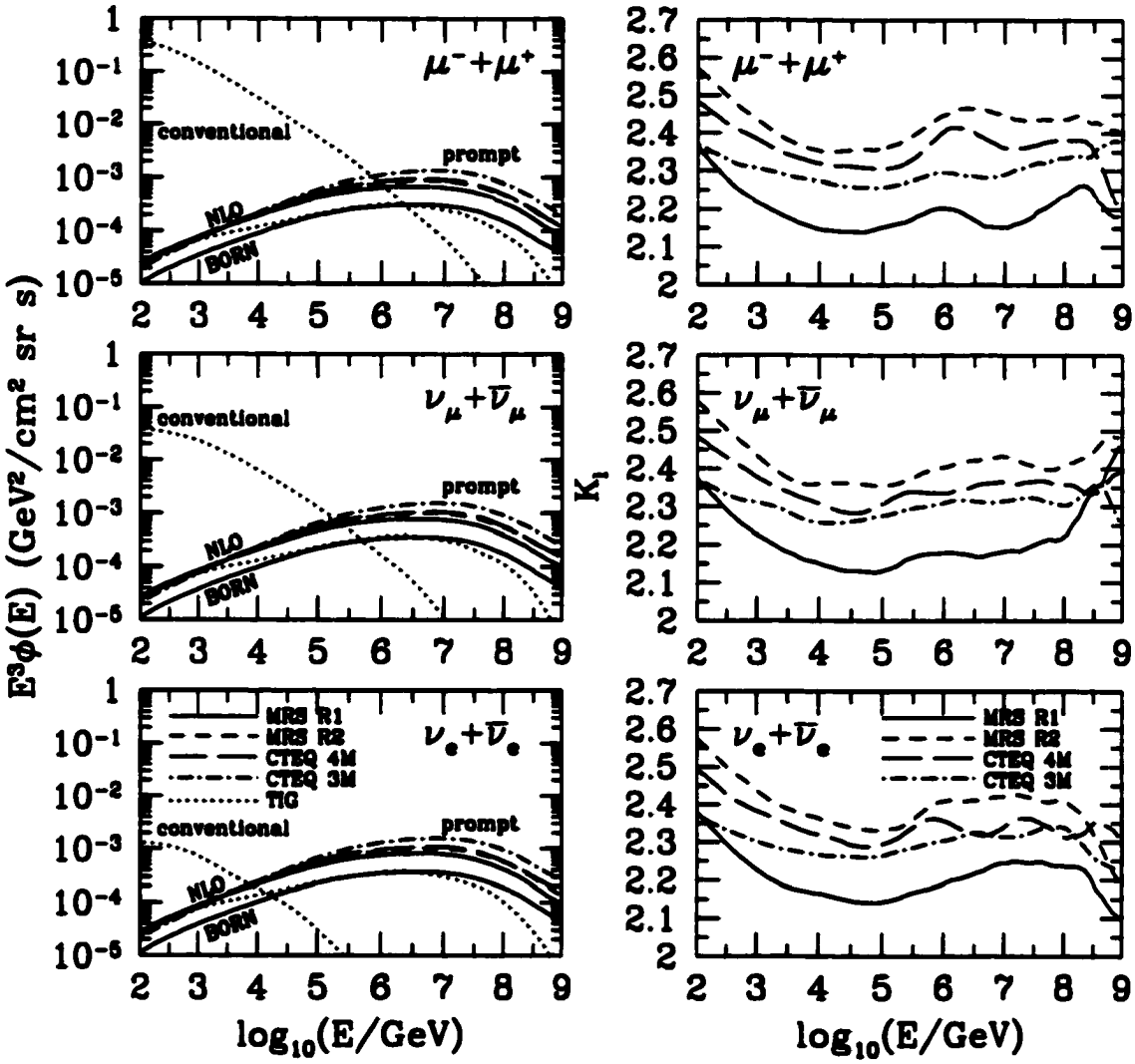

Figure 2.5: E^3-weighted vertical prompt fluxes, for different PDF's, at NLO (for MRS R1 we also show the Born flux), for the three types of leptons considered, compared to the TIG [15] conventional and prompt fluxes (left figures) and the related K_l factors for each case (right figures).

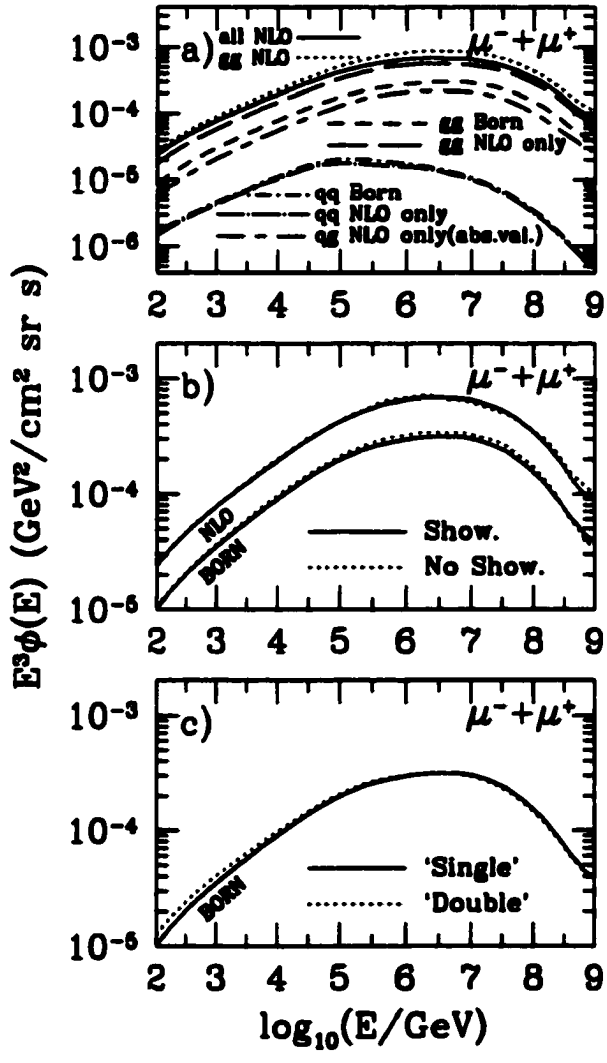

Figure 2.6: (a) Contributions of the different Born and NLO processes to the total E^3-weighted vertical prompt fluxes. (b) Comparison of the fluxes with or without the showering option, at Born and NLO. (c) Comparison of the fluxes calculated in the 'single' or 'double' mode, at Born only (PDF: MRS R1).

Chapter 3

Part Two: Dependence on the Gluon Distribution Function

3.1 Introduction to Part Two

We recall from Part One that the flux of atmospheric neutrinos and muons at very high energies, above 1 TeV, originates primarily from semileptonic decays of charmed particles instead of pions and kaons, which are the dominant decay modes at lower energies. This flux is one of the most important backgrounds for "neutrino telescopes", limiting their sensitivity to astrophysical signals, especially for future km^3 detectors which might be able to observe neutrinos and muons at extremely high energies, even up to 10^{12} GeV.

We use perturbative QCD (pQCD), the theoretically preferred model, to compute the charm production. We perform a true next-to-leading order (NLO) pQCD analysis of the production of charmed particles in the atmosphere, together with a full simulation of the particle cascades down to the final muons and neutrinos. This is done by combining the NLO pQCD calculations of charm production and

computer routines of Mangano, Nason, and Ridolfi [19, 20] (called MNR in the following) with the computer simulations of the cascades generated by PYTHIA [28]. These are the same programs currently used to compare pQCD predictions with experimental data in accelerator experiments.

We have already presented results of our calculations in the first part, in which all the details of the program we use can be found. The main goal of this first part was to compare the fluxes obtained with the NLO and the leading order (LO) calculations, i.e. we computed the K factor for the neutrino and muon fluxes. This was done to improve on the first study of atmospheric fluxes based on pQCD, performed by Thunman, Ingelman, and Gondolo a few years ago in Ref. [15] (called TIG in the following). TIG used the LO charm production cross section computed by PYTHIA, multiplied by a constant K factor of 2 to bring it in line with the NLO values, and supplemented by parton shower evolution and hadronization according to the Lund model.

In Chapter Two we found the K factors for different parton distribution functions (PDF's), as function of energy, to be in a range between 2.1 and 2.5. A similar analysis was recently made in Pasquali, Reno, and Sarcevic [21] (called PRS from now on), with results compatible with ours, using a treatment of the problem complementary to ours. In fact, PRS used approximate analytic solutions to the cascade equations in the atmosphere, also introduced by TIG, while we make instead a full simulation of the cascades.

In Chapter Two we showed that the approach used by TIG (i.e. multiplying the LO fluxes by an overall K factor of 2) was essentially correct, except for their relative low K factor (since K values of 2.2 - 2.4, depending slightly on the PDF, provide estimates of the NLO within about 10%). However, while TIG found neutrino and muon fluxes lower than the lowest previous estimate, we found instead larger fluxes

(by factors of 3 to 10 at the highest energies, about 10^9 GeV), in the bulk part of previous predictions. The main reason for this difference is studied in this chapter.

Here we explore the dependence of the atmospheric fluxes on the extrapolation of the gluon PDF at very small partonic momentum fraction x, $x \lesssim 10^{-5}$, which is crucial for the fluxes at high energies. As explained below, the relevant momentum fraction x of the interacting atmospheric parton is of the order of the inverse of the leptonic energy E_l (in the atmospheric rest frame) in GeV. This energy, in turn, is of the order of 0.1 E, where E is the energy per nucleon of the incoming cosmic ray in the laboratory frame (the atmospheric rest frame). Thus, for $E_l \gtrsim 10^5$ GeV, we need the PDF's at $x \lesssim 10^{-5}$, values of x which are not reached experimentally. The final fluxes depend mostly on the gluon PDF, since this is by far the dominant one at these small x values and charm is mostly produced through gluon-gluon fusion processes.

A concern that has been expressed to us several times is the applicability of the MNR NLO-pQCD calculations, mostly done for accelerator physics, to the different kinematic domain of cosmic rays. In response we remark that, for the less steep extrapolations of the gluon structure function $g(x)$ that we use at small x, we have large logarithms, known as "ln(1/x)" terms, where $x \simeq \sqrt{4m_c^2/s}$, s is the hadronic center of mass squared energy and this x is the average value of the hadron energy fraction needed to produce the $c\bar{c}$ pair. With the extrapolation $g(x) \simeq x^{\lambda-1}$ (see below) and λ close to 0.5, and possibly for the intermediate choices of λ also, there should be no large logarithm. The problem arises for λ too close to zero. Moreover, contrary to the case in accelerators, we do not have the uncertainty present in the differential cross sections [19] when k_T is much larger than m_c, due to the presence of large logarithms of $(k_T^2 + m_c^2)/m_c^2$. Because we do not have here a forward cut in acceptance, the characteristic transverse charm momentum in our simulations is of

the order of the charm mass, $k_T \simeq O(m_c)$.

In this part, as in Chapter Two, the MNR program is used to compute the inclusive charm cross section, and the cascades simulated by PYTHIA are initiated by a single c quark. This is the 'single' mode described in Part One, where we argued its advantages. We explained there our normalization of the NLO charm production cross sections in the MNR program, and described in detail the computer simulations used to calculate the neutrino and muon fluxes, which we briefly review in Sections 3.2 and 3.3. Except for the inclusion of the NLO calculations our model closely follows TIG. In Section 3.4 we show the neutrino and muon fluxes we obtain for different low x behaviors of the gluon PDF and we compare them with the TIG fluxes. In Section 3.5, we give analytic arguments that explain and support our results.

Finally, as in Part One (and TIG), we consider only vertical showers for simplicity.

3.2 Charm production in pQCD and choice of PDF's

Our NLO calculation is based on the MNR computer code. The NLO cross section for charm production depends on the choice of the parton distribution functions and on three parameters: the charm quark mass m_c, the renormalization scale μ_R, and the factorization scale μ_F. In order to calibrate the charm production routines we fit the most recent experimental data [11, 12, 13, 14] (differential and total cross sections) with one and the same combination of m_c, μ_R, and μ_F, for each PDF we use (see Part One for complete details). Several choices of m_c, μ_R and μ_F may

work equally well. In fact the cross sections increase by decreasing μ_F, μ_R or m_c, so changes in the three variables can be played against each other to obtain practically the same results. We use just one such choice for each PDF. We intend to further study the uncertainty related to this range of possible choices in Part Three.

3.2.1 Choice of m_c, μ_R, μ_F

As in Chapter Two, here we use the PDF's MRS R1, R2 [22] and CTEQ 4M [24], with the following parameters. We choose $\mu_R = m_T$, $\mu_F = 2m_T$ for all sets, where m_T is the transverse mass, $m_T = \sqrt{k_T^2 + m_c^2}$, and

$$m_c = 1.185 \text{ GeV} \quad \text{for MRS R1}, \tag{3.1}$$

$$m_c = 1.31 \text{ GeV} \quad \text{for MRS R2}, \tag{3.2}$$

$$m_c = 1.27 \text{ GeV} \quad \text{for CTEQ 4M}. \tag{3.3}$$

The data we use for this 'calibration' of the MNR program are shown in Table 1 and Table 2 of the second chapter. In this part, we add to our list of PDF's the latest of the MRS set, the MRST [31], with charm mass

$$m_c = 1.25 \text{ GeV} \quad \text{for MRST}, \tag{3.4}$$

obtained with the same procedure used for the other PDF's.

As we will see clearly in Sect. 3.5, due to the steep decrease with increasing energy of the incoming flux of cosmic rays, only the most energetic charm quarks produced will count, and these come from the interactions of projectile partons carrying a large fraction of the incoming nucleon momentum. Thus, the characteristic x of the projectile parton, that we call x_1, is large. It is $x_1 \simeq O(10^{-1})$. We can,

then, immediately understand that very small partonic momentum fractions are needed in our calculation, because typical partonic center of mass energies $\sqrt{\hat{s}}$ are close to the $c\bar{c}$ threshold, $2m_c \simeq 2$ GeV (since the differential cross section decreases with increasing $\hat{s}$) while the total center of mass energy squared is $s = 2m_N E$ (with m_N the nucleon mass, $m_N \simeq 1$ GeV). Calling x_2 the momentum fraction of the target parton (in a nucleus of the atmosphere), then $x_1 x_2 \equiv \hat{s}/s = 4m_c^2/(2m_N E) \simeq$ GeV$/E$. Thus, $x_2 \simeq O(\text{GeV}/0.1E)$, where E is the energy per nucleon of the incoming cosmic ray in the lab frame. The characteristic energy E_c of the charm quark and the dominant leptonic energy E_l in the fluxes are $E_l \simeq E_c \simeq 0.1E$, thus $x_2 \simeq O(\text{GeV}/E_l)$. Namely $x_2 \simeq 10^{-6}, 10^{-7}$ at $E_l \simeq 1, 10$ PeV.

3.2.2 Choice of PDF's

For $x > 10^{-5}$ ($E \lesssim 10^3$ TeV), PDF's are available from global analyses of existing data. We use four sets of PDF's. Three of these, MRS R1, MRS R2 [22] and CTEQ 4M [24] (used also in Part One), incorporate most of the latest HERA data and cover the range of parton momentum fractions $x \geq 10^{-5}$ and momentum transfers $Q^2 \geq 1.25 - 2.56$ GeV^2. MRS R1 and MRS R2 differ only in the value of the strong coupling constant α_s at the Z boson mass: in MRS R1 $\alpha_s(M_Z^2) = 0.113$, and in MRS R2 $\alpha_s(M_Z^2) = 0.120$. The former value is suggested by "deep inelastic scattering" experiments, and the latter by LEP measurements. This difference leads to different values of the PDF parameters at the reference momentum $Q_0^2 = 1.25$ GeV^2, where the QCD evolution of the MRS R1 and R2 PDF's is started. The CTEQ 4M is the standard choice in the $\overline{MS}$ scheme in the most recent group of PDF's from the CTEQ group ($\alpha_s(M_Z^2) = 0.116$ for CTEQ 4M). In this part we also use the very recent MRST [31]. This new PDF set includes all the latest experimental

measurements that have become available and, for the first time, an investigation of the uncertainty in the gluon distribution function. We will use the main choice of the MRST set, the "central gluon" MRST, related to the central value of the gluon PDF's of the package, which is considered the optimum global choice of this new set. The range in Q^2 and x of MRST set is the same as for the older MRS R1-R2 ($x \geq 10^{-5}$ and $Q^2 \geq 1.25$ GeV^2), and $\alpha_s(M_Z^2) = 0.1175$.

For $x \ll 1$, all these PDF's go as

$$x f_i(x, Q^2) \simeq A_i x^{-\lambda_i(Q^2)}, \tag{3.5}$$

where i denotes valence quarks u_v, d_v, sea quarks S, or gluons g. The PDF's we used have $\lambda_S(Q_0^2) \neq \lambda_g(Q_0^2)$, in contrast to older sets of PDF's which assumed an equality. As x decreases the density of gluons grows rapidly. At $x \simeq 0.3$ it is comparable to the quark densities but, as x decreases it increasingly dominates over them. Quark densities become negligible at $x \lesssim 10^{-3}$.

The PDF's need to be extrapolated to $x < 10^{-5}$ ($E \gtrsim 10^3$ TeV). Extrapolations based on Regge analysis usually propose $xg(x) \sim x^{-\lambda}$ with $\lambda \simeq 0.08$ [26], while evolution equations used to resum the large logarithms $\alpha_s \ln(1/x)$ mentioned before, such as the BFKL (Balitsky, Fadin, Kuraev, Lipatov [27]) find also $xg(x) \sim x^{-\lambda}$, but with $\lambda \simeq 0.5$.

In this work we use extrapolations with different values of λ. For the older MRS R1-R2 and CTEQ 4M we consider only the two extreme behaviors and the intermediate one that we used in Part One, namely: (i) a constant extrapolation $\lambda_g(Q^2) = 0$ for $x \leq 10^{-5}$; (ii) a linear extrapolation of $\ln g(x)$ as a function of $\ln x$, $\ln g(x) = -(\lambda_g(Q^2) + 1) \ln x + \ln A_g$, where $\lambda_g(Q^2)$ is taken at $x = 10^{-5}$, the smallest x for which the PDF's are provided (we call λ(R1), λ(R2) or λ(4M) the λ's

so obtained); (iii) an extrapolation with $\lambda_g(Q^2) = 0.5$ for $x \leq 10^{-5}$. Cases (i) and (iii) are extreme choices theoretically justified before [26], while (ii) is somewhat in between, with a resulting $\lambda \simeq 0.2 - 0.3$.

For the new MRST we have included several values of λ, in order to test the dependence on this parameter in a more complete way: (i) extrapolations with different λ's, i.e. $\lambda_g(Q^2) = 0, 0.1, 0.2, 0.3, 0.4, 0.5$ for $x \leq 10^{-5}$; (ii) we also included the linear extrapolation of $\ln g(x)$ as a function of $\ln x$, similar to the second intermediate choice of the previous list; we will call λ(T) the λ obtained in this way.

3.3 Simulation of particle cascades in the atmosphere

In this section we briefly describe the computer simulation used to calculate the neutrinos and muons fluxes; a more detailed description can be found in Chapter Two. The charm production process in the atmosphere and the particle cascades are simulated by modifying and combining together two different programs: the MNR routines [19] and PYTHIA 6.115 [28].

The MNR program was modified to become an event generator for charm production at different heights in the atmosphere and for different energies of the incoming primary cosmic rays.

The charm quarks (and antiquarks) generated by this first stage of the program are then fed into a second part which handles quark showering, fragmentation and the interactions and decays of the particles down to the final leptons. The cascade evolution is therefore followed throughout the atmosphere: the muon and neutrino fluxes at sea level are the final output of the process.

In order to make our results comparable to those of TIG, we keep the same modeling of the atmosphere and of the primary cosmic ray flux as in TIG and the same treatment of particle interactions and decays in the cascade.

We recall however that our main improvements are the inclusion of a true NLO contribution for charm production, the use of updated PDF's and, in this second part, the different extrapolations used for the gluon PDF at low x.

In the rest of this section we review briefly the model for the atmosphere and the primary flux used in this study, which was introduced originally by TIG.

We assume a simple isothermal model for the atmosphere. Its density at vertical height h is

$$\rho(h) = \frac{X_0}{h_0} e^{-h/h_0}, \tag{3.6}$$

with the parameters, scale height $h_0 = 6.4$ km and column density $X_0 = 1300$ g/cm^2 at $h = 0$, chosen as in TIG to fit the actual density in the range 3 km $< h <$ 40 km, important for cosmic ray interactions. Along the vertical direction, the amount of atmosphere traversed by a particle, the depth X, is related to the height h simply by

$$X = \int_h^\infty \rho(h')dh' = X_0 e^{-h/h_0}. \tag{3.7}$$

The atmospheric composition at the important heights is approximately constant: 78.4% nitrogen, 21.1% oxygen and 0.5% argon with average atomic number $\langle A \rangle =$ 14.5.

Following TIG [15], we neglect the detailed cosmic ray composition and consider all primaries to be nucleons with energy spectrum

$$\phi_N(E,0)\left[\frac{nucleons}{cm^2\ s\ sr\ GeV\ /\ A}\right] = \phi_0 E^{-\gamma-1} = \tag{3.8}$$

$$= \left\{ \begin{array}{ll} 1.7\ (E/GeV)^{-2.7} & for\ E < 5\ 10^6\ GeV \\ 174\ (E/GeV)^{-3.0} & for\ E > 5\ 10^6\ GeV \end{array} \right\}$$

The primary flux is attenuated as it penetrates into the atmosphere by collisions against the air nuclei. An approximate expression for the intensity of the primary flux at a depth X is (see [15] again)

$$\phi_N(E, X) = e^{-X/\Lambda_N}\ \phi_N(E, 0)\ . \tag{3.9}$$

The nuclear attenuation length Λ_N, defined as

$$\Lambda_N(E) = \frac{\lambda_N(E)}{1 - Z_{NN}(E)}\ , \tag{3.10}$$

has a mild energy dependence through λ_N and Z_{NN}, the spectrum-weighted moment for nucleon regeneration in nucleon-nucleon collisions. We use the Z_{NN} values in Fig. 4 of Ref. [15]. The interaction thickness λ_N is

$$\lambda_N(E, h) = \frac{\rho(h)}{\sum_A \sigma_{NA}(E) n_A(h)}\ , \tag{3.11}$$

where $n_A(h)$ is the number density of air nuclei of atomic weight A at height h and $\sigma_{NA}(E)$ is the total inelastic cross section for collisions of a nucleon N with a nucleus A. This cross section scales essentially as $A^{2/3}$, $\sigma_{NA}(E) = A^{2/3}\sigma_{NN}(E)$. For $\sigma_{NN}(E)$ we use the fit to the available data in Ref. [30]. Using our height independent atmospheric composition, we simplify Eq. (3.11) as follows,

$$\lambda_N(E, h) = \frac{\langle A \rangle}{\langle A^{2/3} \rangle}\ \frac{\mathrm{u}}{\sigma_{NN}(E)} = 2.44\ \frac{\mathrm{u}}{\sigma_{NN}(E)}\ . \tag{3.12}$$

Here $\langle\ \rangle$ denotes average and u is the atomic mass unit, that we write as

$$u = 1660.54 \text{ mb g/cm}^2. \tag{3.13}$$

Therefore in our approximations $\lambda_N(E)$ is independent of height.

3.4 Neutrino and muon fluxes

We present here the results of our simulations with all the PDF's and the values of λ described in Section 3.2.

3.4.1 Total cross sections

The NLO total inclusive charm-anticharm production cross sections $\sigma_{c\bar{c}}$ for our four different PDF's are shown in Fig. 3.1 over the energy range needed by our program, $E \leq 10^{11}$ GeV. In the top part of the figure we compare the results of MRS R1-R2 and CTEQ 4M (with their different values of λ described before) to the cross section used in the TIG model. In the bottom part we show the same comparison, done just with the new MRST, with its different λ's (in all these figures cross sections increase for increasing values of λ).

All these cross sections were calculated using the MNR program, with the 'calibration' described in Sect. 3.2, up to the NLO contribution. We can see in the figure that all our cross sections agree at low energies, as expected due to our 'calibration' at 250 GeV, and are very similar for energies up to 10^6 GeV. Beyond this energy they start showing their dependence on the λ value and also a slight dependence on the PDF used, which was already noticed in Part One. As it can be seen from both parts of the figure, the increase of the cross sections with λ is evident at the

highest energies: at the maximum energy considered the cross sections for the two extreme values of λ differ by almost a factor of ten.

We also notice that, for energies above 10^4 GeV, our cross sections are always considerably higher than the one used by TIG. As we have already explained in the first part, TIG used an option of PYTHIA by which the gluon PDF is extrapolated for $x \leq 10^{-4}$ with $\lambda = 0.08$. In fact the TIG cross section at the highest energies shows the same slope of our results for $\lambda \simeq 0$, but it is always lower than our lowest cross sections by about a factor of three.

This can be explained only in part by the fact that the TIG cross section up to NLO is the LO result obtained with PYTHIA, multiplied by a constant K factor of 2, while at large energies the K factor is actually larger than 2 by about 10-15%. The bulk of the difference is however due to the different evaluations of the cross sections, even at LO, done by the MNR routines (our method) and directly by PYTHIA (approach used by TIG).

3.4.2 Prompt atmospheric fluxes

Our results for the prompt fluxes are shown in Figs. 3.2–3.5, for MRS R1-R2, CTEQ 4M and MRST.

In Figs. 3.2 and 3.3 we show the E_ℓ^3-weighted vertical prompt fluxes $E_\ell^3 \phi_\ell$, calculated to NLO, for muons and muon-neutrinos, together with the fluxes from TIG, both from prompt and conventional sources (dotted lines). The flux of electron-neutrinos is practically the same as that of muon-neutrinos. Fig. 3.4 describes the spectral index of the differential fluxes, defined as $\alpha_\ell = -\partial \ln \phi_\ell / \partial \ln E_\ell$.

The effects of the different extrapolations of $g(x)$ to $x < 10^{-5}$ (see Sect. 3.2) are noticeable at $E_\ell \gtrsim 10^5$ GeV. In Figs. 3.2 and 3.3, the E_ℓ^3-weighted fluxes increase

with λ: they can differ by up to two orders of magnitude at the highest energy considered, 10^9 GeV, for the two extreme choices of λ. This behavior is similar for all the PDF's considered.

The λ dependence of the fluxes can also affect the energy at which the prompt contribution dominates over the conventional sources: this is particularly true for the muon fluxes as it can be seen in Fig. 3.2; for the $\nu_\mu + \bar{\nu}_\mu$ fluxes this effect is less important (see Fig. 3.3) and it doesn't exist for the $\nu_e + \bar{\nu}_e$ fluxes, for which the conventional contribution is much lower. Apart from these differences due to the λ values, charm decay dominates over conventional sources at $E_\mu \gtrsim 10^6$ GeV for muons, $E_{\nu_\mu} \gtrsim 10^5$ GeV for muon-neutrinos, and $E_{\nu_e} \gtrsim 10^4$ GeV for electron-neutrinos.

We also see that all our fluxes for $\lambda \simeq 0$ are similar to those of TIG at energies above 10^6 GeV. We have already mentioned that TIG used a very low value of λ, $\lambda = 0.08$. It is remarkable that, for these low values of λ, we obtain similar final fluxes in spite of the differences of the two simulations and of the total cross sections already noted in Fig. 3.1.

We can also compare our fluxes to those of the recent PRS results [21]. As we have already noticed in Part One, for intermediate values of λ our results are very similar to the PRS ones. From Fig. 3.3, for example, we see that our fluxes for the $\lambda = 0.3$ case (calculated with MRST) are close to the corresponding PRS results shown in Fig. 8 of Ref. [21], calculated with CTEQ 3M and $\lambda \simeq 0.3$. Our results are lower than the PRS by $30 - 50\%$ at the highest energies, which is probably due to the PDF's used and to the different approach of the two groups.

Regarding the dependence of the spectral index α_ℓ on the slope λ of the gluon PDF, we notice in Fig. 3.4 that, for all four PDF's, above about 10^6 GeV the differences in slope between the $\lambda = 0$ and $\lambda = 0.5$ fluxes is about 0.5, suggesting

that the spectral index is $\alpha_\ell(E_\ell) = b_\ell(E_\ell) - \lambda$, namely,

$$\phi_\ell(E_\ell) \sim {E_\ell}^{-\alpha_\ell(E_\ell)} = {E_\ell}^{-b_\ell(E_\ell)+\lambda}, \tag{3.14}$$

where $b_\ell(E_\ell)$ is an energy dependent coefficient, that can be read off directly from the $\lambda = 0$ curve ($b_\ell(E_\ell)$ is the spectral index for $\lambda = 0$). We will justify this result in Sect. 3.5. Due to this linear dependence of the spectral index on λ, given a model which specifies the function $b_\ell(E_\ell)$, the value of λ could be determined through a measurement of any of the ϕ_ℓ fluxes at two different energies. We will study in detail this possibility in the next chapter.

Here we only comment on the typical rates in a km^3 detector. It can be estimated from the curves of Fig. 3.2 that the number of prompt atmospheric muons traversing a km^3 detector from above would be over 100 per year around a muon energy of 1 PeV, decreasing rapidly to less than 1 per year above 100 PeV. In this energy range there is a concrete possibility of detecting these prompt muons. Notice that the intensity of the prompt muon flux depends critically on the value of λ, suggesting still another way to estimate λ through the measurement of the fluxes.

In Fig. 3.5 we study the dependence of the prompt fluxes on the PDF for fixed values of λ. We summarize our previous results for $\lambda = 0$ (left) and for $\lambda = 0.5$ (right), and compare them again to TIG. The figures on the top show the E_ℓ^3-weighted fluxes, those on the bottom the spectral indices. As we already noticed in Part One, the dependence on the PDF is not strong, all fluxes are very similar. This indicates that our procedure for the 'calibration' of our simulation with different PDF's (described in Sect. 3.2) is good. There are, however, some differences between the PDF's: in some cases (especially for $\lambda = 0$) the results of MRS R2 and CTEQ 4M are very similar and higher than those of MRS R1 and MRST (also very close

to each other). The maximum difference between all these fluxes is at the level of 30 to 70% at high energies.

We want here to remark once more that our $\lambda = 0$ fluxes are very close to that of TIG at energies above 10^6 GeV (and also below 10^3 GeV, but the prompt fluxes are not important at these low energies). For increasing values of λ, our results are higher than TIG, even by two orders of magnitude for $\lambda = 0.5$, and at the highest energies. From the bottom part of the figure we notice that also the spectral indices are almost independent of the PDF used. This indicates that the linear dependence between α_ℓ and λ of Eq. (3.14) is not affected by the choice of the PDF and again might be used to determine the value of λ. We will return on this analysis in more details in the next chapter.

3.5 Analytic insight

In this section we first find the characteristic values of the partonic momentum fractions in the cosmic ray nucleus and in the nucleus in the atmosphere, and then derive the linear relation between the slope of the atmospheric muon (or neutrino) fluxes and the slope of the gluon parton distribution function.

3.5.1 Characteristic values of partonic momentum fractions

We first show that the characteristic values of the partonic momentum fractions of the incoming cosmic ray parton, x_1, and of the target parton belonging to a nucleus in the atmosphere, x_2, are respectively,

$$x_1 \simeq 10^{-1} \quad x_2 \simeq (E/10\ \text{GeV})^{-1} \tag{3.15}$$

where E is the energy of the incoming nucleon (a proton in this paper) in the atmosphere reference frame. Because of the small value of x_2, for the relevant energies $E \gtrsim 10^4$ GeV, the gluon density $g(x_2)$ is much larger than the density of quarks, which we, thus, neglect in these analytic arguments.

Let us first consider the charm flux at production $d\phi_c(E_c, X)/dX$, defined as the rate of c quark production[1] per unit area, unit depth and unit charm energy (E_c in the atmosphere reference frame) in the interactions of the attenuated nucleon flux $\phi_N(E, X)$ with the air nuclei in the atmospheric layer between X and $X + dX$. To obtain $d\phi_c(E_c, X)/dX$ for a layer of transverse area $\mathcal{A}$ and height $|dh|$, we simply multiply the c production rate per air nucleus (which equals the incoming nucleon flux at depth X times the cross section for $N + A \to c + Y$, where Y stands for "anything" and N is simply a proton p in our study) by the number of nuclei A in the layer (which is $\mathcal{A}|dh|n_A(h)$) and divide the result by the transverse area $\mathcal{A}$ and the layer thickness $dX = \rho(h)|dh|$. We find

$$\frac{d\phi_c(E_c, X)}{dX} = \sum_{\mathrm{A}} \frac{n_{\mathrm{A}}(h)}{\rho(h)} \int_{E_c}^{\infty} dE\, \phi_{\mathrm{N}}(E, X)\, \frac{d\sigma(\mathrm{pA} \to \mathrm{cY}; \mathrm{E}, \mathrm{E_c})}{dE_c}. \tag{3.16}$$

We assume that the charm production cross section simply scales as A, which is expected when it is much smaller than the total inelastic cross section. In this case, the sum over A becomes trivial, and we have (u is the atomic mass unit)

$$\frac{d\phi_c(E_c, X)}{dX} = \frac{1}{\mathrm{u}} \int_{E_c}^{\infty} dE\ \phi_N(E, X)\, \frac{d\sigma(pN \to cY; E, E_c)}{dE_c}\ . \tag{3.17}$$

In these analytical considerations, we assume a simple power law for the primary

[1]This is what we compute in our simulations (we use our 'single' mode), only the production of a c quark is calculated. Then the result is multiplied by two to include the contribution of the antiquark (see Part One for details).

flux and an energy independent attenuation length.[2] With these approximations, the attenuated primary flux reads

$$\phi_N(E, X) = \phi(X) E^{-\gamma-1}, \tag{3.18}$$

where $\phi(X) = \phi_0 \exp(-X/\Lambda_N)$. Substituting this approximate expression for the attenuated primary flux and changing the integration variable from E to $x_E = E_c/E$ in Eq. (3.17), we find

$$\frac{d\phi_c(E_c, X)}{dX} = \frac{\phi(X)}{\mathrm{u}} E_c^{-\gamma-1} \int_0^1 dx_E \, x_E^{\gamma} \frac{d\sigma(pN \to cY; x_E, E_c)}{dx_E} \,. \tag{3.19}$$

The differential cross section $d\sigma(pN \to cY)/dx_E$ is given in terms of the partonic differential cross section $d\hat{\sigma}_{ij}/dx_E$ (where i and j are partons belonging to the projectile 1 and the target 2 respectively), and the PDF's $f_i^1(x_1, \mu_F^2)$ and $f_j^2(x_2, \mu_F^2)$ as

$$\frac{d\sigma(pN \to cY)}{dx_E} = \sum_{ij} \int dx_1 dx_2 f_i^1(x_1, \mu_F^2) f_j^2(x_2, \mu_F^2) \frac{d\hat{\sigma}_{ij}}{dx_E}. \tag{3.20}$$

Here x_1 and x_2 are the momentum fractions of the projectile and target partons. Mangano et al. [19] give the partonic cross section in terms of functions h_{ij} as

$$E_c \frac{d\hat{\sigma}_{ij}}{d^3k} = \frac{\alpha_s^2(\mu_R)}{\hat{s}^2} h_{ij}(\tau_x, \tau_2, \rho, \mu_R, \mu_F), \tag{3.21}$$

where k and E_c are the momentum and energy of the produced c quark, and,

[2]The dependence of Λ_N on E is actually very mild. In fact the whole factor $e^{-X/\Lambda_N(E)}$ behaves like $E^{-\beta}$ with $\beta \simeq 0.1$ for $E \geq 10^6$ GeV and β even smaller for $E \leq 10^6$ GeV. Including this contribution in our analytic argument would just mean to replace γ with $\gamma + \beta$ everywhere, i.e. the total spectral index would become $\gamma + 1 + \beta \simeq 3.1$ instead of 3.0, for energies above the knee at $E = 5\ 10^6$ GeV. This slight change can actually be seen in our results of Fig. 3.8 (see the description of that figure).

in the notation of Ref. [19], $\rho \equiv 4m_c^2/\hat{s}$, $\tau_x = 1 - \tau_1 - \tau_2$, $\tau_1 \equiv (k \cdot p_1/p_1 \cdot p_2)$, $\tau_2 \equiv (k \cdot p_2/p_1 \cdot p_2)$ and $\hat{s} \equiv (p_1 + p_2)^2$, while p_1 and p_2 are the projectile and target parton momenta respectively, $p_1 = x_1 P_1, p_2 = x_2 P_2$. The hats indicate quantities in the partonic center of mass (those without hats are in the lab frame at rest with the atmosphere).

In the partonic center of mass frame, the projectile and target parton momenta are

$$\hat{p_1} = \left(\frac{\sqrt{\hat{s}}}{2}, 0, 0, \frac{\sqrt{\hat{s}}}{2}\right), \quad \hat{p_2} = \left(\frac{\sqrt{\hat{s}}}{2}, 0, 0, -\frac{\sqrt{\hat{s}}}{2}\right), \quad \hat{k} = \left(\hat{E}_c, 0, \hat{k}_T, \hat{k}\right), \tag{3.22}$$

and we have

$$\tau_2 = \frac{\hat{E}_c + \hat{k}}{\sqrt{\hat{s}}}, \quad \tau_x = 1 - \frac{2\hat{E}_c}{\sqrt{\hat{s}}}. \tag{3.23}$$

Then, after integration over azimuthal angles,

$$\frac{d^3k}{E_c} = \frac{d^3\hat{k}}{\hat{E}_c} = 2\pi d\ \hat{E}_c d\hat{k} = \pi \hat{s} d\tau_2 d\tau_x. \tag{3.24}$$

The kinematic bounds $m_c \leq \hat{E}_c \leq \sqrt{\hat{s}}/2$ and $|\ \hat{k}| \leq \sqrt{\hat{E}_c^2 - m_c^2}$ fix the integration domains of τ_2 and τ_x. Using $\rho = 4m_c^2/\hat{s}$, we get $(1-\sqrt{1-\rho})/2 \leq \tau_2 \leq (1+\sqrt{1-\rho})/2$ and $0 \leq \tau_x \leq 1 - \tau_2 - (\rho/4\tau_2)$. We can use the relation

$$x_E = \frac{E_c}{E} = \frac{k \cdot P_2}{P_1 \cdot P_2} = x_1 \frac{k \cdot p_2}{p_1 \cdot p_2} = x_1 \tau_2, \tag{3.25}$$

to write the differential cross section in dx_E as

$$\frac{d\hat{\sigma}_{ij}}{dx_E} = \int d^3k \frac{d\hat{\sigma}_{ij}}{d^3k} \delta(x_E - x_1\tau_2). \tag{3.26}$$

The bound $x_1 x_2 = \hat{s}/s \geq 4m_c^2/2m_p E = 4\epsilon x_E$ (m_p is the proton mass, $m_p \simeq$

1 GeV), where we define

$$\epsilon = \frac{m_c^2}{2m_p E_c}, \tag{3.27}$$

implies that x_1 and x_2 have a minimum lower bound larger than zero. In fact, $x_1 \geq 4\epsilon x_E/x_2 \geq 4\epsilon x_E$ (since $x_2 \leq 1$). Taking x_1 as the independent variable, then $4\epsilon x_E \leq x_1 \leq 1$ and $4\epsilon x_E/x_1 \leq x_2 \leq 1$. We now change the order of the integrations, in order to perform the integration in x_E before the integrations in x_1, x_2 and τ_2.

The integration over x_E in Eq. (3.19) then becomes trivial, amounting to the replacement of x_E^γ by $x_1^\gamma \tau_2^\gamma$, except for the necessary changes in the integration domains which become $0 \leq x_1, x_2, \tau_2 \leq 1$ and $0 \leq x_E \leq (x_1 x_2/\epsilon)\tau_2(1-\tau_2)$. For the $\delta(x_E - x_1\tau_2)$ in Eq. (3.26) to yield a non-zero result, we need to take $0 \leq x_1\tau_2 \leq (x_1 x_2/\epsilon)\tau_2(1-\tau_2)$, which means that $\tau_2 \leq 1 - (\epsilon/x_2)$, and given that $\tau_2 \geq 0$, this means $x_2 \geq \epsilon$. This leads to a factorization of the x_1 and x_2 integrations as follows:

$$\int_0^1 dx_E\, x_E^\gamma \frac{d\sigma(pN \to cY)}{dx_E} = \frac{\pi\alpha_s^2(\mu_R)}{m_c^2} \times \sum_{ij} \int_0^1 \left[dx_1 x_1^\gamma f_i^1(x_1, \mu_F^2)\right] \left[\int_\epsilon^1 dx_2 f_j^2(x_2, \mu_F^2) \zeta_{ij}\left(\frac{\epsilon}{x_2}, \mu_R, \mu_F\right)\right], \tag{3.28}$$

where the functions ζ_{ij} are defined as

$$\zeta_{ij}(v, \mu_R, \mu_F) = v \int_0^{1-v} d\tau_2\, \tau_2^{\gamma+1} \int_0^{1-v-\tau_2} d\tau_x\, h_{ij}(\tau_x, \tau_2, 4v\tau_2, \mu_R, \mu_F)\,, \tag{3.29}$$

and the argument v is $v \equiv \epsilon/x_2$ (to rewrite the integration in τ_2 we noticed that $\rho/4\tau_2 = v$). The functions h_{ij} are given by $h_{ij}(\tau_x, \tau_2, \rho, \mu_R, \mu_F) = h_{ij}^{(0)}(\tau_2, \rho)\delta(\tau_x) + O(\alpha_s^2)$. We will take only gluons as partons from now on, thus $f_i^1(x, \mu_F^2) = f_j^2(x, \mu_F^2) = g(x, \mu_F^2)$.

The function ζ_{gg}, using h_{gg} at the Born level, is shown in Fig. 3.6a for $\gamma = 1.7$ and 2 (corresponding to the spectral indices $\gamma + 1$ of the primary flux above and

below the knee). In the same figure we see that the maximum of $\zeta_{gg}(v)$ is at $v \simeq 0.1$, namely $x_2 \simeq 10\ \epsilon$. However, given that $g(x_2, \mu_F^2)$ is a sharply increasing function with decreasing x_2 (i.e. for increasing v at fixed E_c), the maximum of the product $g(x_2, \mu_F^2)\zeta_{gg}(v)$ is always to the right of the maximum of $\zeta_{gg}(v)$, at $v > 0.1$. Therefore, the integral in x_2 is dominated by the values of x_2 of order ϵ, namely

$$x_2 \simeq \epsilon \simeq \frac{\text{GeV}}{2E_c}\ . \tag{3.30}$$

Also, the integral in x_1 shows that large values of x_1 will be dominant since $x_1^\gamma g(x_1) \to x_1^{\gamma-\lambda-1}$ for small x, where the exponent is positive, since $\gamma = 1.7$ or 2, while $0 \leq \lambda \leq 0.5$ (thus $\gamma - \lambda - 1 > 0$). To see more precisely what range of x_1 dominates the integral, it is necessary to prove two statements. The first is that $\tau_2 \equiv x_E/x_1 < 1$, due to kinematical constrains, therefore $x_1 > x_E$. The second is that the characteristic value of x_E is 0.1, namely that the c-quark is mainly produced with 0.1 of the proton energy

$$E_c = \mathcal{O}(0.1\ E). \tag{3.31}$$

With respect to the kinematical limit on τ_2, as we already mentioned, $\tau_2 \equiv x_E/x_1 \leq 1 - v$, and we obtained as a kinematical constraint that $\epsilon \leq v = \epsilon/x_2 \leq 1$ (since x_2 goes from ϵ to 1). Thus, $\tau_2 \leq 1 - \epsilon < 1$, since ϵ is always larger than zero. Another way of obtaining this bound is the following. Since the partonic processes involved are $gg \to c\bar{c}$ or $gg \to c\bar{c}g$, then $\sqrt{\hat{s}} \geq 2(\hat{E}_c)_{\max}$ and due to $m_c \neq 0$, $(\hat{k})_{\max} < (\hat{E}_c)_{\max}$, therefore $\tau_2 < 2(\hat{E}_c)_{\max}/\sqrt{\hat{s}} \leq 1$.

That in fact $E_c = \mathcal{O}(0.1\ E)$ is clearly demonstrated in Fig. 3.6b, which shows the function $x_E^\gamma(d\sigma/dx_E)$ normalized by the total c-production cross section. Thus

we have proven that the dominant range of x_1 is $x_1 \geq \mathcal{O}(0.1E)$ and also, combining together Eq. (3.30) and Eq. (3.31), our statement in Eq. (3.15) about x_2.

Even if we have not yet included gluon shadowing in our calculations, we want to point out that this effect might only be important for the target gluon (given that x_2 is very small) but it is not important for the gluons in the projectile (given that $x_1 \geq 0.1$). This means that the uncertainties on the composition of cosmic rays will not affect the results through shadowing effects.

As a summary of our arguments we can say that, due to the incoming flux being rapidly falling with increasing energy of the primary, only the charm quarks produced with a large fraction of the incoming energy, $E_c \simeq 0.1E$, will count in the charm flux at production, and those highly energetic c quarks come from projectile partons carrying a large fraction of the incoming momentum $x_1 \geq x_E \simeq 0.1$. On the other hand, because typical partonic center of mass energies $\sqrt{\hat{s}}$ are close to the $c\bar{c}$ threshold, $2m_c \simeq 2$ GeV (since the cross section decreases steeply with increasing $\sqrt{\hat{s}}$), while the total center of mass energy squared is $s = 2m_pE$ (with m_p the proton mass, $m_p \simeq 1$ GeV), the product $x_1x_2 \equiv \hat{s}/s = 4m_c^2/(2m_pE) \simeq \text{GeV}/E$. This shows that $x_2 \simeq (\text{GeV}/Ex_1) \simeq \text{GeV}/0.1E$.

3.5.2 Atmospheric fluxes and dependance on λ

We now derive the dependence on λ of the muon and neutrino fluxes for a simple power law primary flux.

We can explain first the dependence on λ of the spectral index of $d\phi_c/dX$ at large energies, and then, using this result, the dependence on λ of the spectral indices of atmospheric muons and neutrinos. To start with, we notice that the integral for $d\phi_c/dX$ depends on the charm energy E_c only through the presence of the

parameter ϵ in the integration on x_2. To approximately perform this integration at large energies, let us replace $g(x_2) \simeq x_2^{-\lambda-1}$ in that integral and take $\zeta(\epsilon/x_2) \simeq \zeta_{\max}$ (namely develop ζ in powers of $v = \epsilon/x_2$ and keep only the constant term) then

$$\int_\epsilon^1 dx_2\; g(x_2)\; \zeta\left(\frac{\epsilon}{x_2}\right) \simeq \zeta_{\max} \int_\epsilon^1 dx_2\; x_2^{-\lambda-1}\;. \tag{3.32}$$

Since $\epsilon \ll 1$, this integral is well approximated by $\zeta_{\max}\epsilon^{-\lambda}/\lambda$, for all $\lambda \neq 0$. Better approximations to the function ζ give similar results. For example, approximating the function ζ by two power laws, one above and another below the maximum, which is at about $x_2 = 5\epsilon$ ($\zeta = \zeta_{\max}(x_2/5\epsilon)^{2.1}$ for x_2 between ϵ and 5ϵ and $\zeta = \zeta_{\max}(5\epsilon/x_2)^{0.4}$ for x_2 between 5ϵ and 1), the integral in Eq.(3.32) becomes $\zeta_{\max}(5\epsilon)^{-\lambda}/(0.9 + 1.7\lambda - \lambda^2)$. Thus the essential dependence of $\epsilon^{-\lambda}$ is maintained. Recalling that $\epsilon = m_c^2/(2\, m_p\, E_c)$, Eq. (3.19) is proportional to E_c^λ, and the same is true for Eq. (3.32), therefore

$$\frac{d\phi_c}{dX}(E_c, X) \sim E_c^{-\gamma-1+\lambda}\;. \tag{3.33}$$

The charm production function $d\phi_c(E_c, X)/dX$, calculated numerically, is shown in Fig. 3.7 for a typical $X = 57.12$ g/cm^2 ($h = 20$ km). We are using here the PDF MRS R1 with the three related values of $\lambda = 0$, λ(R1), 0.5. We clearly see here that the slope at $E_c \gtrsim 10^5$GeV depends on the extrapolation of the gluon PDF at $x < 10^{-5}$. This is one order of magnitude lower in energy than in Fig. 3.1 for the total cross section. This reflects the fact mentioned above that the characteristic charm energy is $E_c = \mathcal{O}(0.1E)$. Fig. 3.8 shows that, as predicted analytically, the slopes (the negative of the spectral index in our notation) of the charm fluxes at production depend almost linearly on λ. In fact, in Fig. 3.8, we can see that

the logarithmic slopes of the $\lambda = 0$ and $\lambda = 0.5$ fluxes differ precisely by 0.5, above 5 10^6 GeV (namely, above the knee) to about 10^9 GeV (the maximum energy at which our fluxes are reliable, given that we take 10^{11} GeV as the maximum incoming proton energy E). In fact, the slope of the $\lambda = 0$ flux in that interval is about -3.1 to -3.2, while that of the $\lambda = 0.5$ flux is about -2.6 to -2.7. Above the knee, the primary spectrum goes as E^δ with $\delta \simeq (-\gamma - 1 - 0.1) = -3.1$, where we have also included the 0.1 contribution coming from the E-dependence of Λ_N (see footnote in previous discussion), thus the charm spectrum, (in the energy range 10^7 GeV $\lesssim E_c \lesssim 10^9$ GeV) goes approximately as $E_c^{\delta+\lambda}$ as expected from Eq. (3.33).

Using the definition of the leptonic fluxes in terms of the charm spectrum at production $d\phi_c/dX$, we can now find the dependence of the spectral index of muon and neutrino fluxes with λ. For example, the differential flux ϕ_μ of muons with energy E_μ (μ stands here for μ^+ or μ^-) is

$$\phi_\mu(E_\mu) = 2\int_{X_0}^{\infty} dX \int_{E_\mu}^{\infty} dE_c \frac{d\phi_c(E_c, X)}{dX} \left[\frac{dN_\mu(c \to \mu; E_c, E_\mu, X)}{dE_\mu}\right] \qquad (3.34)$$

(ϕ_μ has, thus, units of [1/ cm^2 s sr GeV]). Here the factor of 2 accounts for the muons produced by $\bar{c}$ and the last square bracket is the number of muons of energy E_μ produced at sea level by the cascades, each cascade initiated by a c quark of energy E_c at a depth X.

Our results above indicate that we can write the atmospheric charm spectrum at production as (see Eq.(3.33)) $d\phi_c(E_c, X)/dX \simeq F(X)E_c^{-\gamma-1+\lambda}$ with $F(X)$ a function independent of energy. Replacing this form for $d\phi_c(E_c, X)/dX$ in Eq.

(3.34) and multiplying and dividing by $E_\mu^{-\gamma-1+\lambda}$ we can write ϕ_μ as

$$\phi_\mu(E_\mu) = 2E_\mu^{-\gamma-1+\lambda} \int_{X_0}^{\infty} dX F(X) \int_{E_\mu}^{\infty} dE_c \left(\frac{E_c}{E_\mu}\right)^{-\gamma-1+\lambda} \left[\frac{dN_\mu(c \to \mu; E_c, E_\mu, X)}{dE_\mu}\right]. \tag{3.35}$$

We can argue that in so far as the values of the parent charm quark energy E_c and the daughter lepton energy E_μ are not very different, the dependence of the integral on λ (and on γ) should be mild. In this case, from Eq. (3.35), we find that the spectral index of the muon (and similarly of the neutrino) flux contains λ as a term, i.e.

$$\phi_\mu(E_\mu) \simeq f(E_\mu, \gamma, \lambda) E_\mu{}^{-\gamma-1+\lambda} \equiv E_\mu^{-b_\mu(E_\mu,\gamma,\lambda)+\lambda}\ , \tag{3.36}$$

where the dependence of the function $f(E_\mu, \gamma, \lambda)$ on λ and γ should be mild. The function $b_\mu(E_\mu, \gamma, \lambda)$ should depend linearly on γ and again very mildly on λ. We will return on this in the next chapter. This justifies the results shown in Figs. 3.4 and 3.5, presented in Sect. 3.4, showing all the spectral indices obtained using all our PDF's.

Finally we examine the deviations from linearity of the relation between the spectral index α_ℓ and the gluon PDF slope λ. In Fig. 3.9a we show directly the relation between λ and α_ℓ, using the values coming from our simulation for the MRST case already presented in Fig. 3.4, but now plotting them for fixed energy E_μ. We show two examples, for $E_\mu = 1\ PeV,\ 10\ PeV$, where our points indicate a good agreement with the linear relation between α_ℓ and λ of Eq. (3.14).

The mild dependence on λ of the functions $b_\ell(\lambda) = \alpha_\ell + \lambda$ can be seen in Fig. 3.9b, where we show the percentage difference $[b_\ell(\lambda) - b_\ell(0)]/b_\ell(0)$ for the different values of $\lambda = 0 - 0.5$ with the MRST PDF. It is evident that, in the range where our theoretical arguments are applicable (for $E_\mu \gtrsim 10^6$ GeV) the $b_\ell(\lambda)$ functions differ

only by $2-3\%$ for different λ values, namely they are almost independent of λ, given one particular PDF. This analysis confirms the validity of Eq. (3.14), which leads to the possibility of obtaining information on λ at small parton fractions x not reachable in experiments, through the measurement of the fluxes. We will study this possibility in more detail in Chapter Four.

3.6 Conclusions for Part Two

The actual next-to-leading order perturbative QCD calculations of charm production cross sections, together with a full simulation of the atmospheric cascades, were used to obtain the vertical prompt fluxes of neutrinos and muons.

We have analyzed the dependence of the atmospheric fluxes on the extrapolation of the gluon PDF at very low x, which is related to the value of the parameter λ. This was done using four different sets of PDF's: MRS R1, MRS R2, CTEQ 4M and MRST, with variable λ in the range 0–0.5.

The charm production cross sections and the final lepton fluxes depend critically on λ for leptonic energies $E_l \gtrsim 10^5$ GeV, which correspond to $x \lesssim 10^{-5}$ GeV. We found that the fluxes vary up to almost two orders of magnitude at the highest energy considered, 10^9 GeV, for the different λ's in the allowed interval; on the contrary, for fixed λ, the results don't depend much on the choice of the PDF.

For the lowest values of λ ($\lambda \simeq 0-0.1$) our fluxes are very close to those of TIG [15], confirming that the very low flux prediction is mostly due to a low value of λ ($\lambda_{\rm TIG} \simeq 0.08$). For higher values of λ ($\lambda \simeq 0.2-0.5$) our results are in the bulk of previous predictions and, in particular, for $\lambda \simeq 0.3$ they are very close to a recent semi-analytical calculation [21] done with a similar value of λ.

We have also considered the dependence of the spectral index of the final fluxes

on the parameters of the model. From both, computer simulations and analytical considerations, we find that the spectral index α_ℓ of atmospheric leptonic fluxes depends linearly on λ as in Eq. (3.14).

This suggests the possibility of obtaining bounds on λ in "neutrino telescopes" for small values of x not reachable in colliders, if the spectral index of leptonic atmospheric fluxes could be determined by these telescopes. We will investigate this possibility in detail in the next part.

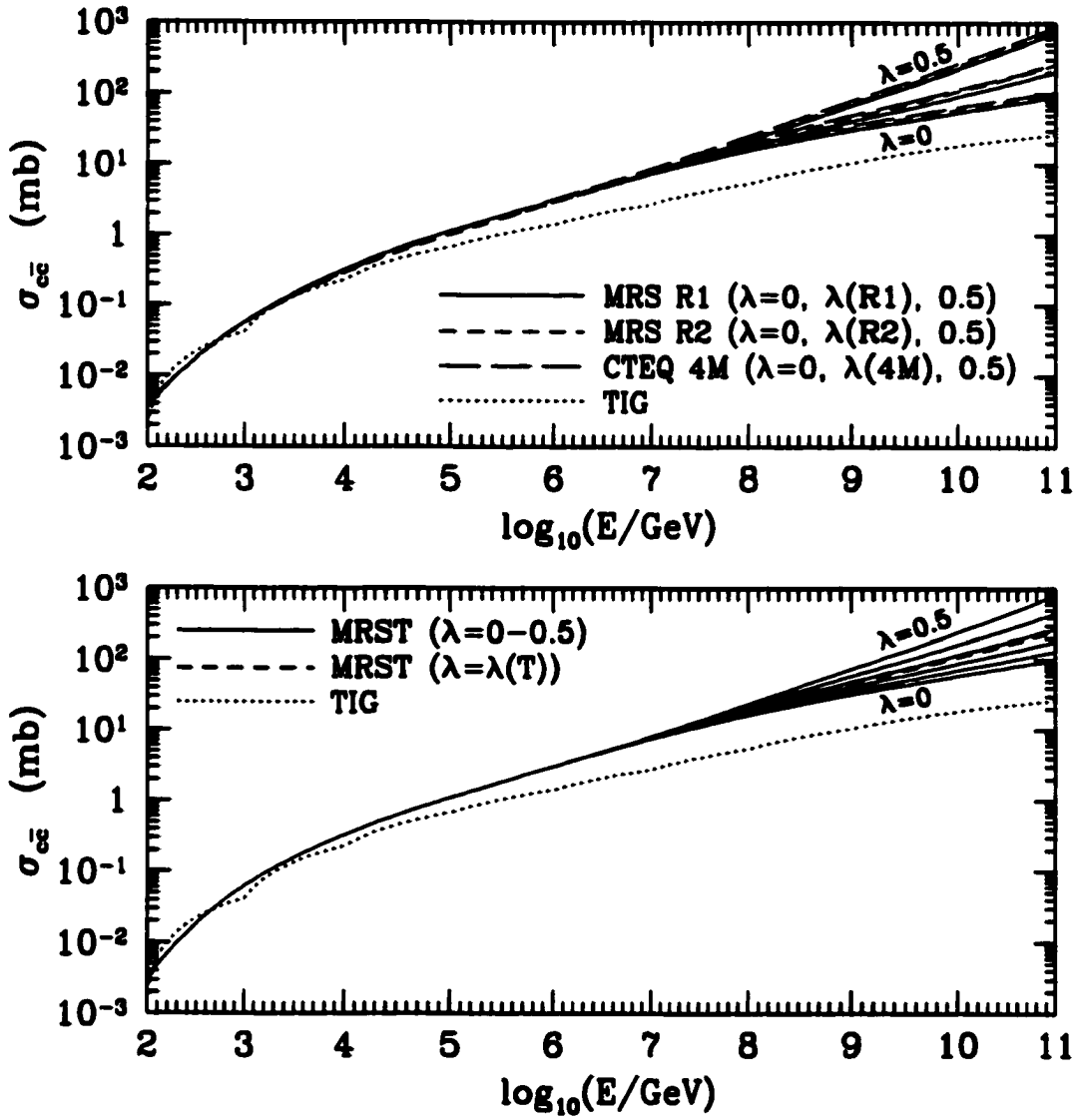

Figure 3.1: Total cross section for charm production $\sigma_{c\bar{c}}$, up to NLO, for our different PDF's and λ values, compared to that used by TIG [15]. Top panel: MRS R1-R2 and CTEQ 4M; bottom panel: MRST (cross sections increase with λ).

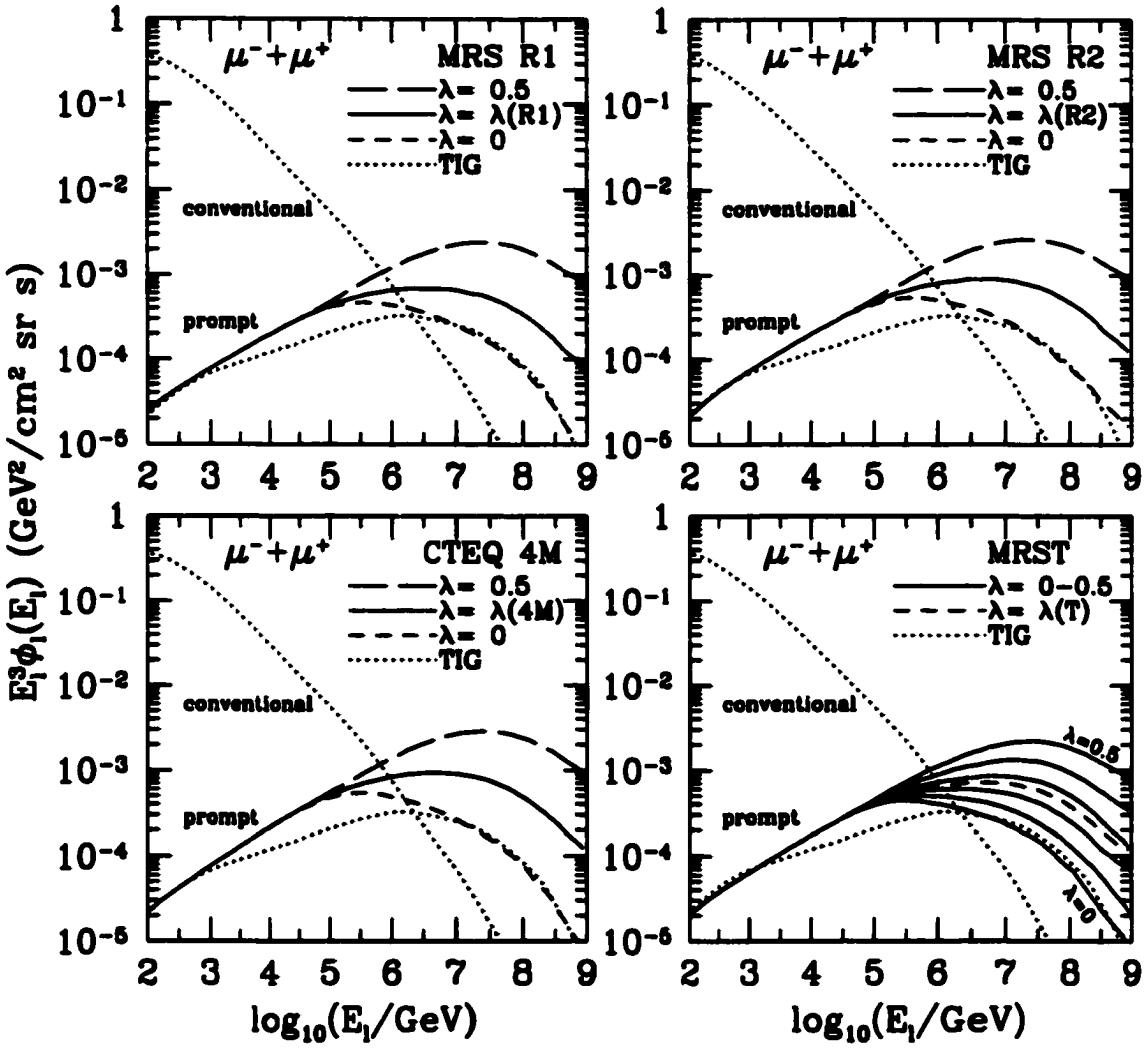

Figure 3.2: Prompt muons: E^3-weighted vertical fluxes at NLO, compared to the TIG [15] conventional and prompt fluxes (dotted lines). We show results using the four PDF's MRS R1, MRS R2, CTEQ 4M and MRST.

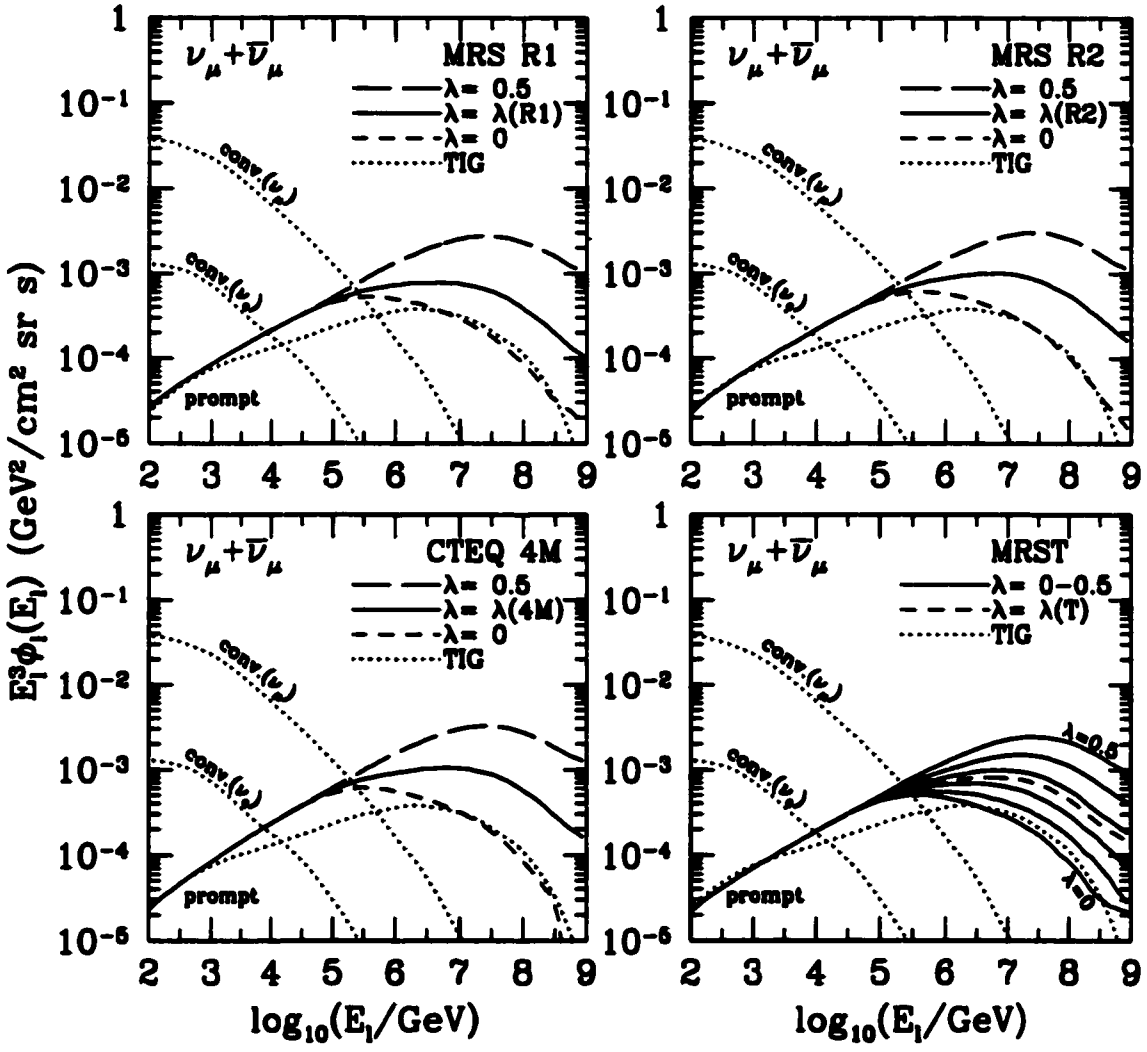

Figure 3.3: Prompt muon-neutrinos: E^3-weighted vertical fluxes at NLO, compared to the TIG [15] conventional and prompt fluxes (dotted lines). We show results using the four PDF's MRS R1, MRS R2, CTEQ 4M and MRST.

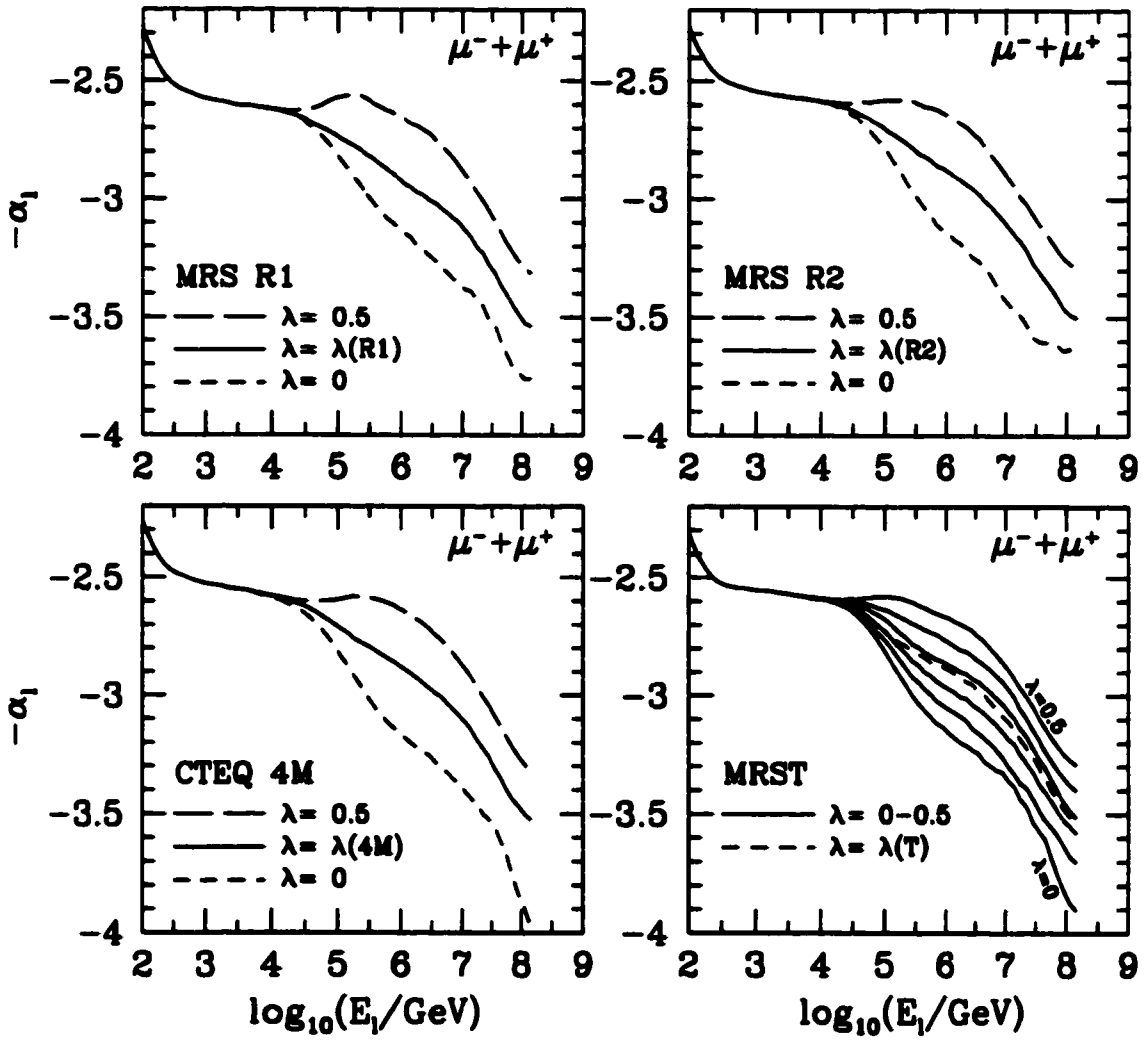

Figure 3.4: Prompt muons: spectral index of the NLO vertical fluxes for the four PDF's MRS R1, MRS R2, CTEQ 4M and MRST.

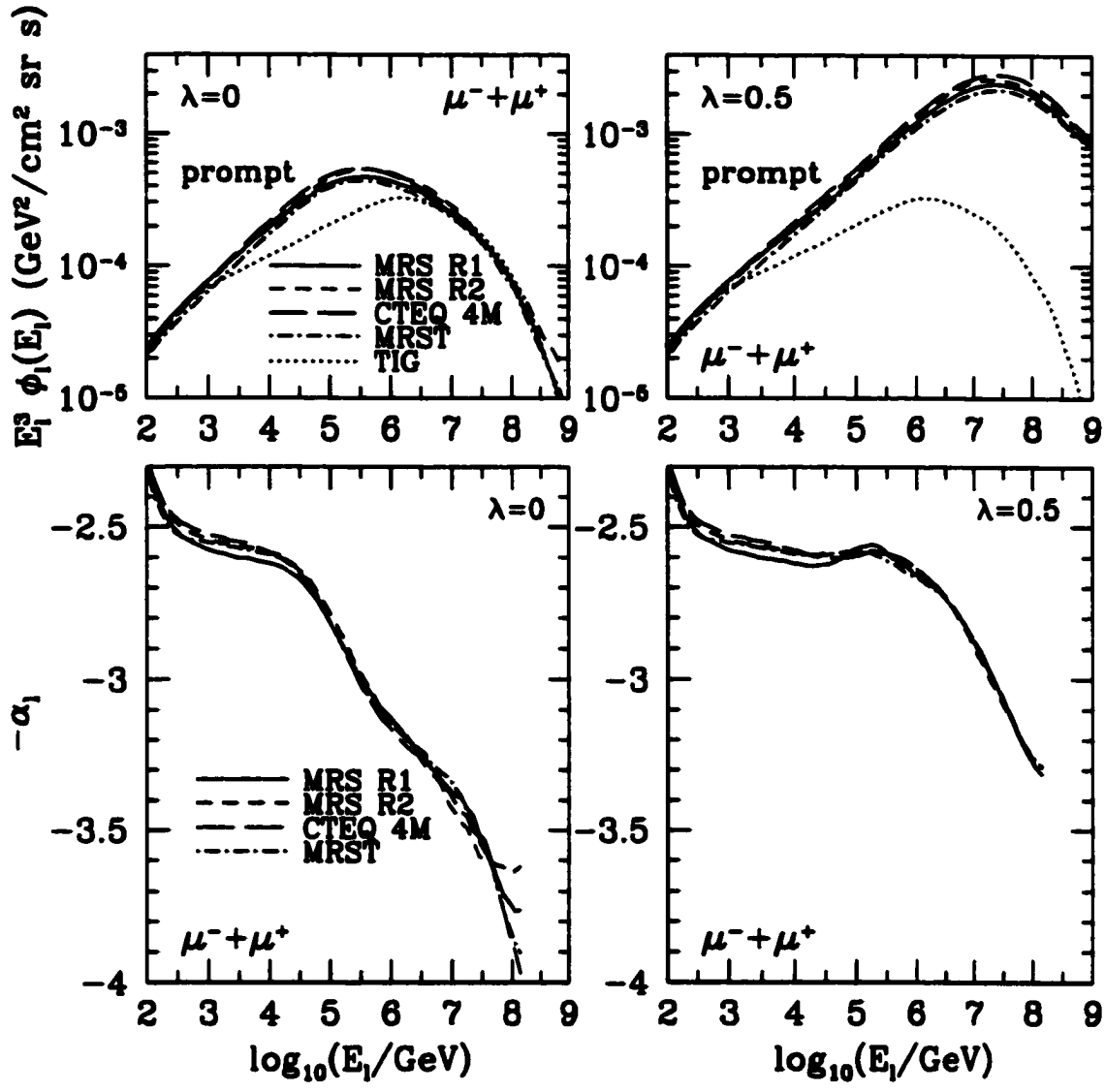

Figure 3.5: Dependence of prompt fluxes and their spectral index on the PDF at fixed λ: left side $\lambda = 0$, right side $\lambda = 0.5$.

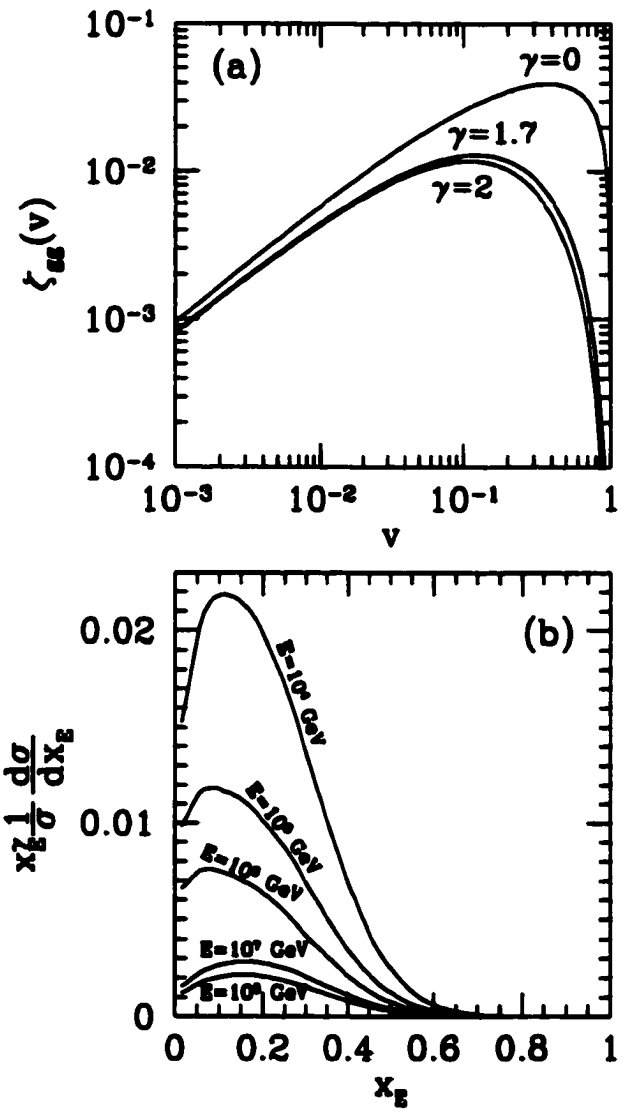

Figure 3.6: (a) The function $\zeta_{gg}(v)$ at the Born level for $\gamma = 0$, 1.7 (below the knee) and $\gamma = 2$ (above the knee). (b) Flux-weighted charm production spectra $x_E^{\gamma} \frac{1}{\sigma} \frac{d\sigma}{dx_E}$ at several beam energies (using MRS R1, λ(R1)).

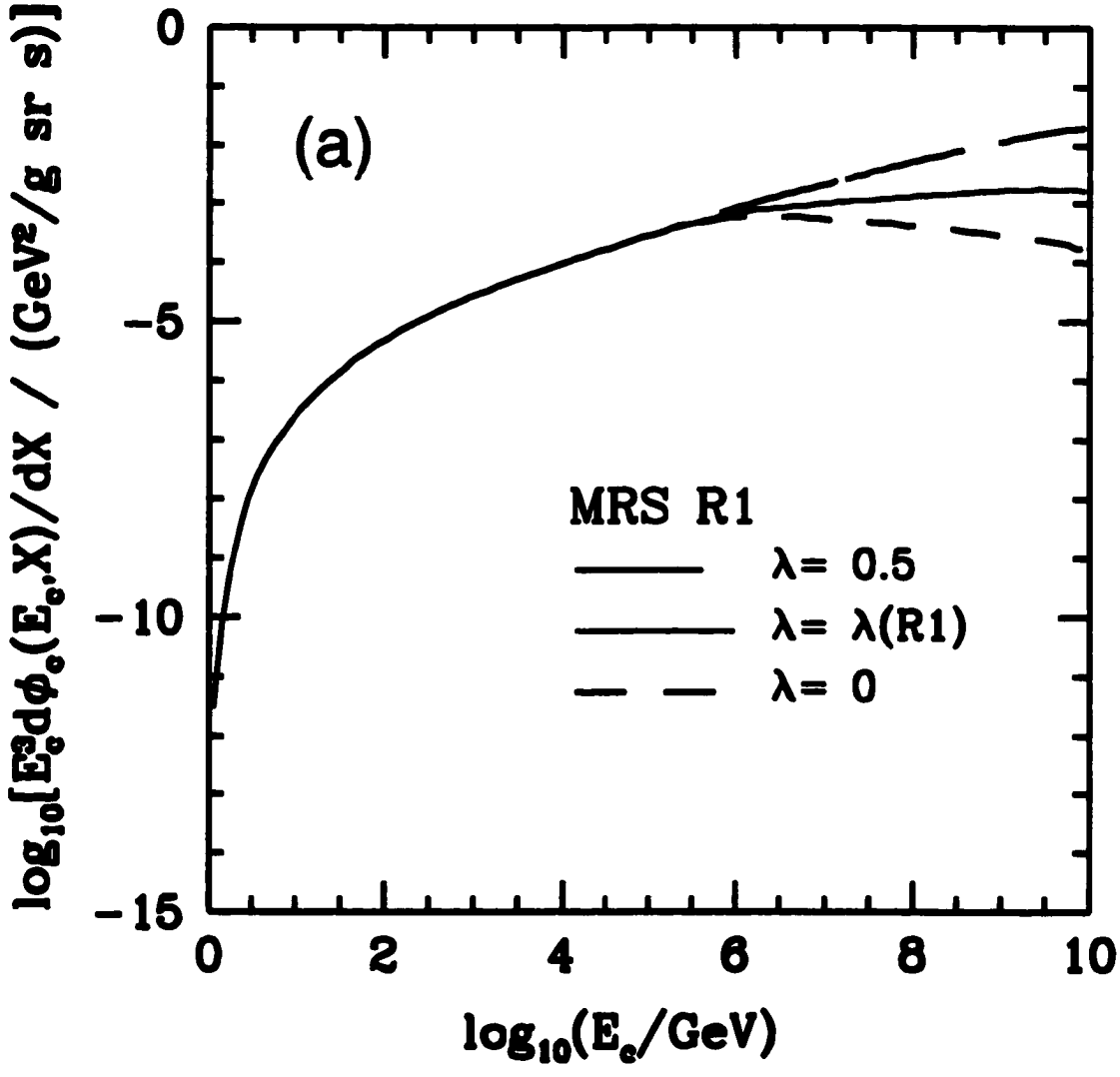

Figure 3.7: NLO charm production function $E_c^3 d\phi_c(E_c, X)/dX$ (PDF MRS R1).These results are for a height $h = 20$ km, corresponding to a vertical depth $X = 57.12$ g/cm^2 (similar results are obtained for other heights).

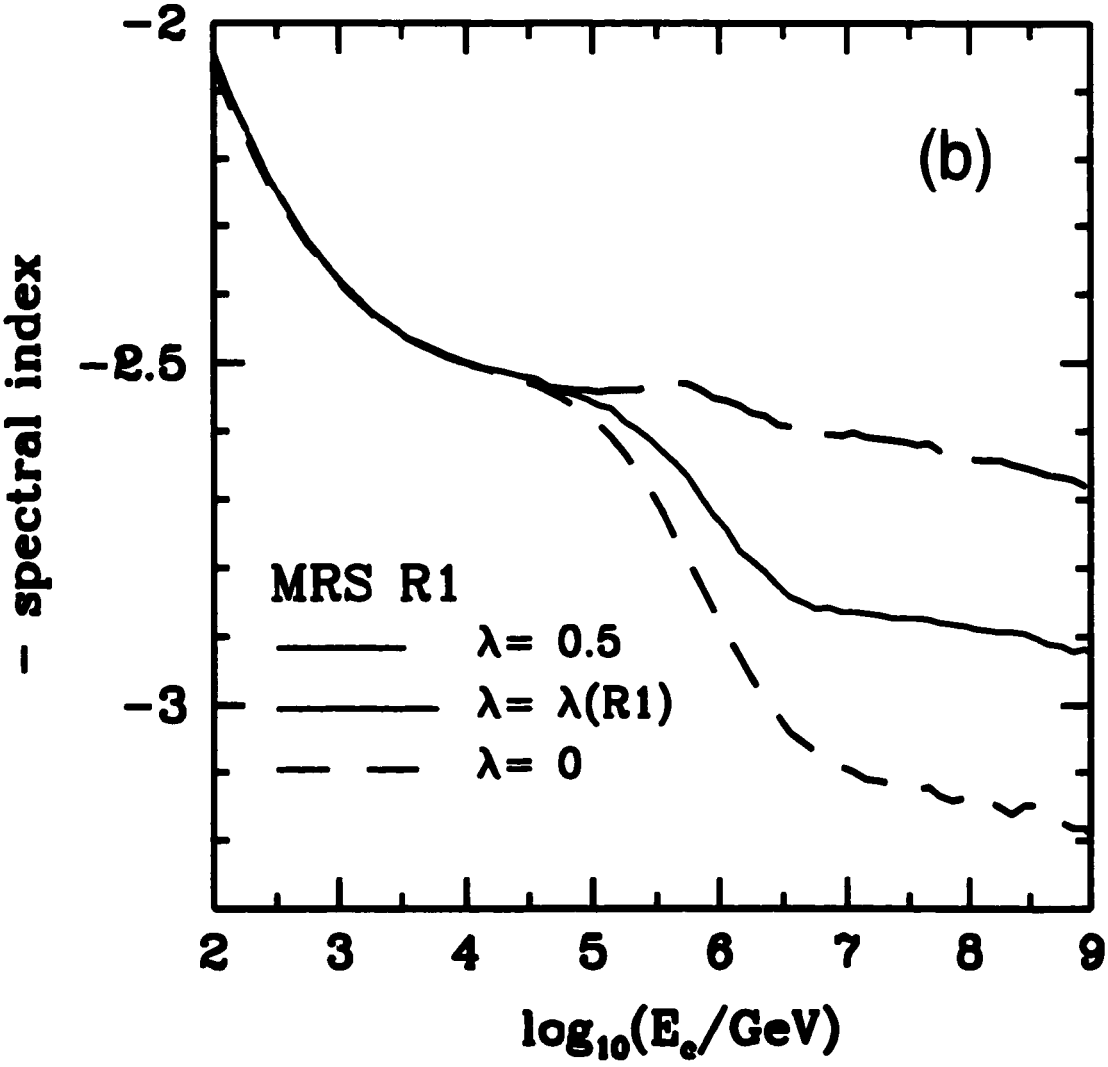

Figure 3.8: Spectral index of the charm production function

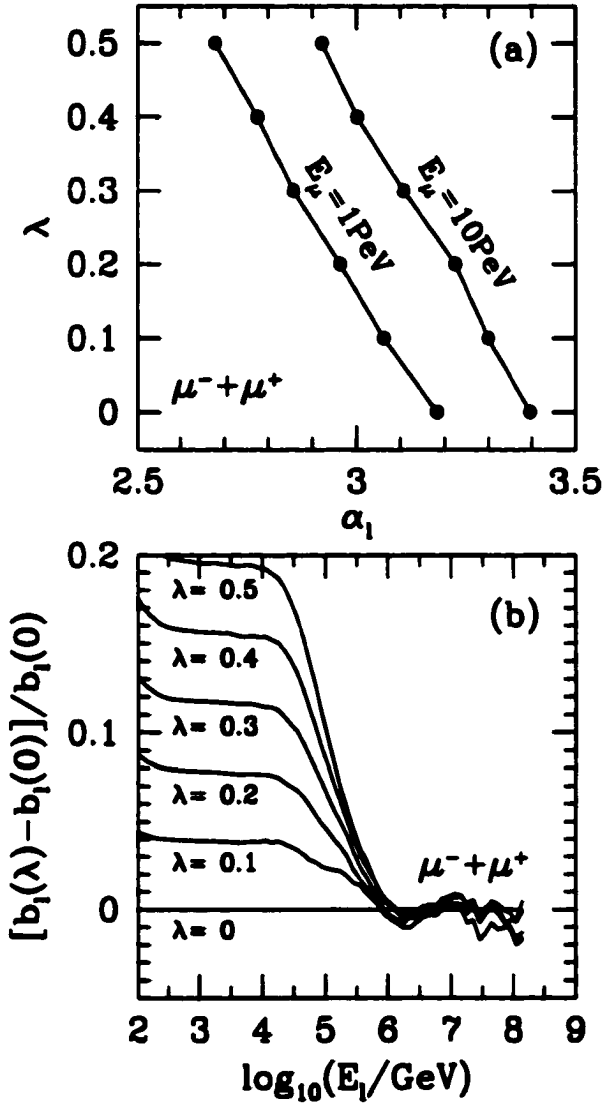

Figure 3.9: (a) Relation between the slope λ of the gluon PDF and the muon spectral index α_μ at fixed muon energy. (b) Non-linearities in this relation. Here $b_\ell(\lambda) = \alpha_\ell(\lambda) + \lambda$ and we use the MRST PDF.

Chapter 4

Part Three: Error Analysis and Measurement of the Gluon PDF at very low x

4.1 Introduction to Part Three

We recall once again that atmospheric neutrinos and muons are the most important source of background for present and future neutrino telescopes, which are expected to open a new window in astronomy by detecting neutrinos from astrophysical sources.

At energies above 1 TeV, atmospheric lepton fluxes have a prompt component consisting of neutrinos and muons created in semileptonic decays of charmed particles, as opposed to the conventional leptons coming from decays of pions and kaons. Thus a model for charm production and decays in the atmosphere is required.

We base our model on QCD, the theoretically preferred model, to compute the charm production. We use a next-to-leading order perturbative QCD (NLO pQCD)

calculation of charm production in the atmosphere, followed by a full simulation of particle cascades generated with PYTHIA routines [28].

We have already examined the prompt muon and neutrino fluxes in the two previous parts. In Part One, we found that the NLO pQCD approach produces fluxes in the bulk of older predictions (not based on pQCD) as well as of the recent pQCD semianalytical analysis of Pasquali, Reno and Sarcevic [21]. We also explained the reason of the low fluxes of the TIG model [15], the first to use pQCD in this context, which were due to the chosen extrapolation of the gluon partonic distribution function (PDF) at small momentum fractions x, and we confirmed the overall validity of their pioneering approach to the problem.

In Part Two, we analyzed in detail the dependence of the fluxes on the extrapolation of the gluon PDF at small x, which, according to theoretical models, is assumed to be a power law with exponent λ,

$$xg(x) \sim x^{-\lambda}, \tag{4.1}$$

with λ in the range 0–0.5. Particle physics experiments are yet unable to determine the value of λ at $x < 10^{-5}$. We found that the choice of different values of λ at $x < 10^{-5}$ leads to a wide range of final background fluxes at energies above 10^5 GeV.

Due to this result, in Part Two, we suggested the possibility of measuring λ through the atmospheric leptonic fluxes at energies above 10^5 *GeV*, not the absolute fluxes, because of their large theoretical error, but rather through their spectral index (i.e. the "slope"). In particular, we now propose to use the slope of the flux of down-going muons.

We want to stress that we are proposing to use *down-going muons*, at energies

$E_\mu \gtrsim 100\ TeV$, where prompt muons dominate over conventional ones, and not up-going neutrino-induced muons whose flux is orders of magnitude smaller. While an important contribution to up-going muons is expected from astrophysical neutrinos, there is no background for down-going atmospheric muons.

In this chapter we further investigate the possibility of measuring λ, in the more general context of an overall error analysis of our model.

We can identify five potential causes of uncertainty in our final results. The first one is the possible presence of large logarithms of the type $\alpha_s \ln p_T^2$ and $\alpha_s \ln s$ (the latter are the so called "$\ln 1/x$" terms). The second is the treatment of the multiplicity in the production of $c\bar{c}$ at high energies.

The third one consists of all the sources of uncertainty hidden in the treatment of particle cascades generated by PYTHIA. The fourth one is the uncertainty in the NLO pQCD charm production model we use. This includes the dependence of the fluxes on the three parameters of the model and the PDF's used. The fifth and final one is the choice of the primary cosmic ray flux, which is the input of our simulation. Of all these potential sources of uncertainty we conclude that only the last two are relevant.

We deal with these five potential sources of error in turn. In Sect. 4.2 we address the question of the large logarithms $\alpha_s \ln p_T^2$ and $\alpha_s \ln s$, and in Sect. 4.3 we analyze the problem of multiplicity in our charm production mechanism.

In Sect. 4.4 we consider the uncertainties due to the cascade generation by PYTHIA and to our NLO pQCD charm production (the core of our analysis). Here we evaluate the errors due to the parameters of the model, errors that affect the charm production cross section, the final differential and integrated fluxes and their spectral indices. We also determine how the final results (fluxes and their spectral indices) are affected by the choice of different extrapolations of the PDF's

at $x < 10^{-5}$.

We are finally ready in Sect. 4.5 to discuss how λ could be measured. We study the dependence on the different extrapolations of λ at $x < 10^{-5}$, we consider the spectral indices and, using the discussion of Sect. 4.4, we provide an estimate of the errors on these indices and examine the feasibility of an experimental determination of λ at $x < 10^{-5}$ with neutrino telescopes.

Finally in Sect. 4.6 we discuss the error on the determination of λ coming from the uncertainties in the elemental composition of the cosmic ray flux.

4.2 Importance of the $\alpha_s \ln 1/x$ terms

We address here a concern that has been expressed to us several times, about the applicability of perturbative QCD calculations, mostly done for accelerator physics, to the different kinematic domain of cosmic rays.

Contrary to the case in accelerators, we do not have the uncertainty present in the differential cross sections [19] when the transverse momentum p_T is much larger than m_c, uncertainty which is due to the presence of large logarithms of $(p_T^2 + m_c^2)/m_c^2$. The reason is that we do not have a forward cut in acceptance, and so the characteristic transverse charm momentum in our simulations is of the order of the charm mass, $p_T \simeq O(m_c)$, and not $p_T \gg O(m_c)$ as in accelerator experiments.

We may however, depending on the steepness of the gluon structure function λ, have large logarithms of the type $\alpha_s \ln s$, known as "$\ln(1/x)$" terms (here $x \simeq \sqrt{4m_c^2/s}$ is the average value of the hadron energy fraction needed to produce the $c\bar{c}$ pair at hadronic center of mass energy squared s). These "$\ln(1/x)$" terms arise when the t-channel gluon exchange becomes large, and eventually they have to be resummed. Although techniques exist for resumming these logarithms [32],

we have not done it. On the other hand we have phenomenologically altered the behavior of the parton distribution functions at small x by imposing a power law dependence of the form $xf(x) \sim x^{-\lambda}$. This is analogous to resumming the $\ln(1/x)$ terms in a universal fashion and absorbing them in an improved evolution equation for the gluon density (such as the Balitskyiĭ-Fadin-Kuraev-Lipatov (BFKL) evolution equation) [33], a procedure which increases λ. For sufficiently large λ, the large $\ln 1/x$ terms should not be present.

To find if our NLO $c\bar{c}$ cross sections are dominated by the $\ln 1/x$ terms, we have used the following qualitative criterion [34]. We have plotted the ratio

$$R = \frac{\sigma_{NLO} - \sigma_{LO}}{\sigma_{LO}\alpha_s \ln(s/m_c^2)/\pi} \tag{4.2}$$

as a function of the beam energy E. If the ratio is constant we are dominated by the $\ln 1/x$ terms and if it decreases we are not. The good behavior is a decreasing R. Figure 4.1 shows indeed that up to highest energy we consider in this paper, i.e. 10^{11} GeV, R decreases for $\lambda \gtrsim 0.2$, but is roughly constant for smaller λ's. This indicates that we are not dominated by the $\ln 1/x$ terms provided $\lambda \gtrsim 0.2$.

4.3 Multiplicity in charm production

Another concern is the fact that at high energies the charm production cross section we use, $\sigma_{c\bar{c}}$, is sometimes larger than the total pp cross section. At first sight this seems absurd, but we show here that $\sigma_{c\bar{c}}$ contains the charm multiplicity, i.e. it counts the number of $c\bar{c}$ pairs produced, and so can be larger than the total cross section. On the other hand, the inclusive charm production cross section, i.e. the cross section for producing at least one $c\bar{c}$ pair, is always smaller than the total pp

cross section.

We call σ_{QCD} the perturbative QCD cross section of $c\bar{c}$ pair production in pp collisions,

$$\sigma_{QCD} = \sum_{ij} \sigma_{QCD}(ij \to c\bar{c}), \tag{4.3}$$

where the sum is over the partons i and j in the colliding nucleons, and

$$\sigma_{QCD}(ij \to c\bar{c}) = \int dx_1 dx_2 dQ^2 \frac{d\hat{\sigma}(ij \to c\bar{c})}{dQ^2} f_i(x_1, \mu_F^2) f_j(x_2, \mu_F^2). \tag{4.4}$$

Here $d\hat{\sigma}(ij \to c\bar{c})/dQ^2$ is the $ij \to c\bar{c}$ parton scattering cross section, Q^2 is the four-momentum transfer squared, x_i is the fraction of the momentum of the parent proton carried by parton i, and $f_i(x, \mu_F^2)$ is the usual parton distribution function for parton momentum fraction x and factorization scale μ_F.

In the scattering of each pair of partons (one parton from the target and one from the projectile) only one $c\bar{c}$ pair may be produced, but the number of parton pairs interacting in each nucleon-nucleon collision is in general not limited to one and it increases with the number of partons $f(x, \mu_F^2)dx$ in each nucleon.

For λ close to 0.5, σ_{QCD} becomes larger than the total pp cross section $\sigma_{pp} \sim$ 200 mb at $E_p \sim 10^{10}$ GeV. It is obvious therefore that our results at high energy and large λ are unphysical, unless multiplicity is taken into account. In fact, multiparton interactions should be taken into account already at a smaller cross section of order 10 mb, as determined in studies of double parton scattering [35].

In order to incorporate multiparton scatterings into our analysis, we use an impact-parameter representation for the scattering amplitude, and ignore spin-dependent effects (cfr. [36]). Assuming the validity of factorization theorems, the mean number of parton-parton interactions $ij \to c\bar{c}$ in the collision of two protons

at impact parameter $\vec{b}$ is given by

$$n_{c\bar{c}}(\vec{b}) = \sum_{ij} \int d^2b' dx_1 dx_2 dQ^2 \frac{d\hat{\sigma}(ij \to c\bar{c})}{dQ^2} f_i(x_1, \mu_F^2, \vec{b'}) f_j(x_2, \mu_F^2, \vec{b} + \vec{b'}), \qquad (4.5)$$

where $f_i(x, \mu_F^2, \vec{b})d^2b$ is the number of partons i in the interval $(x,\ x + dx)$ and in the transverse area element d^2b at a distance $\vec{b}$ from the center of the proton. For simplicity of notation we drop the vector symbol in $\vec{b}$ and write b from now on.

If $n_{c\bar{c}}(b) \ll 1$, $n_{c\bar{c}}(b)$ is the probability of producing a $c\bar{c}$ pair in a pp collision at impact parameter b. If $n_{c\bar{c}}(b) \geq 1$, $n_{c\bar{c}}(b)$ is just the mean value of k, the number of $c\bar{c}$ pairs produced, at impact parameter b. Let the probability of k scatterings $ij \to c\bar{c}$ in a pp collision at impact parameter b be $P_{kc\bar{c}}(b)$. Then

$$n_{c\bar{c}}(b) = \sum_{k=0}^{\infty} k P_{kc\bar{c}}(b). \qquad (4.6)$$

The inclusive cross section for charm production is obtained by integrating the probability of having at least one $ij \to c\bar{c}$ scattering, which is $1 - P_{0c\bar{c}}(b)$, over the impact parameter b. Thus

$$\sigma_{c\bar{c}\text{incl}} = \int d^2b \left[1 - P_{0c\bar{c}}(b)\right]. \qquad (4.7)$$

The k-tuple parton cross section is obtained instead by integrating the probability of exactly k parton scatterings $P_{kc\bar{c}}(b)$ over the impact parameter b,

$$\sigma_{kc\bar{c}} = \int d^2b\ P_{kc\bar{c}}(b). \qquad (4.8)$$

Of course, $\sigma_{c\bar{c}\text{incl}} = \sum_k \sigma_{kc\bar{c}}$ for $k \neq 0$.

The total pp cross section can be obtained in analogy to Eq. (4.7) as

$$\sigma_{\rm tot} = \int d^2b\,[1 - P_0(b)]\,, \tag{4.9}$$

where $P_0(b)$ is the probability of not having any parton-parton interaction at impact parameter b, into any final state. Since there are final states other than $c\bar{c}$, one has $P_{0c\bar{c}}(b) > P_0(b)$. It follows that $1 - P_{0c\bar{c}}(b) < 1 - P_0(b)$ and so $\sigma_{c\bar{c}\rm incl} < \sigma_{\rm tot}$. This is what one would expect.

On the other hand, in our evaluation of charm production by cosmic ray interactions in the atmosphere, we must count the number of $c\bar{c}$ pairs produced in the pp collision. So we define $\sigma_{c\bar{c}}$ including the number k of $c\bar{c}$ pairs produced per collision (the multiplicity). We find

$$\sigma_{c\bar{c}} = \sum_k k\sigma_{kc\bar{c}} = \int d^2b \sum_k k P_{kc\bar{c}}(b) = \int d^2b\; n_{c\bar{c}}(b). \tag{4.10}$$

This cross section can be larger than the inclusive charm cross section and even the total pp cross section, because it accounts for multiparton interactions. In particular, the ratio $\sigma_{c\bar{c}}/\sigma_{c\bar{c}\rm incl}$ gives the average charm multiplicity.

Notice that here we consider only independent production of $c\bar{c}$ pairs in 2→2, 4→ 4, etc. processes, and we neglect coherent production of multiple $c\bar{c}$ pairs in 2→4, 2→6, etc. processes. This will underestimate the charm production cross section.

We assume in the following that the partonic distributions $f_i(x, \mu_F^2, b)$ factorize as

$$f_i(x, \mu_F^2, b) = f_i(x, \mu_F^2)\rho_i(b), \tag{4.11}$$

where $f_i(x, \mu_F^2)$ is the usual parton distribution function, and $\rho_i(b)$ is the probability

density of finding a parton in the area d^2b at impact parameter b. We normalize $\rho_i(b)$ to $\int d^2b\ \rho_i(b) = 1$, to maintain the usual normalization $\int dx\ x f_i(x) = 1$. The factorization in Eq. (4.11) is consistent with the usual parton picture and with our assumption of no parton-parton correlations.

The mean number of $ij \to c\bar{c}$ scatterings at impact parameter b then becomes

$$n_{c\bar{c}}(b) = \sum_{ij} a_{ij}(b)\sigma_{QCD}(ij \to c\bar{c}), \tag{4.12}$$

where

$$a_{ij}(b) = \int d^2b' \rho_i(b')\rho_j(b + b') \tag{4.13}$$

is an overlap integral, and $\sigma_{QCD}(ij \to c\bar{c})$ is the QCD parton-parton cross section for $ij \to c\bar{c}$, as in Eq. (4.4). From the normalization of $\rho_i(b)$ it follows that $\int d^2b\ a_{ij}(b) = 1$ for every i, j. Hence from Eqs. (4.10) and (4.12) we find

$$\sigma_{c\bar{c}} = \sigma_{QCD}, \tag{4.14}$$

where $\sigma_{QCD} = \sum_{ij} \sigma_{QCD}(ij \to c\bar{c})$ is the charm production cross section calculated within QCD. This justifies our use of σ_{QCD} as $\sigma_{c\bar{c}}$ in the calculation of the atmospheric fluxes.

The way in which we use $\sigma_{c\bar{c}}$ in our simulation is as follows. We input only one $c\bar{c}$ pair per pp collision at a given energy E, and multiply by $\sigma_{c\bar{c}}$, which includes the $c\bar{c}$ multiplicity. We make, therefore, the following approximation in the kinematics of the $c\bar{c}$ pairs produced in the same pp interaction. Even if in a real multiparton collision the energy available to the second and other $c\bar{c}$ pairs is smaller than E, we are neglecting this difference. This is a very good approximation because the fraction of center of mass energy that goes into a $c\bar{c}$ pair is of the order of $\sqrt{\hat{s}/s} \sim$

$\sqrt{10\ \mathrm{GeV}/E} \ll 1$ at the high energies we are concerned with.

4.4 Uncertainties due to cascade simulation, parameters of charm production model and choice of PDF's

In Part One we considered the uncertainties related to the cascade generation in PYTHIA. There we tried different modes of cascade generation, different options allowed by PYTHIA in the various stages of parton showering, hadronization, interactions and decays, etc., without noticing substantial changes in the final results (differing at most by 10 %). These uncertainties are however very difficult to quantify, due to the nature of the PYTHIA routines. Since these uncertainties are small, we neglect them in this analysis and continue to use PYTHIA with the options described in Part One as our main choice for the simulation: 'single' mode with showering, 'independent' fragmentation, interactions and semileptonic decays according to TIG (see Chapter Two for details).

Important sources of uncertainty are contained in our charm production model, which is NLO pQCD as implemented in the MNR program [19], calibrated at low energies.

The calibration procedure consisted in the following:

- choosing a PDF set from those available and fixing the related value of Λ_{QCD};[1]
- choosing m_c, μ_F and μ_R, which are the charm mass, the factorization scale and the renormalization scale respectively, so as to fit simultaneously both the total and

[1]We note that Λ_{QCD} can be chosen in the MNR program independently of the PDF and therefore can constitute an additional independent parameter of our model. We have opted however to choose the value of Λ_{QCD} assumed in the PDF set being used, for consistency.

differential cross sections from existing fixed target charm production experiments [11, 12] at the energy of 250 GeV, without additional normalization factors;

• checking that the total cross section generated after the previous choices fits reasonably well the other existing experimental points for fixed target charm production experiments [14].

Besides the choice of the PDF set, our procedure has the freedom to choose reasonable values of the three parameters m_c, μ_F, and μ_R so as to fit the experimental data. In Part One and Two we made the standard choice [19, 14] of

$$\mu_F = 2m_T, \quad \mu_R = m_T, \tag{4.15}$$

where $m_T = \sqrt{p_T^2 + m_c^2}$ is the transverse mass. The values of the charm mass are taken slightly different for each PDF set, namely:

$$m_c = 1.185 \text{ GeV} \quad \text{for MRS R1}, \tag{4.16}$$

$$m_c = 1.310 \text{ GeV} \quad \text{for MRS R2}, \tag{4.17}$$

$$m_c = 1.270 \text{ GeV} \quad \text{for CTEQ 4M}, \tag{4.18}$$

$$m_c = 1.250 \text{ GeV} \quad \text{for MRST}. \tag{4.19}$$

Here we explore the changes induced in cross sections and fluxes at high energies by different choices of m_c, μ_F, and μ_R which fulfil our calibration requirements.

We have performed this analysis with the most recent PDF set: the MRST [31] (other PDF's give similar results). At first we fix $\lambda = 0$ and then we examine other values of λ. We note that the calibration procedure described above is independent of λ because it involves only relatively low energies, where the low x extrapolation is not an issue.

4.4.1 MRST $\lambda = 0$: fluxes

We considered the $\lambda = 0$ case because it is the most significant for the evaluation of the uncertainties in the spectral indices, as it will be clear in the next subsection. We have considered the following reasonable ranges of the parameters

$$1.1 \text{ GeV} \leq m_c \leq 1.4 \text{ GeV}, \tag{4.20}$$

$$0.5\ m_T \leq \mu_F \leq 2\ m_T, \tag{4.21}$$

$$0.5\ m_T \leq \mu_R \leq 2\ m_T, \tag{4.22}$$

where the bounds on m_c come from the 1998 Review of Particle Physics [37], while those for μ_F and μ_R are those used in the existing literature [19, 14].

Within these ranges we have looked for values of the three parameters capable of reproducing the experimental data in our calibration procedure described before. Table 4.1 summarizes the different sets of parameters: we have varied the charm mass through the values m_c = 1.1, 1.2, 1.25, 1.3, 1.4 GeV (m_c = 1.25 GeV was our previous optimal choice for MRST in Eq. (4.19)) and then found values of the factorization and renormalization scales that reproduce the experimental value of the total cross section $\sigma_{c\bar{c}} = 13.5 \pm 2.2$ μb at 250 GeV [11]. In particular, for each value of m_c, we took $\mu_F = m_T/2$, m_T, $2m_T$ and found the value of μ_R which best fits the data.

We have also checked that these choices give good fits to the differential, besides the total, cross sections at 250 GeV [12], without additional normalization factors, as done for the original choice of parameters in Part One. For m_c = 1.1 GeV we had to choose values of μ_R slightly outside the range in Eq. (4.22) (but we have kept these values in our analysis anyway).

For all the sets of parameters in Table 4.1 we have run our full simulations for the MRST, $\lambda = 0$ case and the results are described in Figs. 4.2-4.5.

In Figs. 4.2 and 4.3 we show the resulting total charm production cross section $\sigma_{c\bar{c}}$ for all of the fifteen sets of parameters in Table 4.1, together with recent experimental data (from Table 1 of Ref. [14], where all the data for pp or pN collisions have been transformed into a $\sigma_{c\bar{c}}$ cross section following the procedure described in Part One). Fig. 4.3 is an enlargement of the region of Fig. 4.2 containing the experimental data.

In Fig. 4.2 we see the spread of the cross sections, which is more than one order of magnitude at 10^{11} GeV. One can clearly distinguish three "bands" of increasing cross sections for $\mu_F = m_T/2$, m_T and $2m_T$. Within each "band" the cross sections increase with increasing values of m_c, or with decreasing values of μ_R. Our standard choice ($m_c = 1.25$ GeV, $\mu_F = 2m_T$, $\mu_R = m_T$) proves to be one of the highest cross sections we obtain.

In Fig. 4.3 we see better how all of these cross sections verify our calibration procedure. They pass through the point at 250 GeV [11], agree with the point at 400 GeV [38] and disagree with the very low experimental point at 200 GeV [39]. The lower values of $\mu_F = m_T/2$ and m_T fit better the lowest experimental point at 800 GeV [40], while the higher value of $\mu_F = 2m_T$ fits better the upper point at 800 GeV [41].

We believe that the spread of the total cross sections shown in Fig. 4.2 provides a reasonable estimate of the uncertainty of our charm production model at fixed λ. Since our standard choice of parameters ($m_c = 1.25$ GeV, $\mu_F = 2m_T$, $\mu_R = m_T$) gives one of the highest cross sections (in better agreement with the more recent value of the cross section at 800 GeV [41]), the uncertainty band should be added under each of the cross section curves calculated with our standard choice of

parameters (like the curves shown in Fig. 3.1).

Fig. 4.4 illustrates the corresponding spread of the final prompt fluxes. Although our results are for the MRST PDF's extrapolated with $\lambda = 0$ (the value of λ which gives the lowest fluxes) similar spreads result from other PDF's and λ's. We show the flux of muons; the fluxes of muon-neutrinos and electron-neutrinos are essentially the same.

Similarly to what happens with cross sections in Fig. 4.2, the fluxes in Fig. 4.4 increase with the value of μ_F and, keeping this fixed, they increase with m_c. At energies around 10^6 GeV the total uncertainty is almost one order of magnitude and decreases slightly for higher energies. If we would decide to work only with $\mu_F = 2m_T$ (which fits the experimental measurement at 800 GeV with the highest cross section), the uncertainty would be greatly reduced: the fluxes in this rather narrow band differ by less than 40%. We observe that the flux calculated with our standard choice of parameters ($m_c = 1.25$ GeV, $\mu_F = 2m_T$, $\mu_R = m_T$) is almost the highest, as was the case for the corresponding cross section in Fig. 4.2.

In Fig. 4.4 we also indicate the conventional and prompt fluxes from TIG; we notice that the TIG prompt flux is within our band of uncertainty, which is reasonable since TIG used a low $\lambda = 0.08$ value for their predictions (see the discussions in Part One and Two).

4.4.2 MRST $\lambda = 0$: spectral index

In the previous chapter, we pointed out that an experimental measurement of the slope of the atmospheric lepton fluxes at energies where the prompt component dominates over the conventional one, might give information on the value of λ, the slope of the gluon PDF at small x. The best flux for this measurement is that of

down-going muons, because the prompt neutrinos have first to convert into muons or electrons through a charged current interaction in order to be detectable in a neutrino telescope.

In this section and in the following two we consider the uncertainties in our method to determine λ. In this section we examine those coming from the charm production model, in Sect. 4.5 those related to the non linearity of our model, and in Sect. 4.6 those coming from the unknown composition of the cosmic rays at high energies.

The slope of the fluxes or spectral index is $\alpha_\ell(E_\ell) = -\partial \ln \phi_\ell(E_\ell)/\partial \ln E_\ell$, with $\ell = \mu^\pm, \nu_\mu + \bar{\nu}_\mu$ or $\nu_e + \bar{\nu}_e$. In other words, the final lepton fluxes are

$$\phi_\ell(E_\ell) \propto E_\ell^{-\alpha_\ell(E_\ell)}. \tag{4.23}$$

In Part Two we found a simple linear dependence of α_ℓ on λ, namely

$$\alpha_\ell(E_\ell) = b_\ell(E_\ell, \gamma, \lambda) - \lambda \simeq b_\ell(E_\ell) - \lambda, \tag{4.24}$$

where $b_\ell(E_\ell)$ is an energy dependent coefficient evaluated using our simulation with $\lambda = 0$ and fixed γ. As argued in Part Two (cfr. Eqs. (3.35) and (3.36)), the coefficient $b_\ell(E_\ell, \gamma, \lambda)$ depends mildly on λ and can be well approximated by its value for $\lambda = 0$ (see Sect. 4.5). The coefficient $b_\ell(E_\ell, \gamma, \lambda)$ depends almost linearly on γ, the spectral index of the primary cosmic rays. We recall that the equivalent nucleon flux for primary cosmic rays is expressed as

$$\phi_N(E) \propto E^{-\gamma-1}. \tag{4.25}$$

The linear dependence of $b_\ell(E_\ell, \gamma, \lambda)$ on γ can be written as

$$b_\ell(E_\ell, \gamma, \lambda) = \bar{b}_\ell(E_\ell, \gamma, \lambda) + \gamma, \tag{4.26}$$

where $\bar{b}_\ell(E_\ell, \gamma, \lambda)$ depends mildly on λ and γ [2], as we will prove in Sect. 4.5 and Sect. 4.6, respectively.

Given $b_\ell(E_\ell)$ from our model, an experimental measurement of α_ℓ at energy E_ℓ would immediately give λ corresponding to a value of $x \simeq \mathrm{GeV}/E_\ell$, as we discussed in Part Two. A measurement at $E_\ell \simeq 10^6$ GeV $= 1$ PeV would give λ at $x \simeq 10^{-6}$, a value of x unattainable by present experiments.

For the time being we keep fixed the value of γ ($\gamma = 1.7$ below the knee, and $\gamma = 2.0$ above the knee, as in the previous chapters); only in Sect. 4.6 we will consider changes in the value of γ.

The feasibility of a measurement of λ depends, therefore, on the uncertainties in $b_\ell(E_\ell)$. Here we discuss those coming from the charm production model.

Fig. 4.5 shows the $-b_\mu$ corresponding to the fluxes of Fig. 4.4 as functions of E_μ. In the region of interest $E_\mu \gtrsim 10^5$–10^6 GeV, the values of $-b_\mu$ within each "band" of fixed μ_F decrease with increasing m_c.

The spread of b_μ due to the choice of μ_F , μ_R and m_c is $\Delta b_\mu \simeq 0.1$, or $\Delta b_\mu / b_\mu \simeq 0.03$, much smaller than the uncertainty $\Delta\phi_\mu/\phi_\mu \simeq 10$ of the absolute flux in Fig. 4.4. If we would for some reason restrict ourselves to the $\mu_F = 2\, m_T$ band, the uncertainty on b_μ would become even smaller, $\Delta b_\mu \simeq 0.03$. We will refer to this error as Δb_{par} in the following, as it is related to the choice of parameters in the charm production model. Therefore

[2] We have included in $\bar{b}_\ell$ the $+1$ term coming from the -1 in the exponent of Eq. (4.25).

$$\Delta b_{par} \simeq 0.1\ (0.03), \tag{4.27}$$

where the value in parenthesis corresponds to the $\mu_F = 2m_T$ band.

4.4.3 MRST $\lambda = \lambda(T)$

So far we used $\lambda = 0$ only. This case determines the uncertainty of the $b_\ell(E_\ell)$ function which enters in the determination of λ through the atmospheric muon fluxes.

Here we study an "intermediate" value of λ. We continue to use the MRST PDF, but with the value of $\lambda = \lambda(T)$ given by the slope of the lowest tabulated value of x (see Part Two for more explanations). This value depends on Q^2 and is about 0.2-0.3.

We repeat the same analysis of subsection 4.4.1. However, for simplicity, we report the results for four selected sets of values for the parameters in Table 4.1. The first set ($m_c = 1.1$ GeV, $\mu_F = 0.5\ m_T$, $\mu_R = 2.53\ m_T$) gives a lower bound for the fluxes. The second set ($m_c = 1.4$ GeV, $\mu_F = 2m_T$, $\mu_R = 0.61\ m_T$) gives an upper bound for the fluxes. The remaining two sets are cases in the $\mu_F = 2m_T$ "band".

The results are plotted in Fig. 4.6. The general features of Fig. 4.6 coincide with those of Fig. 4.4, except for an overall increase in all the fluxes due to the larger value of λ. The total spread of the fluxes given by the two limiting cases, as well as the spread within the narrower $\mu_F = 2m_T$ band, are comparable to those found for $\lambda = 0$. As in Fig. 4.4, our standard choice of parameters ($m_c = 1.25$ GeV, $\mu_F = 2m_T$, $\mu_R = 1.0\ m_T$) yields almost the highest flux.

We conclude that similar features would be obtained for other values of λ: our

"standard choice" flux would be almost the highest in a band of uncertainty whose width is similar for all values of λ. The fluxes in the uncertainty band of Fig. 4.6 are consistent with older predictions and with the prediction by L. Pasquali et al. [21].

4.4.4 Other PDF's

Another source of uncertainty for the final fluxes and spectral indices is the choice of the PDF set. As in Part Two, we consider here four recent sets of PDF's: MRS R1-R2 [22], CTEQ 4M [24] and MRST [31], with the standard choice of parameters of Eqs. (4.15),(4.16),(4.17),(4.18),(4.19).

Figs. 4.7 and 4.8 show the muon fluxes (top panels) and spectral indices (bottom panels) for the two limiting cases of $\lambda = 0$ (Fig. 4.7) and $\lambda = 0.5$ (Fig. 4.8). In both cases the μ fluxes show at most a $30 - 50\%$ variation depending on the PDF used. The uncertainty in the spectral indices for $E_\mu \gtrsim 10^5 - 10^6$ GeV is $\Delta b_\mu \lesssim 0.02$, or $\Delta b_\mu / b_\mu \lesssim 0.01$. This error will be denoted as Δb_{PDF} in the following, namely

$$\Delta b_{PDF} \simeq 0.02. \tag{4.28}$$

These uncertainties, related to the PDF's, are smaller that those due to the choices of mass scales (see Figs. 4.4, 4.5). We conclude that, provided different PDF's are calibrated in a similar way (i.e. same values of μ_F, μ_R and m_c, chosen to fit the experimental data of our calibration), the final fluxes and spectral indices are very similar. The main source of uncertainty resides therefore in the choice of the mass parameters, rather than the adoption of a certain PDF set.

4.5 Determination of λ with neutrino telescopes

In Part Two we have given a detailed analysis of the dependence of the final fluxes and spectral indices on λ for different PDF's. In this section we show that the spread in our results due to λ is larger than the one due to the choice of μ_F, μ_R, m_c and of the PDF set, analyzed in the previous section. This is good news for the possibility of measuring λ, since the spread in α_μ, due to different λ's, is the signal we want to detect, while the spread due to other factors constitutes the theoretical error of this measurement.

Figs. 4.9-4.12 show how the μ flux and its spectral index depend on λ. We used MRST with variable $\lambda = 0,\ 0.1,\ 0.2,\ 0.3,\ 0.4,\ 0.5$ and our standard choice of parameters ($m_c = 1.25$ GeV, $\mu_F = 2m_T$, $\mu_R = 1.0\ m_T$).

Fig. 4.9 contains the differential muon fluxes. At the highest energies the μ fluxes are spread over almost two orders of magnitude. To each of the curves in this plot we need to assign a band of uncertainty of about one order of magnitude coming from the choice of the PDF and of the parameters m_c, μ_F, and μ_R (see Fig. 4.4). Thus the curves become entirely superposed with each other. This makes it impossible to derive the value of λ from an experimental measurement of the absolute level of the fluxes. However, the uncertainties in the spectral index of these prompt muons are much smaller and a determination of λ becomes possible using the slope of the muon fluxes instead of their absolute level.

Fig. 4.10 shows the E^2-weighted integrated fluxes as functions of the muon energy. The slant lines indicate the number of particles traversing a km^3 detector over a 2π sr solid angle. Even for the highest predicted fluxes, less than 1 particle per year will traverse the km^3 detector for energies above 10^8 GeV. Moreover, while prompt muons can be detected directly, prompt neutrinos have first to convert

into charged leptons before being detected. The smallness of the charged current interaction effecting the conversion considerably lowers the detection rate of neutrinos. Therefore, the slope of the charm component of the atmospheric leptons can be studied in neutrino telescopes only using atmospheric muons coming from above the horizon, and only in a narrow range of energies, between a lower limit of $E_\mu \simeq 10^5 - 10^6$ GeV, above which the prompt component dominates over the conventional one, and an upper limit of $E_\mu \simeq 10^7 - 10^8$ GeV, above which the detection rates become negligible.

In practice, the spectral index of the prompt muon flux may be estimated by the difference of two integrated muon fluxes above two different energies, e.g. 10^6 and 10^7 GeV.

Figs. 4.11, 4.12 prove the validity in our model of Eq. (4.24), which is $\alpha_\ell(E_\ell) = b_\ell(E_\ell) - \lambda$. In Fig. 4.11 we plot the spectral indices $-\alpha_\ell(E_\ell)$ for the different values of λ, both as directly calculated with our simulation (solid lines) and as $-b_\ell(E_\ell) + \lambda$ (dotted lines), where $b_\ell(E_\ell)$ is α_ℓ with $\lambda = 0$. The two almost coincide, in the interval of interest, $E_\ell \gtrsim 10^6$ GeV. Their difference, $\alpha_\ell(E_\ell) - b_\ell(E_\ell) + \lambda$, given in Fig. 4.12, is small, about $\simeq 0.03$ at $E \gtrsim 10^6$ GeV. This difference stems from the mild dependence of $b_\ell(E_\ell)$ on λ and need to be added to the the other uncertainties evaluated in Sect. 4.4. We will refer to this error, due to the non linearity in λ of Eq. (4.24), as

$$\Delta b_{non-lin} \simeq 0.03. \tag{4.29}$$

We see in Fig. 4.11 that $\Delta\lambda \sim \Delta\alpha$, therefore we would need an uncertainty in the spectral index of order 0.1 to determine λ with the same accuracy. We will show now that this is roughly the uncertainty related to our theoretical model.

In fact, we can finally estimate the total uncertainty in the determination of λ coming from our theoretical model (that is, excluding the uncertainty due to the unknown composition of cosmic rays). We sum together the three spreads of $b_\ell(E_\ell)$ previously calculated in Eqs. (4.27), (4.28) and (4.29), to obtain the final uncertainty [3] from the charm production model,

$$(\Delta\lambda)_{charm} \simeq (\Delta b_\mu)_{charm} \simeq 0.15\ (0.08), \tag{4.30}$$

where the number in parenthesis corresponds to fixing $\mu_F = 2m_T$ in the charm model.

If the theoretical uncertainties so far presented would be the only ones affecting the determination of λ through a measurement of the slope of the down-going muon flux, we could expect to get to know λ with an uncertainty of about $\Delta\lambda \sim 0.1$. However, even excluding experimental uncertainties in the neutrino telescopes themselves, the uncertainty increases when our ignorance of the composition of the cosmic rays at high energy is taken into account, as we show in the following section.

4.6 Uncertainty from cosmic ray composition

The final uncertainty we consider in the determination of λ comes from the poorly known elemental composition of the high energy cosmic rays.

The spectral index of the cosmic rays γ enters almost linearly in the slope of the atmospheric leptons. From Eqs. (4.24) and (4.26) we have

$$\alpha_\ell(E_\ell) = \bar{b}_\ell(E_\ell, \gamma, \lambda) + \gamma - \lambda. \tag{4.31}$$

[3] We summed the errors linearly. Summing in quadrature would give $(\Delta\lambda)_{charm} \simeq (\Delta b_\mu)_{charm} \simeq 0.11\ (0.05)$.

So far we have kept γ fixed, thus the uncertainty Δb_μ calculated in Eq. (4.30) is actually an uncertainty in $\bar{b}_\mu$. We are going now to evaluate the uncertainty due to γ.

The non–linearity of Eq. (4.31) with respect to γ is mild, as we have argued analytically in Part Two and we show here using our numerical simulation. We have conducted a few trial runs of our simulation simply changing the values of γ used for the primary flux. We recall from subsection 4.4.2 that in our model we used $\gamma = 1.7,\ 2.0$, respectively below and above the knee at $E = 5\ 10^6\ GeV$. We have run our simulation changing these values of γ by $\pm 0.1,\ \pm 0.2$ [4], both above and below the knee, to see the error produced when taking $\bar{b}_\ell$ computed at fixed γ (our usual values) in Eq. (4.31) and thus leaving a pure linear dependence on γ. We used the MRST PDF, with $\lambda = 0$, but similar results are obtained with other PDF's and λ's.

In Fig. 4.13 we plot the spectral index $-\alpha_\ell(E_\ell)$ for the different values of γ, both as directly calculated with our simulation (solid lines) and as $-\bar{b}_\ell(E_\ell; \gamma = 1.7,\ 2.0; \lambda = 0) - \gamma$ (dotted lines), i.e. using our standard values for γ of the primary flux and adding an increment in γ equal to $\pm 0.1,\ \pm 0.2$. In this way the "central value" of these spectral indices corresponds to the $\lambda = 0$ case of Fig. 4.11. We can see that the dotted and the solid lines almost coincide, especially in the interval of interest for $E_\ell \gtrsim 10^5 - 10^6$ GeV, proving the validity of Eq. (4.31). The uncertainty in $\bar{b}_\ell$ due to this non-linearity, that we call $\Delta\gamma_{non-lin}$, evaluated in terms of the difference $\alpha_\ell - \bar{b}_\ell - \gamma$, is plotted in Fig. 4.14 and, in the energy range of interest, is

[4] Notice that these values of γ are some of the most probable values (see Fig. 4.16).

$$\Delta\gamma_{non-lin} \simeq 0.02. \tag{4.32}$$

We will now consider the error due to the poorly known elemental composition of the high energy cosmic rays. Concerning charm production, the relevant cosmic ray flux to be considered is the equivalent flux of nucleons impinging on the atmosphere. For a given cosmic ray flux, the equivalent flux of nucleons $\phi_{eq}(E_N)$ depends in general on the composition of the cosmic rays. Nuclei with atomic number A and energy E_A, coming with a flux $\phi_A(E_A)$, contribute an amount $A\phi_A(AE_N)$ to the equivalent flux of nucleons at energy $E_N = E_A/A$. So in total

$$\phi_{eq}(E_N) = \sum_A A\phi_A(AE_N). \tag{4.33}$$

The uncertainties in the equivalent nucleon flux arise from the poorly known composition of cosmic rays in the energy range above the so-called knee, $E_A \sim 10^6$ GeV.

The actual γ that enters into our proposed determination of λ is the spectral index of the equivalent nucleon flux γ_{eq}, the equivalent cosmic rays spectral index for short. The equivalent nucleon flux is written as $\phi_{eq} \propto E_N^{-\gamma_{eq}-1}$, so that the spectral index γ_{eq} is given by

$$\gamma_{eq} + 1 = -\frac{E_N}{\phi_{eq}}\frac{\partial\phi_{eq}}{\partial E_N} = \frac{1}{\phi_{eq}}\sum_A A\phi_A(\gamma_A + 1), \tag{4.34}$$

where γ_A is the spectral index of the component of atomic number A, i.e. $\phi_A(E_A) = k_A E_A^{-\gamma_A-1}$.

We have calculated ϕ_{eq} and γ_{eq} using the experimental data of JACEE [42], CASA-MIA [43], HEGRA [44], and the data collected by Biermann et al, in Table

1 of Ref. [45], each with their respective compositions. Figs. 4.15 and 4.16 show the ϕ_{eq} and the γ_{eq} so obtained. Only the data of CASA-MIA [43] and HEGRA [44] reach energies $E_N \lesssim 10^8$ GeV, so we have not extended our analysis beyond 10^8 GeV.

We have calculated the error band associated to γ_{eq} in two different ways, because of the different parametrization of the composition used in Refs. [42] to [45]. Refs. [42, 45] give separate power law fits to the spectrum of each cosmic ray component,

$$\phi_A(E_A) = k_A E_A^{-\gamma_A - 1}, \tag{4.35}$$

where the parameters k_A and γ_A have errors Δk_A and $\Delta\gamma_A$. Standard propagation of errors gives, in this case,

$$\Delta\phi_{eq} = \left\{ \sum_A A^2 \phi_A^2 \left[\left(\frac{\Delta k_A}{k_A} \right)^2 + \left(\ln(AE_N) \Delta\gamma_A \right)^2 \right] \right\}^{1/2} \tag{4.36}$$

and

$$\Delta\gamma_{eq} = \left\{ \sum_A \frac{A^2\phi_A^2}{\phi_{eq}^2} \left[(\gamma_A - \gamma_{eq})^2 \left(\frac{\Delta k_A}{k_A} \right)^2 + \left[1 - (\gamma_A - \gamma_{eq}) \ln(AE_N) \right]^2 \left(\Delta\gamma_A \right)^2 \right] \right\}^{1/2}, \tag{4.37}$$

where ϕ_A is evaluated at $E_A = AE_N$.

Refs. [43, 44], give a power law fit to the total particle flux

$$\phi(E_A) = kE_A^{-\gamma - 1} \tag{4.38}$$

and a composition ratio $r_A(E_A)$ in terms of which

$$\phi_A(E_A) = r_A(E_A)\, \phi(E_A). \tag{4.39}$$

These experiments distinguish only between a light and a heavy component. We assign atomic number 1 to the light component and 56 to the heavy one (which we call "iron"). Here k, γ, and r_A have errors Δk, $\Delta\gamma$, and Δr_A, respectively. The equivalent nucleon flux is still given by Eq. (4.33), while standard propagation of errors gives in this case

$$\Delta\phi_{eq} = \left\{ \sum_A A^2 \phi_A^2 \left(\frac{\Delta r_A}{r_A} \right)^2 + \phi_{eq}^2 \left(\frac{\Delta k}{k} \right)^2 + \left[\sum_A A \phi_A \ln(AE_N) \Delta\gamma_A \right]^2 \right\}^{1/2}, \quad (4.40)$$

We omit the much longer expression for $\Delta\gamma_{eq}$. For simplicity, we have neglected the error coming from the energy dependence of r_A, which we expect to be much smaller than the others. In Fig. 4.15 we show the equivalent nucleon flux ϕ_{eq}. It is clear from the figure that the systematic uncertainties dominate, with spreads between different experiments of up to a factor of 4.

The uncertainties in the equivalent spectral index γ_{eq} are smaller, as can be seen in Fig. 4.16, where only HEGRA and CASA-MIA extend to the energy region above the knee which is important to us.

We can consider, for example, an energy $E_N \simeq 10^7\ GeV$, which is likely to determine the leptonic fluxes at around $E_\ell \simeq 10^6\ GeV$, energy at which we would like to measure λ through the spectral index (we recall from Part Two that $E_\ell \lesssim 0.1\ E_N$).

At this energy E_N, from Fig. 4.16, we may take half the difference between the central values of the CASA-MIA and HEGRA data as an indication of the systematic uncertainty on γ_{eq},

$$\Delta\gamma_{syst} \simeq 0.1. \quad (4.41)$$

Using the CASA-MIA data and the related error band, instead of the very spread

HEGRA data, we can expect a reasonable statistical uncertainty

$$\Delta\gamma_{stat} \simeq 0.05. \tag{4.42}$$

Since α_ℓ depends linearly on γ_{eq} and λ, the same uncertainties apply to a determination of λ. The total uncertainty in the determination of λ coming from the unknown composition of cosmic rays is now simply the sum of Eqs. (4.32), (4.41) and (4.42),

$$(\Delta\lambda)_{comp} \simeq (\Delta\gamma_{eq})_{comp} \simeq 0.17, \tag{4.43}$$

if summing the errors linearly, or

$$(\Delta\lambda)_{comp} \simeq (\Delta\gamma_{eq})_{comp} \simeq 0.11, \tag{4.44}$$

if we sum them in quadrature.

Finally, we can now combine all the uncertainties together, to compute the overall theoretical error in the determination of λ with neutrino telescopes. From Eqs. (4.27), (4.28), (4.29), (4.32), (4.41), and (4.42) we obtain

$$\Delta\lambda \simeq 0.32 \quad (0.25) \tag{4.45}$$

if summing errors linearly, or

$$\Delta\lambda \simeq 0.16 \quad (0.12), \tag{4.46}$$

if summing in quadrature, where the numbers in parenthesis correspond to the $\mu_F = 2m_T$ "band" in the charm model.

4.7 Conclusions for Part Three

We have examined in detail the possibility of determining the slope λ of the gluon PDF, at momentum fraction $x \lesssim 10^{-5}$, not reachable in laboratories, through the measurement in neutrino telescopes of the slope of down-going muon fluxes at $E_\mu \simeq x^{-1}\ GeV$.

To this end we studied the dependence of the leptonic fluxes and their slopes on λ. The slopes depend almost linearly on λ. We studied the uncertainties of the method we propose (excluding the experimental errors of the telescopes themselves). These come mainly from two sources: the free parameters of the NLO QCD calculation of charm production and the poorly known composition of cosmic rays at high energies.

We have seen that, for a fixed value of λ, the uncertainties give rise to an error band for the leptonic fluxes of almost one order of magnitude at the highest energies. This makes impossible a determination of λ based solely on the absolute values of the fluxes, therefore we propose using the slopes of the fluxes. In particular we are proposing to use *down-going muons*, for energies $E_\mu \gtrsim 100\ TeV$, where prompt muons dominate over conventional ones, and not up-going neutrino-induced muons whose flux is orders of magnitude smaller. While an important contribution to up-going muons is expected from astrophysical neutrinos, there is no background for down-going atmospheric muons.

The overall theoretical error, from the charm production model, on the measurement of λ, is $(\Delta\lambda)_{charm} \lesssim 0.10$. A comparable error, due to uncertainties in the cosmic ray composition, $(\Delta\lambda)_{comp} \lesssim 0.15$, must be added, so that the overall error in the determination of λ with neutrino telescopes is $\Delta\lambda \sim 0.2 - 0.3$.

These errors may be reduced by improving the experimental knowledge of the

charm production cross sections and of the cosmic ray composition around and above the knee. We will return on the uncertainties due to cosmic ray composition in the next chapter.

m_c (GeV)	μ_F (m_T)	μ_R (m_T)	$\sigma_{c\bar{c}}^{MNR}$ (μb)	$\sigma_{c\bar{c}}^{EXP}$ (μb)
1.1	0.5	2.53	13.48	13.5 ± 2.2
	1.0	2.40	13.48	"
	2.0	2.10	13.42	"
1.2	0.5	1.46	13.57	13.5 ± 2.2
	1.0	1.40	13.54	"
	2.0	1.23	13.51	"
1.25	0.5	1.18	13.57	13.5 ± 2.2
	1.0	1.13	13.54	"
	2.0	1.00	13.58	"
1.3	0.5	0.96	13.55	13.5 ± 2.2
	1.0	0.92	13.50	"
	2.0	0.83	13.53	"
1.4	0.5	0.68	13.51	13.5 ± 2.2
	1.0	0.66	13.51	"
	2.0	0.61	13.52	"

Table 4.1: Choice of parameters m_c, μ_F and μ_R, that can reproduce the experimental total cross section $\sigma_{c\bar{c}}^{EXP}$ for charm production in pN collisions at 250 GeV from the E769 experiment. For each set of parameters, $\sigma_{c\bar{c}}^{MNR}$ is the cross section calculated with the MNR program using MRST PDF.

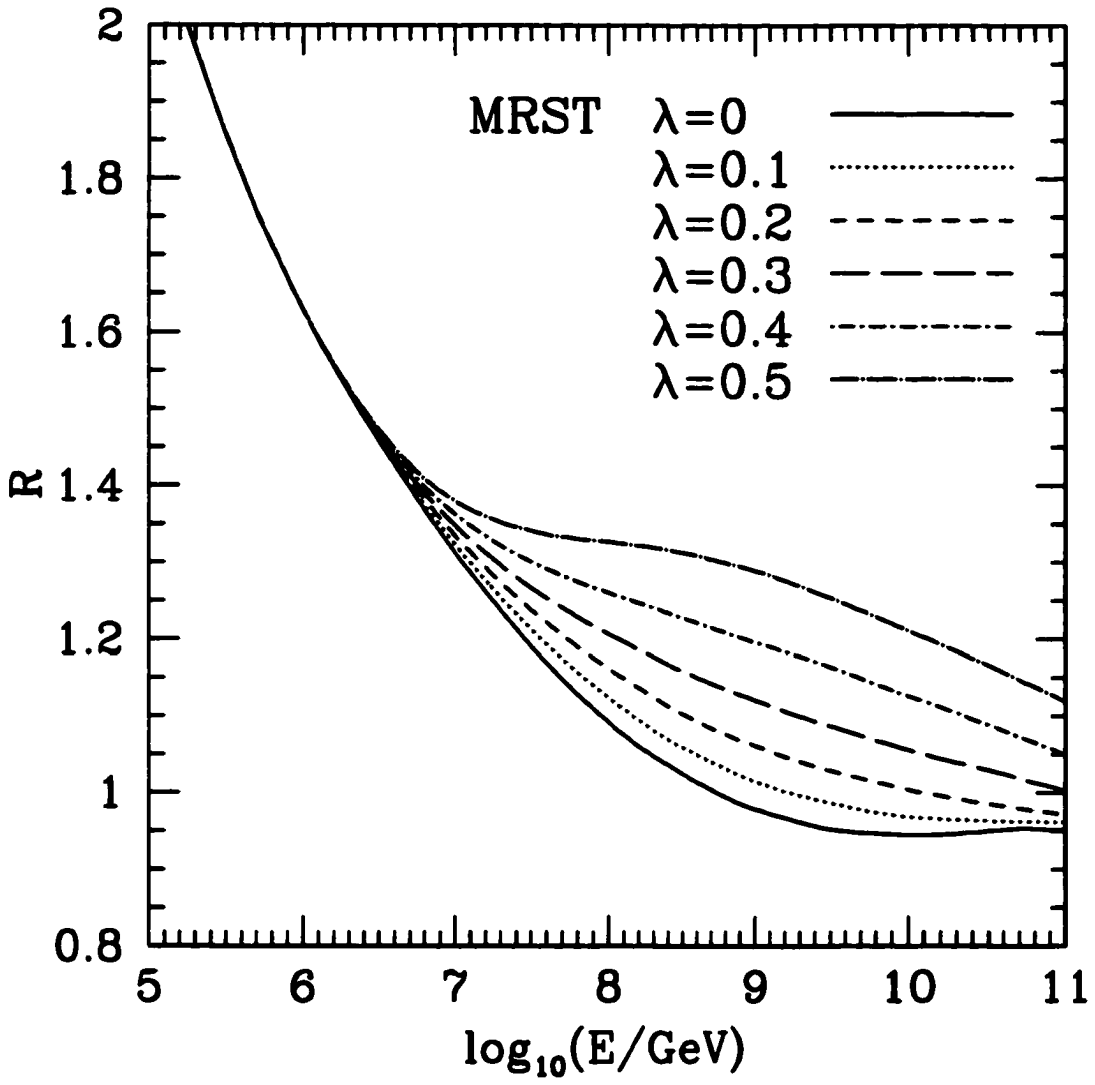

Figure 4.1: The ratio $R = (\sigma_{NLO} - \sigma_{LO})/(\sigma_{LO}\alpha_s \ln(s/m_c^2)/\pi)$ is plotted as a function of the beam energy E, for the different values of λ used with the MRST PDF.

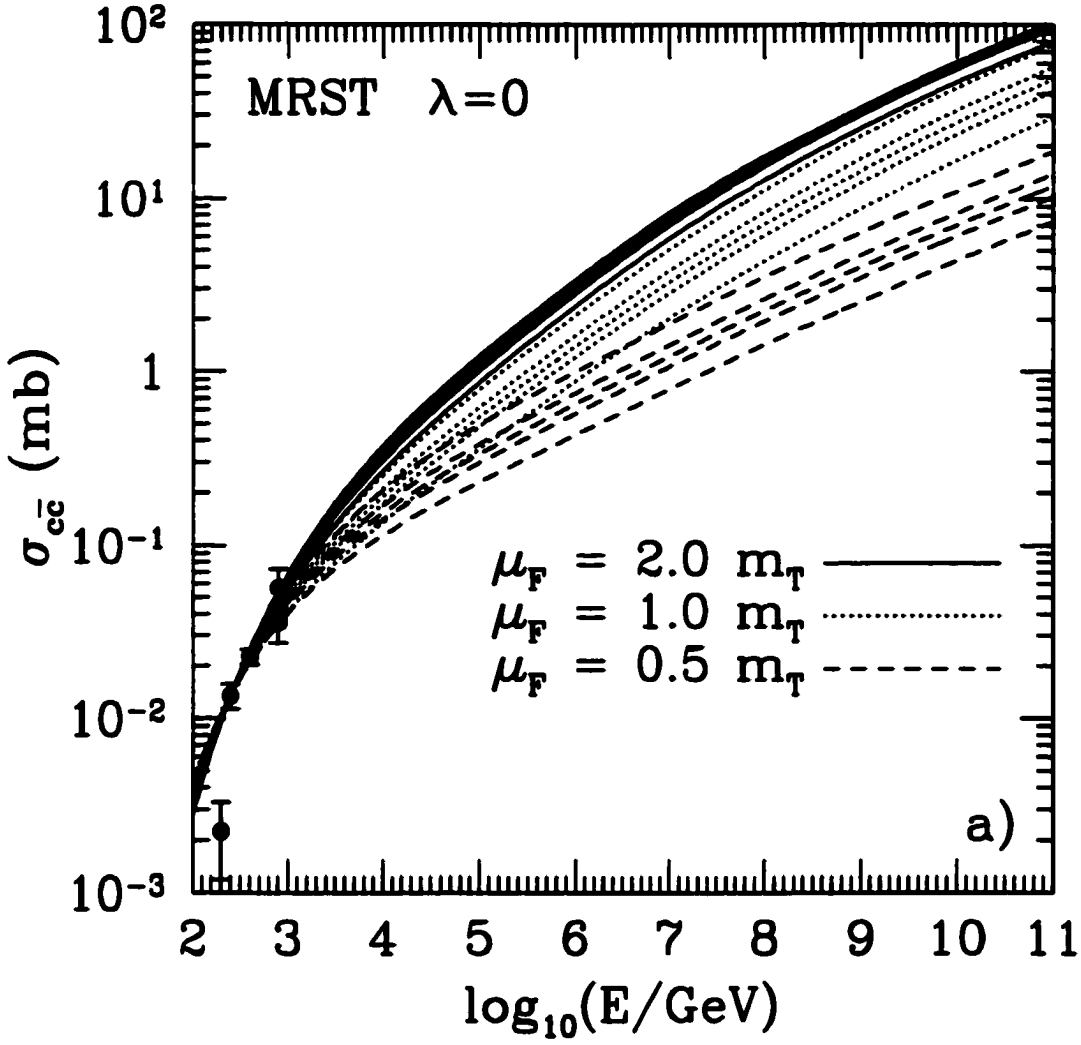

Figure 4.2: Total cross sections for charm production $\sigma_{c\bar{c}}$, up to NLO, calculated with MRST ($\lambda = 0$) and the values of m_c, μ_F, μ_R of Table 4.1, are compared with recent experimental values [11, 14, 38, 39, 40, 41]. For each "band" in the figures (i.e. same value of μ_F) the cross sections increase with increasing m_c (or decreasing μ_R) through the values of Table 4.1.

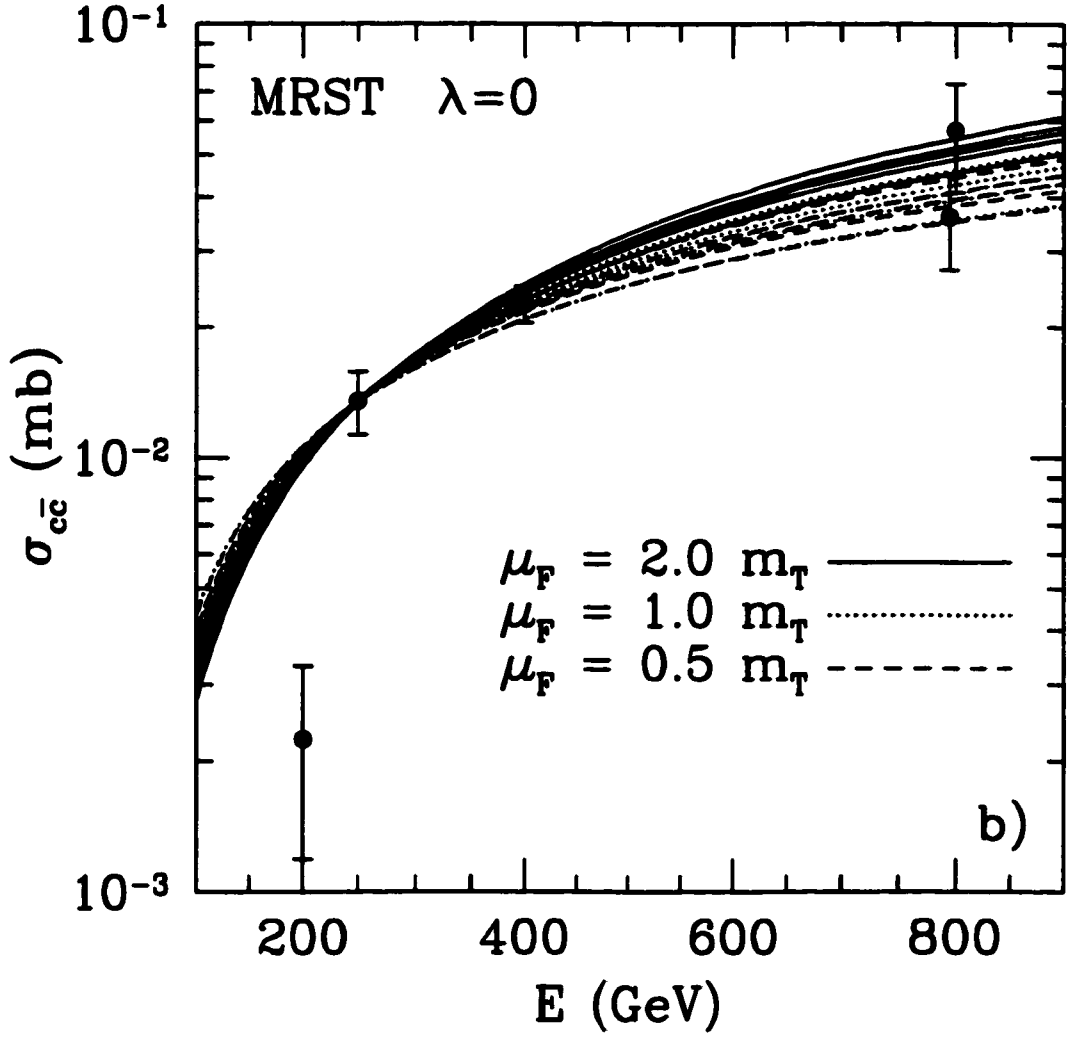

Figure 4.3: Total cross sections for charm production $\sigma_{c\bar{c}}$, up to NLO, calculated with MRST ($\lambda = 0$) and the values of m_c, μ_F, μ_R of Table 4.1, are compared with recent experimental values [11, 14, 38, 39, 40, 41]. For each "band" in the figures (i.e. same value of μ_F) the cross sections increase with increasing m_c (or decreasing μ_R) through the values of Table 4.1 (This is an enlargement of the previous figure).

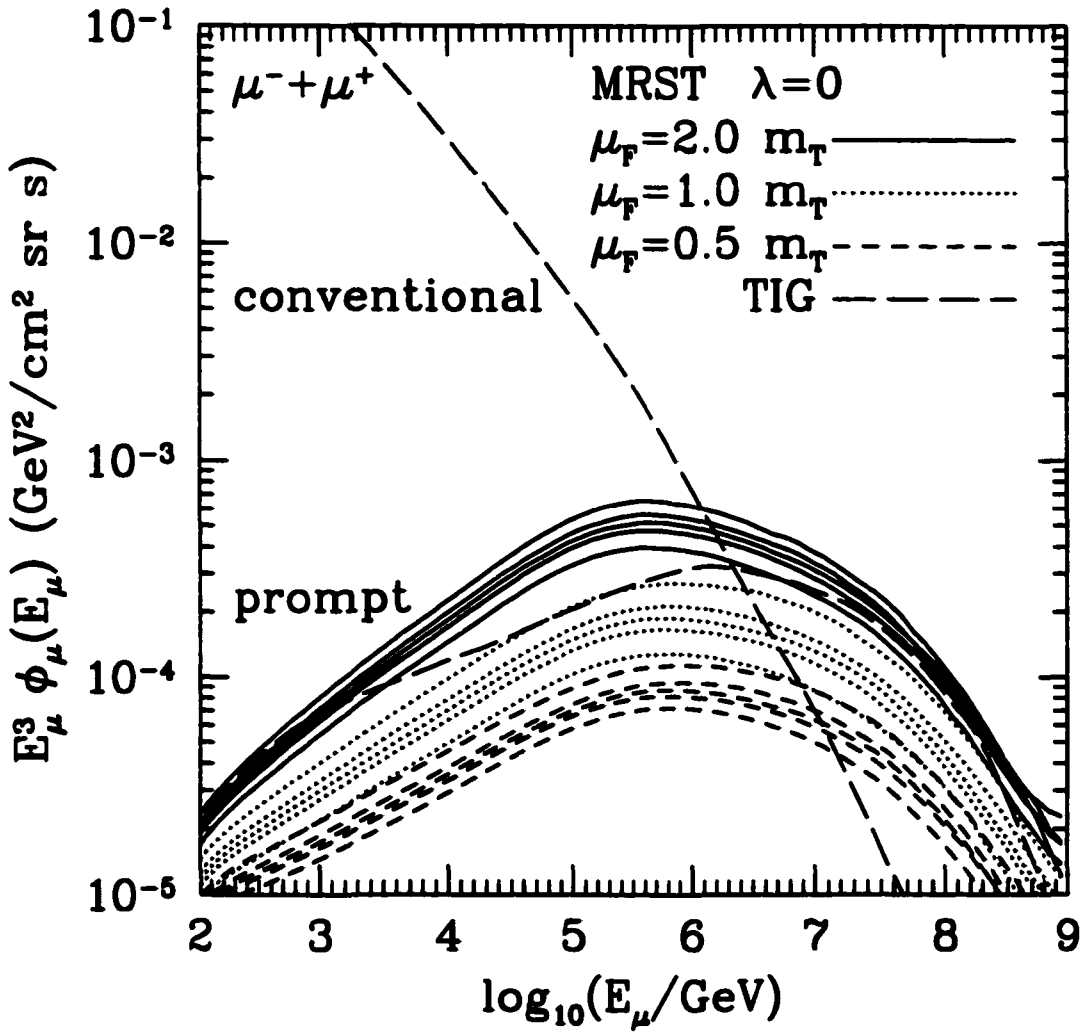

Figure 4.4: Results for MRST $\lambda = 0$. The E_μ^3-weighted vertical prompt fluxes, at NLO, are calculated using the values of m_c, μ_F, μ_R of Table 4.1 and compared to the TIG [15] conventional and prompt fluxes. For each "band" in the figures (i.e. same value of μ_F) the fluxes increase with increasing m_c (or decreasing μ_R) through the values of Table 4.1.

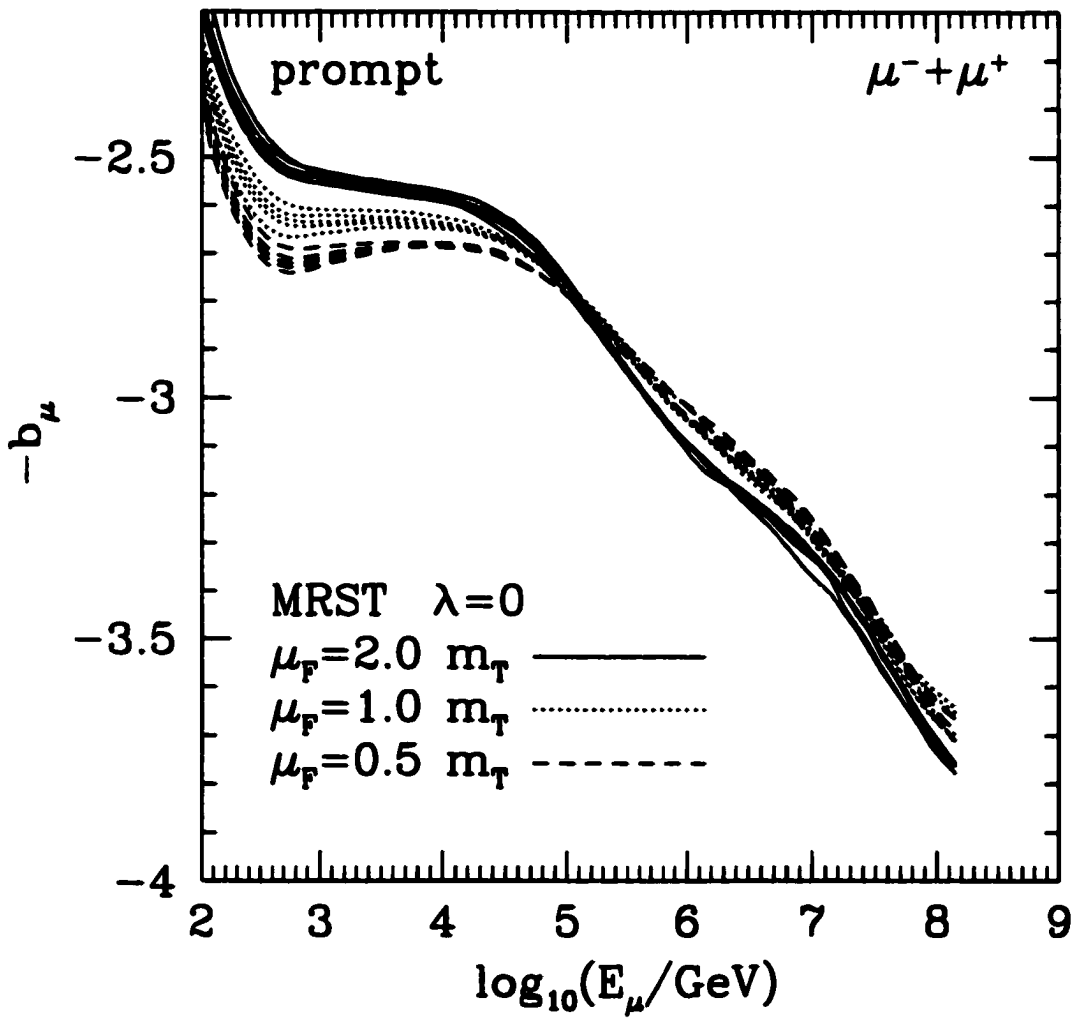

Figure 4.5: Spectral indices $-b_\mu$ of the fluxes plotted in Fig. 4.4, for the MRST $\lambda = 0$ case. For each "band" in the figures (i.e. same value of μ_F) the spectral indices decrease with increasing m_c through the values of Table 4.1.

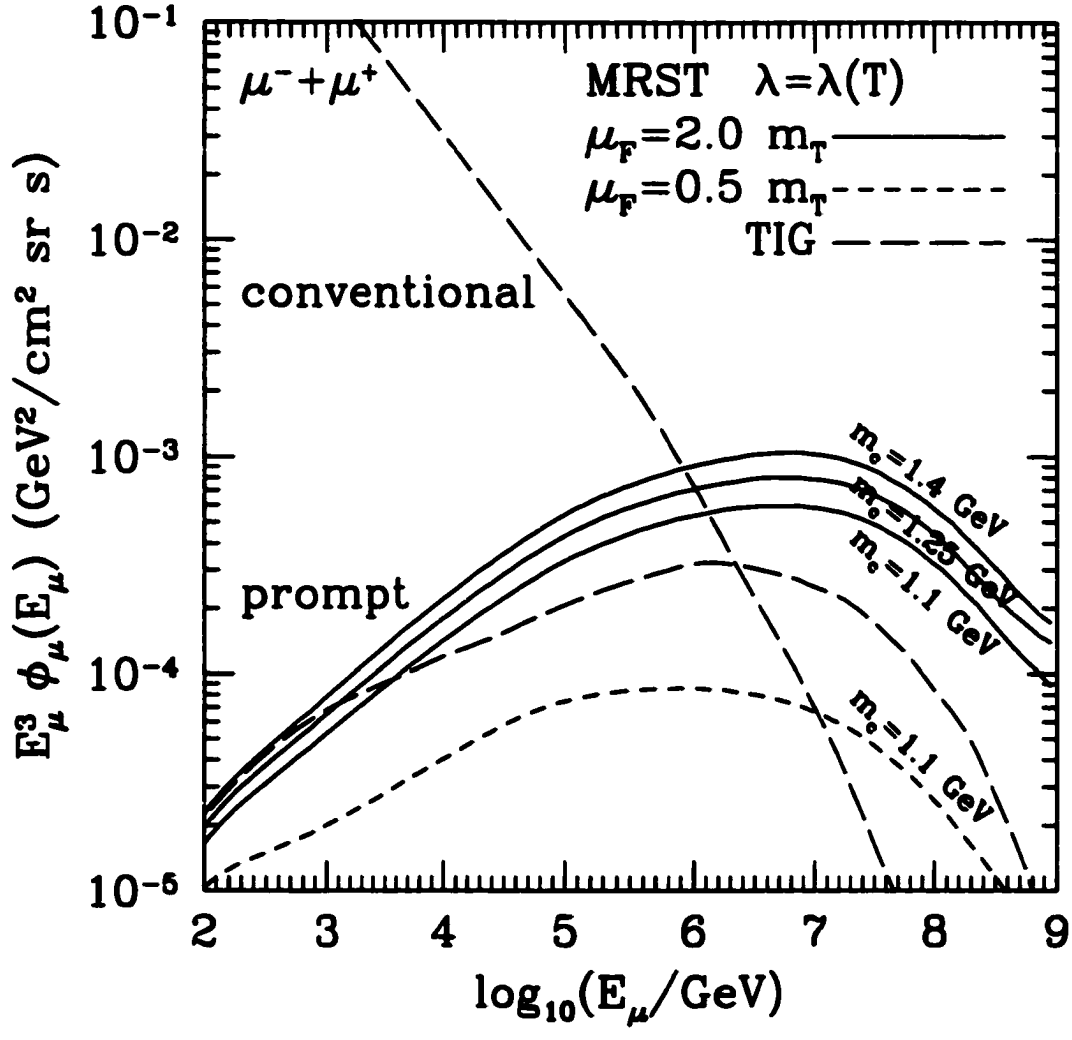

Figure 4.6: Results for MRST $\lambda = \lambda(T)$. The E_μ^3-weighted vertical prompt fluxes, at NLO, are calculated using selected values of m_c, μ_F, μ_R from Table 4.1 and compared to the TIG [15] conventional and prompt fluxes.

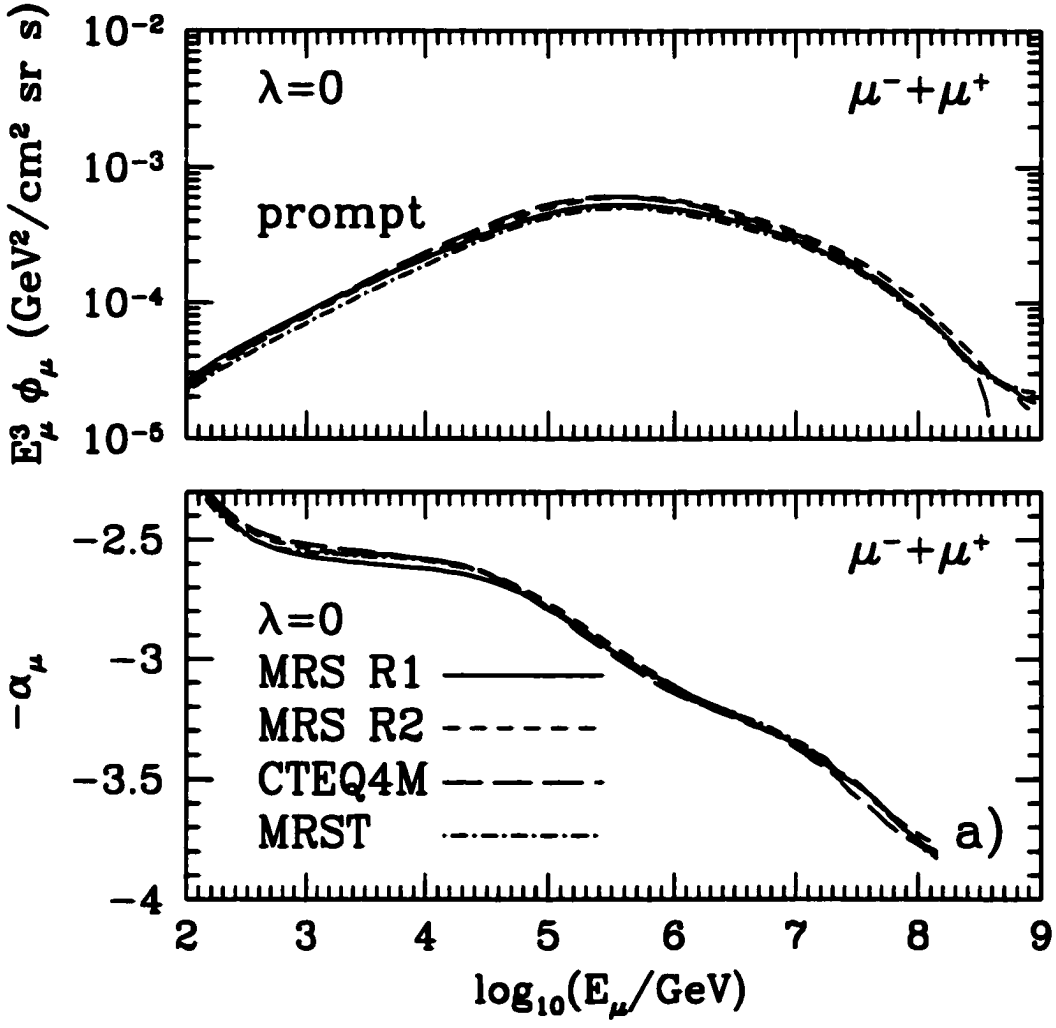

Figure 4.7: Results for MRS R1-R2, CTEQ 4M, MRST, for $\lambda = 0$, with standard choice of parameters m_c, μ_F, μ_R. Top part: E_μ^3-weighted vertical prompt fluxes, at NLO. Bottom part: related spectral indices $-\alpha_\mu$ (for the $\lambda = 0$ case, $-\alpha_\mu = -b_\mu$).

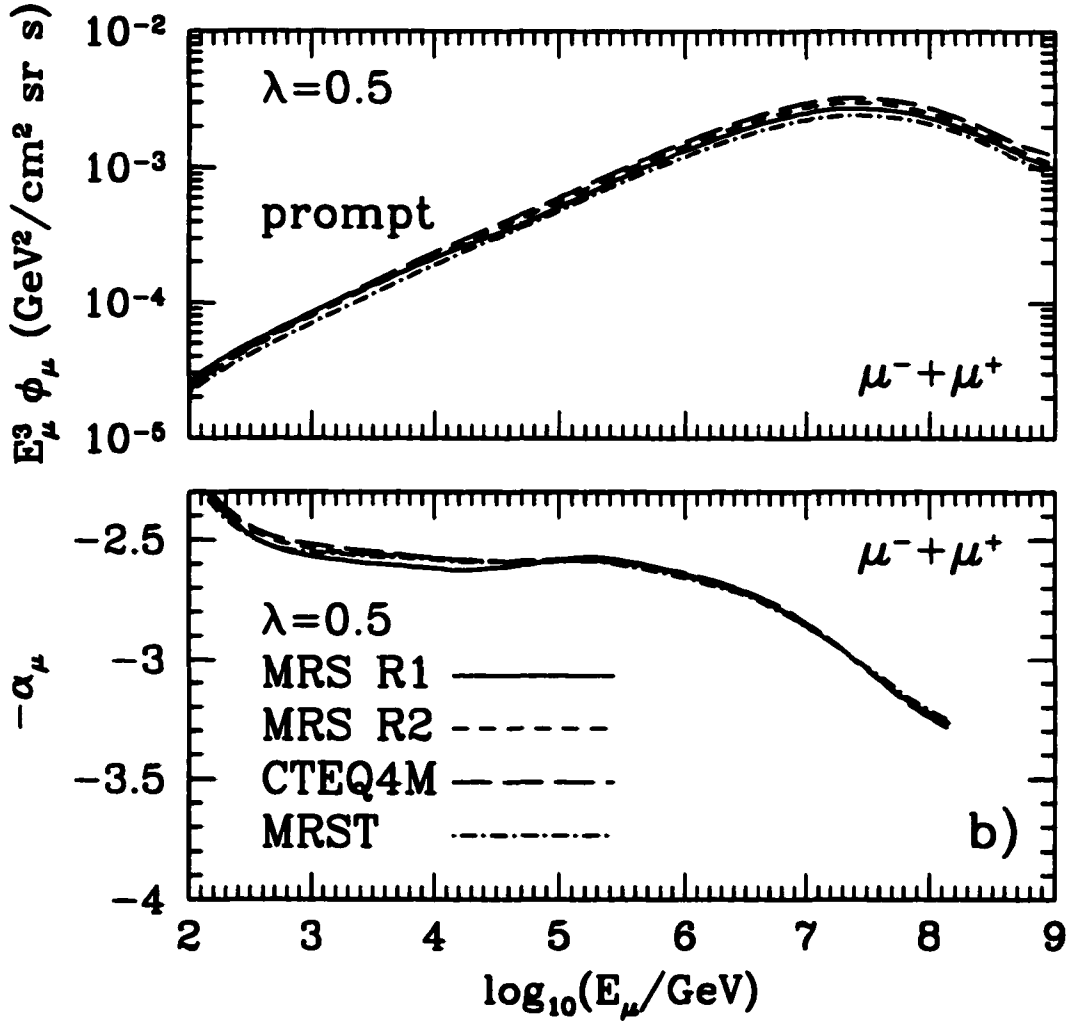

Figure 4.8: Results for MRS R1-R2, CTEQ 4M, MRST, for $\lambda = 0.5$, with standard choice of parameters m_c, μ_F, μ_R. Top part: E_μ^3-weighted vertical prompt fluxes, at NLO. Bottom part: related spectral indices $-\alpha_\mu$.

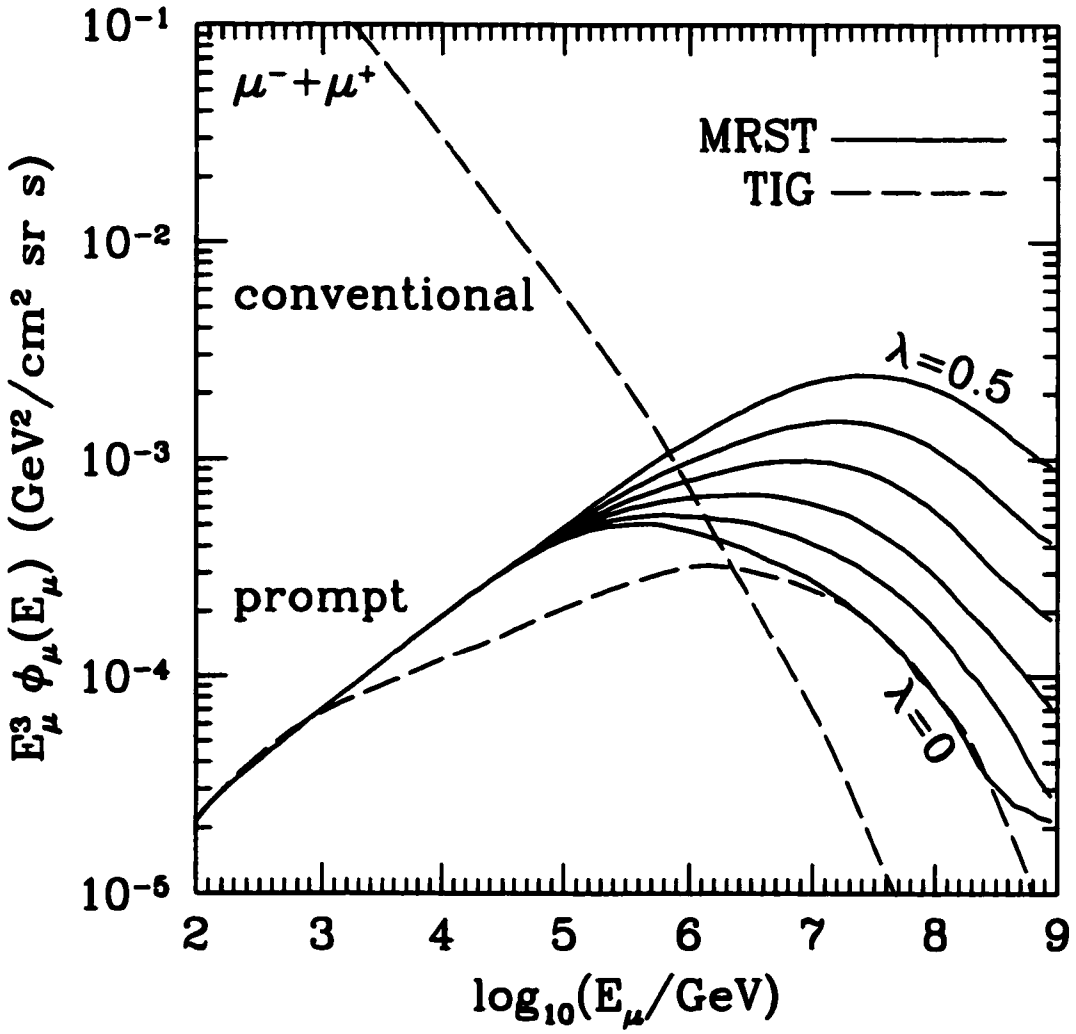

Figure 4.9: Results for MRST $\lambda = 0 - 0.5$ (solid lines). The E_μ^3-weighted vertical prompt fluxes, at NLO, are compared to the TIG [15] conventional and prompt fluxes (dashed lines).

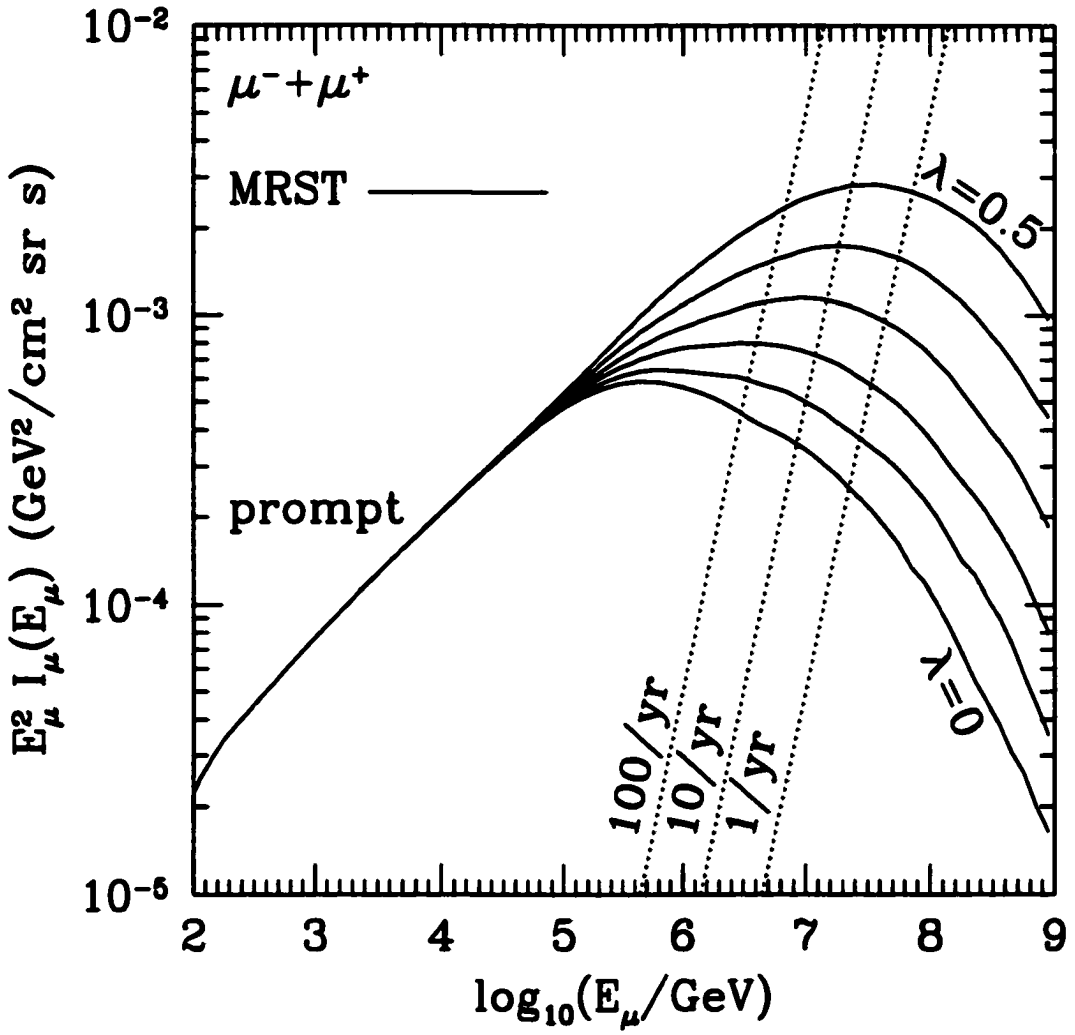

Figure 4.10: Results for MRST $\lambda = 0-0.5$ (solid lines). The E_μ^2-weighted integrated vertical prompt fluxes, at NLO, are compared to the number of particles traversing a km^3 2π sr detector per year (dotted lines).

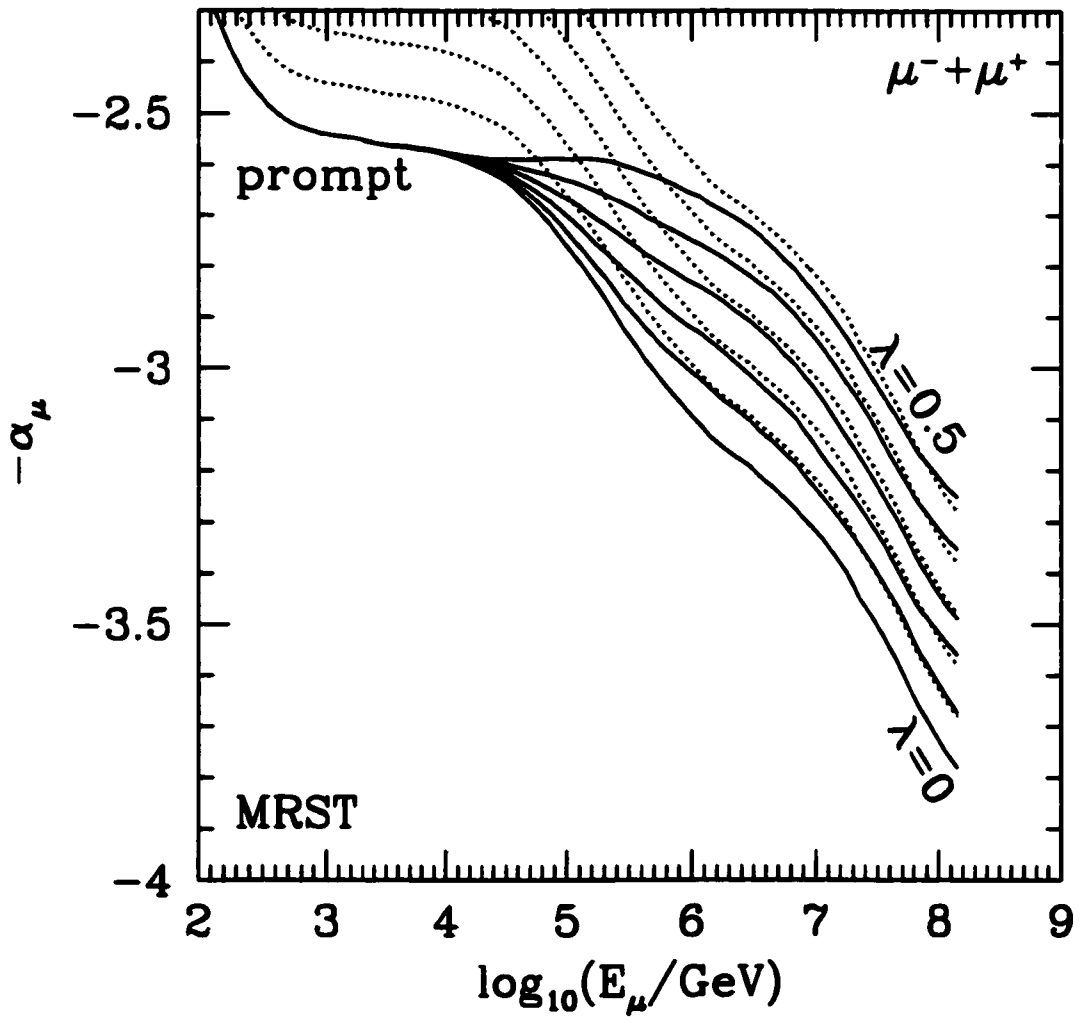

Figure 4.11: Results for MRST $\lambda = 0 - 0.5$. The spectral indices $-\alpha_\ell(E_\ell)$ for the different values of λ, calculated directly by our simulation (solid lines) are compared to the corresponding terms $-b_\ell(E_\ell) + \lambda$ (dotted lines).

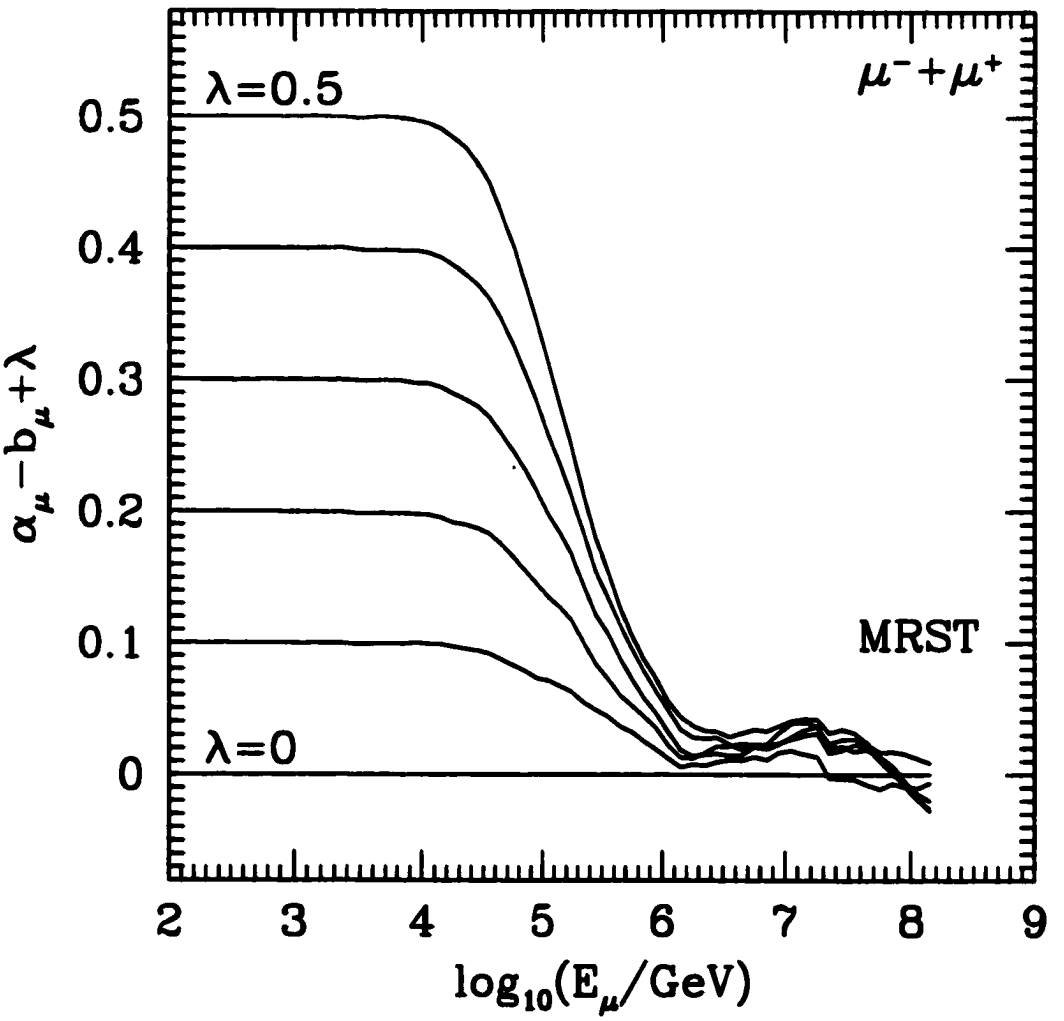

Figure 4.12: Results for MRST $\lambda = 0 - 0.5$ (solid lines). The error of Eq. (4.24) is evaluated in terms of the difference $\alpha_\ell(E_\ell) - b_\ell(E_\ell) + \lambda$.

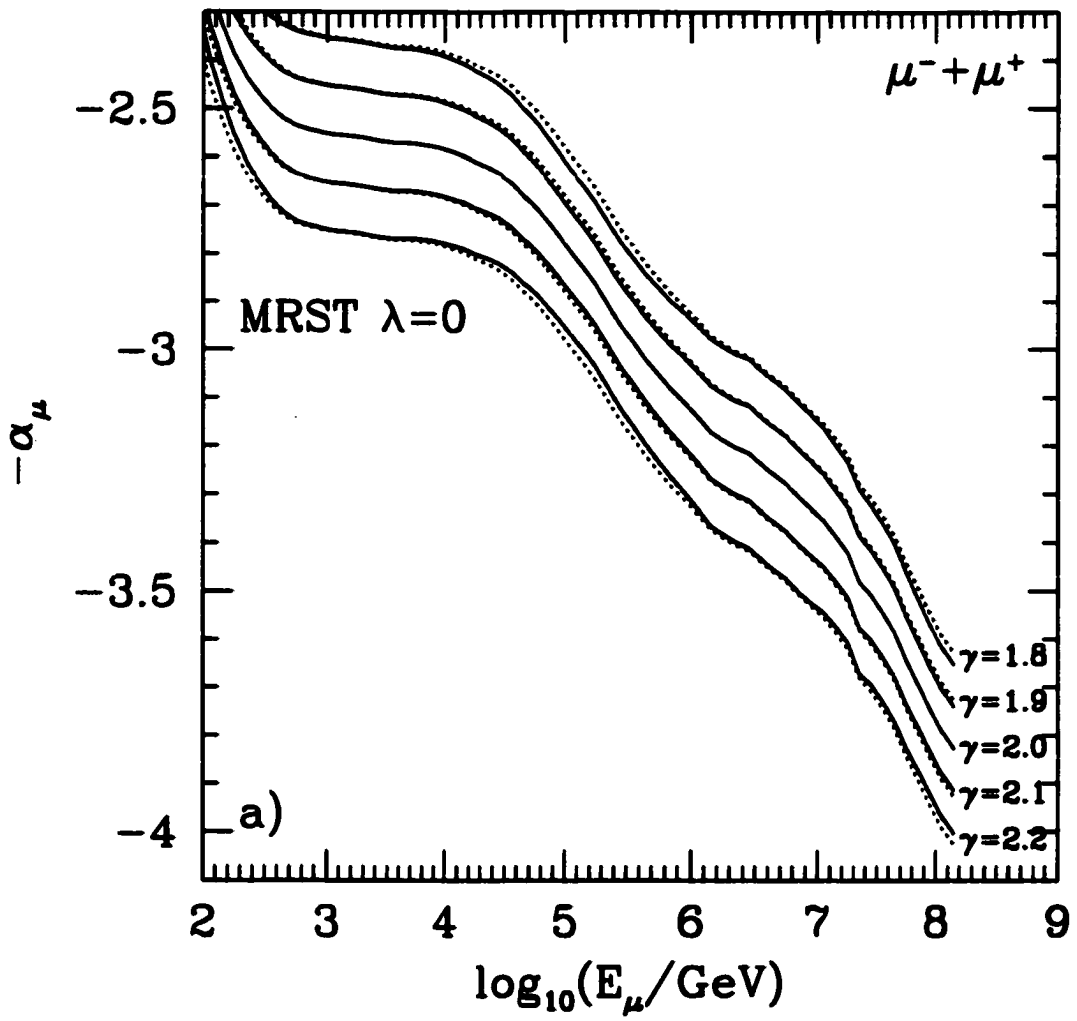

Figure 4.13: Results for MRST $\lambda = 0$ for different values of γ. The spectral indices $-\alpha_\ell(E_\ell)$ for the different values of γ, calculated directly by our simulation (solid lines) are compared to the corresponding terms $-\bar{b}_\ell(E_\ell; \gamma = 1.7,\ 2.0; \lambda = 0) - \gamma$, with increments in γ equal to ± 0.1, ± 0.2 (dotted lines). The curves are labelled by the related value of γ above the knee ($\gamma = 2.0$ is our "standard value").

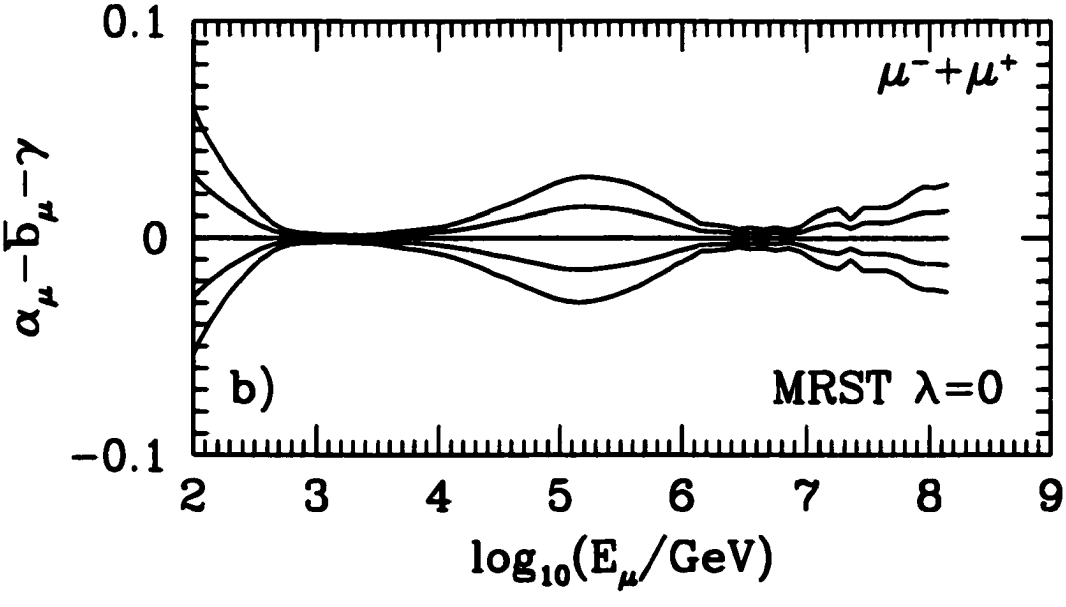

Figure 4.14: Results for MRST $\lambda = 0$ for different values of γ. Uncertainty due to the non-linearity of Eq. (4.31), as the difference $\alpha_\ell - \bar{b}_\ell - \gamma$.

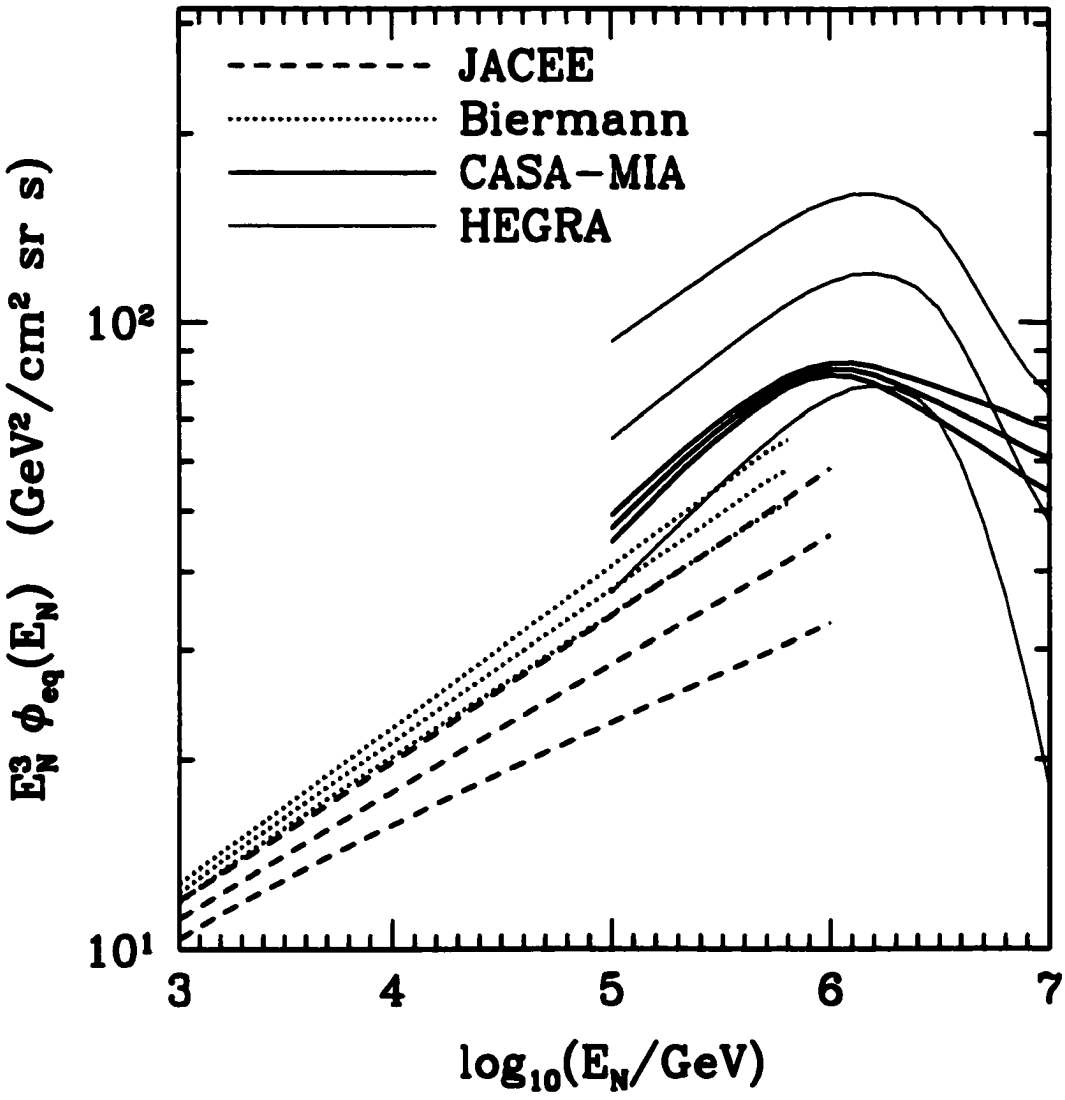

Figure 4.15: The E_N^3-weighted equivalent nucleon flux $\phi_{eq}(E_N)$ is shown for different primary cosmic ray experiments [42, 43, 44, 45]. For each of these we plot the central value and the related error band.

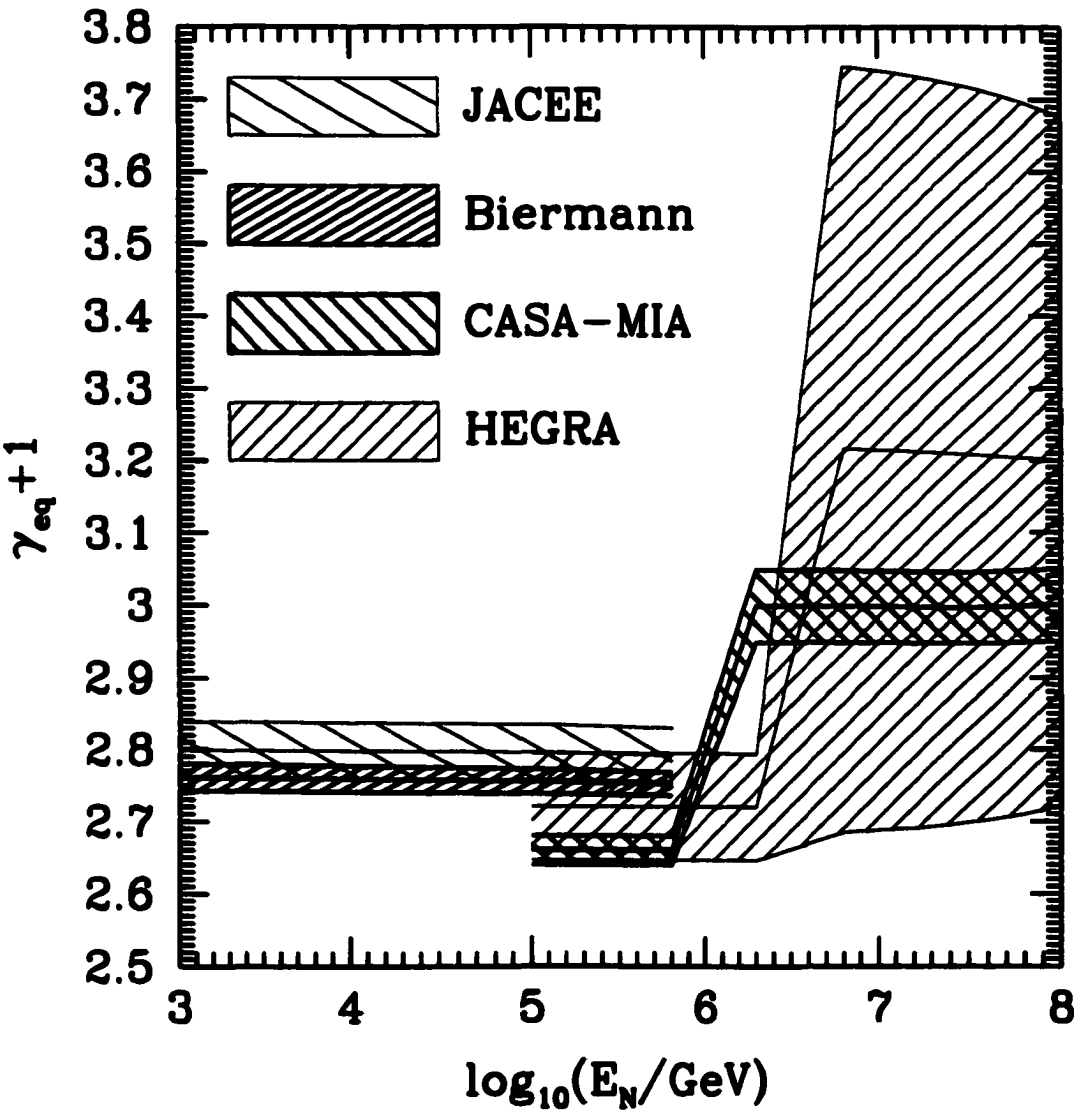

Figure 4.16: The spectral index, $\gamma_{eq}+1$, for the equivalent nucleon fluxes of Fig. 4.15, is shown for different primary cosmic ray experiments [42, 43, 44, 45]. For each of these we plot the central value and the related error band.

Chapter 5

Part Four: Dependence on the Cosmic Ray Model

5.1 Introduction to Part Four

In Part One we have found the NLO pQCD approach to be perfectly adequate to produce fluxes comparable to older predictions (not based on pQCD) and also to the recent pQCD semianalytical analysis of Pasquali, Reno and Sarcevic [21]. We have also explained the reason of the low fluxes in the TIG model [15], the first to use pQCD in this context, which was related to the extrapolation of the gluon partonic distribution function (PDF) at small momentum fractions (small x), confirming however the overall validity of their approach to the problem.

In Part Two we have analyzed in detail the dependance of the fluxes on the extrapolation of the gluon PDF at low x mentioned before, which is related to the choice of the parameter λ. This proved to be a critical factor of the simulation, giving rise to a wide uncertainty of the final fluxes at energies above 10^5 GeV.

We recall that low x extrapolations of the gluon PDF usually propose

$$xg(x) \sim x^{-\lambda}, \tag{5.1}$$

with λ in the range $(0 - 0.5)$, depending on the existing theoretical models.

Because the value of λ is not known from particle physics experiments, we have proposed in Part Two the possibility of its measurement through the atmospheric neutrino fluxes at energies above 10^6 GeV. This would not be possible using the absolute fluxes, because of their large theoretical error, but would rather be done through the spectral index (i.e. the "slope") of the leptonic fluxes, which should be affected by smaller uncertainties.

In Part Three we have investigated further into this possibility, considering the issue of the λ measurement into the more general context of an overall error analysis of our model.

We have analyzed the uncertainty in the charm production model as a major source of error for the prompt atmospheric neutrino fluxes and we have combined this evaluation with the discussion of the λ dependance of the results.

We have seen that, for each value of λ considered, the uncertainties of the model give rise to an error band for the leptonic fluxes, which can span over almost one order of magnitude at the highest energies. This made impossible a determination of λ based solely on the absolute values of the fluxes.

On the contrary, an experimental measure of the spectral index of the fluxes, in an energy range where the "prompt" fluxes would be the dominant ones, could give information on λ and on the gluon distribution function at very low x. In particular we have estimated the overall theoretical error on the measure of λ to be $\Delta\lambda \lesssim 0.10$, which might be further more reduced by improved experimental knowledge of charm

production cross sections.

We have also noted that the predicted fluxes for different λ, together with their bands of uncertainty, are compatible with previous predictions, thus confirming the overall validity of the pQCD approach to the problem.

We have also introduced, in the previous chapter, as a last source of uncertainty in our simulation, the dependence on the primary cosmic ray model. In this chapter we will continue this analysis.

In the next section we will compare the cosmic ray model we used so far, the same one used by the TIG group, with one of the models we have introduced in Part Three. We will then analyze the dependence on these models of the final results of our simulation: differential and integrated leptonic fluxes and related spectral indices. Finally we will discuss how this dependance affects the uncertainty of the estimate of λ with "neutrino telescopes".

5.2 Primary cosmic ray models

In our first three parts we have always used the primary cosmic ray flux from the TIG model [15] to allow a direct comparison of the final prompt fluxes. We recall that TIG neglected the detailed cosmic ray composition and considered all primaries to be nucleons with energy spectrum

$$\phi_N(E)\left[\frac{nucleons}{cm^2\ s\ sr\ GeV\ /\ A}\right] = \phi_0 E^{-\gamma-1} = \tag{5.2}$$

$$= \left\{ \begin{array}{ll} 1.7\ (E/GeV)^{-2.7} & for\ E < 5\ 10^6\ GeV \\ 174\ (E/GeV)^{-3.0} & for\ E > 5\ 10^6\ GeV \end{array} \right\}$$

(see [15] for details and references therein) and the uncertainty of this primary flux was not considered in the TIG model or in our first three parts, except for the brief discussion at the end of the last chapter.

As an example of an alternative model for primary cosmic rays, we will consider in particular here the one recently introduced by B. Wiebel-Sooth, P. L. Biermann and H. Meyer [45] (called WBM in the following). This model provides a detailed and updated analysis of all the experimental data below the knee, i.e. the energy at which the cosmic ray flux steepens (which was taken as $5 \cdot 10^6\ GeV$ in the TIG model), subdividing the fluxes into the contributions of the different elements or classes of elements and including the errors of all these fluxes.

In particular, for energies below the knee, the spectra are given by WBM as

$$\phi_Z \left[\frac{1}{m^2\ s\ sr\ TeV} \right] = \phi_{0_Z}\ (E/TeV)^{-\gamma_Z}, \tag{5.3}$$

where Z refers to the different elements ($Z = 1, ..., 28$) or groups of elements considered together. The values of ϕ_{0_Z} and γ_Z for the different elements can be found in Tables 1-3 of Ref. [45]; in particular we have used in our present analysis the data of Table 1, where the elements and their fluxes are considered individually, i.e. for $Z = 1, 2, ..., 28$. In these tables WBM also quote the errors for the various ϕ_{0_Z} and γ_Z; we will refer to these errors as $\delta\phi_{0_Z}$ and $\delta\gamma_Z$ in the following.

The WBM model considers three sites of origin for the observed cosmic rays:

- supernova explosions into the interstellar medium (ISM-SN),
- supernova explosions into the stellar wind of the predecessor star (wind-SN),
- radio galaxy hot spots for the extragalactic component.

In particular the second type of sources, the wind-SN, is responsible for the bend in the spectrum (i.e. the knee) and basically determines the spectrum beyond

the knee. In this region we have to rely on theoretical predictions, rather than experimental data, therefore we will use those of WBM. For the wind-SN spectrum they propose a knee depending on the particular element, i.e.

$$E_Z^{KNEE} = 600\ Z\ TeV \tag{5.4}$$

and a flux beyond the knee that goes as

$$\phi_{wind}(E) \sim E^{-3.07-0.07\pm0.07}. \tag{5.5}$$

The peculiar way of quoting the error of the spectral index indicates an asymmetric error distribution (see also [46]) extending from the most probable value of 3.07 to 3.21 in our case. For our purposes we will simply rewrite Eq. (5.5) as

$$\phi_{wind}(E) \sim E^{-3.14\pm0.07} = E^{-\gamma_K \pm \delta\gamma_K}, \tag{5.6}$$

thus considering a "central" value for the spectral index beyond the knee $\gamma_K = 3.14$ with an error $\delta\gamma_K = 0.07$.

To obtain a working model for cosmic rays we will combine together Eqs. (5.3), (5.4) and (5.6) to obtain an equivalent nucleon flux ϕ_N. Below the knee we use Eq. (5.3) with the data of Table 1 in Ref. [45] and we add together the various contributions rewriting the total flux as an equivalent nucleon flux, i.e. number of nucleons per unit of time, area, solid angle and energy E (energy per nucleon, in GeV/A)[1].

[1]We use the same symbol, E, for the energy per nucleon, like in Eq. (5.3), or for the energy per nucleus (i.e. for each actual component of the primary cosmic rays) like in Eq. (5.3). It should be clear from the context which type of energy is being considered.

After performing also a change of units, the equivalent nucleon flux below the knee[2] becomes

$$\phi_N(E)\left[\frac{nucleons}{cm^2\ s\ sr\ GeV/A}\right] = 10^{-7}\sum_{Z=1}^{28} A(Z)\ \phi_{0_Z}\left[\frac{A(Z)\ E}{10^3\ GeV}\right]^{-\gamma_Z} = \\ = \sum_{Z=1}^{28} A(Z)^{(1-\gamma_Z)}\ 10^{(3\gamma_Z-7)}\ \phi_{0_Z}\left(\frac{E}{GeV}\right)^{-\gamma_Z}, \qquad (5.7)$$

where $A(Z)$ is the mass number (we used $A(1) = 1$, $A(2) = 4$, $A(3) = 6.5$, $A(4) = 9$, $A(5) = 10.5$, $A(Z) = 2Z$ for $Z \geq 6$) and again the values of $\delta\phi_{0_Z}$ and $\delta\gamma_Z$ come from Table 1 of Ref. [45].

To evaluate the flux ϕ_N beyond the knee(s) we have considered each component, for $Z = 1, 2, ...28$, using Eq. (5.3) up to each respective knee given by Eq. (5.4) and, beyond that energy, we have continued the flux simply "bending" it to assume the steeper spectral index of Eq. (5.6). Therefore, beyond each respective knee, we have assumed that all the components have the same slope, given by the WBM model, through Eqs. (5.5) and (5.6).

We can formally write the equivalent nucleon flux ϕ_N as

$$\phi_N(E)\left[\frac{nucleons}{cm^2\ s\ sr\ GeV/A}\right] = 10^{-7}\sum_{Z=1}^{28} A(Z)\ \phi_{0_Z}\left[\frac{A(Z)\ E}{10^3\ GeV}\right]^{-\gamma_Z} + \\ +10^{-7}\sum_{Z'=1}^{28} A(Z')\ \phi_{0_{Z'}}\left[\frac{A(Z')\ E_{Z'}^{KNEE}}{10^3\ GeV}\right]^{-\gamma_{Z'}}\left[\frac{E}{E_{Z'}^{KNEE}}\right]^{-\gamma_K}, \qquad (5.8)$$

where the first sum runs only on those elements Z such that $E < E_Z^{KNEE} =$

[2]There is actually one "knee" for each component according to Eq. (5.4), the following equation applies only for energies below all "knees", i.e. $E < (E_Z^{KNEE})_{\min} = 600\ TeV$.

6 Z 10^5 GeV, i.e. for E less than the variable knee(s), while the second sum is for E greater than the variable knee(s), for those elements Z' such that $E > E_{Z'}^{KNEE} =$ 6 Z' 10^5 GeV. We have also considered the error on the equivalent nucleon flux coming from all the errors $\delta\phi_{0_Z}$, $\delta\gamma_Z$ and $\delta\gamma_K$ quoted in the WBM model. Using standard error propagation on Eq. (5.8) we obtain the overall error $\delta\phi_N$ as follows:

$$\delta\phi_N(E)\left[\frac{nucleons}{cm^2\ s\ sr\ GeV/A}\right] = \tag{5.9}$$

$$= 10^{-7}\left\{\begin{array}{c} \sum_{Z=1}^{28} A^2(Z)\ \left[\frac{A(Z)\ E}{10^3\ GeV}\right]^{-2\gamma_Z}\left[\delta\phi_{0_Z}^2 + \phi_{0_Z}^2 \ln^2\left(\frac{A(Z)\ E}{10^3\ GeV}\right)\delta\gamma_Z^2\right] \\ + \sum_{Z'=1}^{28} A^2(Z')\left[\frac{A(Z')\ E_{Z'}^{KNEE}}{10^3\ GeV}\right]^{-2\gamma_{Z'}}\left[\frac{E}{E_{Z'}^{KNEE}}\right]^{-2\gamma_K} \cdot \\ \left[\delta\phi_{0_{Z'}}^2 + \phi_{0_{Z'}}^2 \ln^2\left(\frac{A(Z')\ E_{Z'}^{KNEE}}{10^3\ GeV}\right)\delta\gamma_{Z'}^2 + \phi_{0_{Z'}}^2 \ln^2\left(\frac{E}{E_{Z'}^{KNEE}}\right)\delta\gamma_K^2\right] \end{array}\right\}^{\frac{1}{2}}$$

where the meaning of the summations over Z and Z' is the same as in Eq. (5.8).

We have implemented Eqs. (5.8) and (5.9) into our computer simulation and we can therefore utilize the equivalent nucleon flux $\phi_N(E) \pm \delta\phi_N(E)$, coming from the WBM model, as the input for our simulation of prompt atmospheric neutrinos and muons. Before turning our attention to the leptonic fluxes, in Fig. 5.1 we simply compare the primary cosmic ray fluxes according to the different models discussed. In this figure we show the E^3-weighed equivalent nucleon fluxes, $E^3\phi(E)$, for the original TIG model of Eq. (5.3) and the WBM model of Eqs. (5.8) and (5.9). For the WBM model we show the "central" value flux of Eq. (5.8) as well as the error band obtained plotting $\phi_N \pm \delta\phi_N$.

It can be seen immediately that the fluxes of WBM are considerably lower than the TIG one, especially at the higher energies, beyond the knee(s), where the difference in the spectral index of the two models determines an overall discrepancy in the

fluxes up to one order of magnitude at the highest energy considered (10^{11} GeV). Even below the knee(s) the two models differ, although to a smaller extent, and of course also the position of the knee(s) is peculiar to the two models: TIG simplifies the knee as a sharp bend at $5{\cdot}10^6$ GeV while, as we have seen in Eq. (5.4), the change in slope is more gradual for WBM extending from $6{\cdot}10^5$ GeV to $1.68{\cdot}10^7$ GeV, even if the sharper bend is of course toward the lowest energy, where the most important components (H, He, etc.) are bent.

For the calculation of the prompt atmospheric fluxes the most relevant part of the primary spectrum is of course the one beyond the knee(s), at the highest energies. Since in this region WBM and TIG can differ up to one order of magnitude, we can already expect a similar difference in the leptonic fluxes. In the next section we will detail these results.

5.3 Prompt fluxes and spectral indices

We have used the WBM model of the primary spectrum to calculate the vertical prompt fluxes, both differential and integrated, for neutrinos and muons, and the related spectral indices, using the same simulation and procedures described in details in our first three parts. We recall that the main open option of our simulation is the choice of a set of partonic distribution functions (PDF's) and the low partonic momentum fraction (low x) extrapolation of the gluon PDF, regulated by the parameter λ, usually in the range between 0 and 0.5.

We choose here to present our results for just one of the most recent PDF sets, the MRST [31] with a variable λ, taking the values $\lambda = 0, 0.1, 0.2, 0.3, 0.4, 0.5$ and also the intermediate case that we denoted as $\lambda = \lambda(T)$ in Part Two. We just present here the ν_μ fluxes because, as usual, the ν_e and μ cases give essentially the

same results.

In Fig. 5.2 we show the E^3-weighed vertical prompt fluxes obtained using the WBM model of the primary cosmic rays (the central value of this model only, without considering the error band) and we compare them to the results (already reported in Part Two and Three) calculated using the TIG model for the primary cosmic rays. We detail here also the critical dependence on λ and also plot for completeness the conventional flux taken directly from the TIG model [15].

We see that, as expected, the results obtained with WBM are lower than the other ones and this difference is especially notable at the highest energies, where it can be as large as one order of magnitude at 10^9 GeV. Apart from the lower absolute values of the fluxes, the WBM results show the same features of our previous results, including the dependance on λ which is quite similar in the two cases. We can only notice slight differences in the shape of the fluxes, for the two cases, which are the product of the differences in slope, position of the knee(s), etc., that we have described in Fig. 5.1.

In Fig. 5.3 we reproduce the results of Fig. 5.2, but in terms of integrated fluxes which are more commonly used to evaluate signals and backgrounds for "neutrino telescopes". We present here the E^2-weighed integrated vertical prompt fluxes for the different cases and we compare them (as we did in our previous parts) to the number of particles simply traversing a km^2 2π sr detector in one year, in order to give an idea of the very low rates involved at these high energies. Again the use of the WBM primary fluxes basically lowers all our results by one order of magnitude at the energies where the prompt component dominates over the conventional one.

This of course would be a much desired result, reducing the atmospheric background for neutrino telescopes and allowing them to effectively gather data from astrophysical sources, like AGN's and others. On the contrary, in terms of the dis-

cussion over the possibility of setting bounds for λ with the neutrino telescopes, these new results are a serious setback: with such low atmospheric fluxes it will be probably difficult for the neutrino telescopes to give bounds on λ. Nevertheless we have tried in Fig. 5.4 to continue the discussion of a λ measurement.

In this final figure we compare the differential fluxes and the related spectral indices for two particular cases: the $\lambda = 0$ case, which is the fundamental one in our approach and the "intermediate" $\lambda = \lambda(T)$ case, just to show another example of the results (always using the MRST PDF). In the top part of the figure we plot again the E^3-weighed prompt fluxes obtained with the WBM and TIG primary models, but this time we include also the "error band" for the WBM case, i.e. the leptonic fluxes obtained using as an input the error band of the WBM primary flux shown in Fig. 5.1. This provides an estimate of the error of our final results due to the uncertainty of the WBM primary model: the error spread for the WBM leptonic fluxes amounts to a factor of two at around 10^6 GeV, where the prompt fluxes become relevant, and to a factor of about three at the highest energy considered (10^9 GeV). As we already noticed in Fig. 5.2 the WBM fluxes are always lower than those calculated with TIG, by almost one order of magnitude at the highest energies.

The related spectral indices are shown in the bottom part of the figures. In Part Two we argued that the spectral index α_{ν_μ}, for a prompt flux ϕ_{ν_μ}, is of the form

$$\phi_{\nu_\mu} \sim E^{-\alpha_{\nu_\mu}} \simeq E^{-b_{\nu_\mu}+\lambda}, \tag{5.10}$$

where $b_{\nu_\mu}(E)$ is just an energy dependent coefficient to be determined with our simulation in the $\lambda = 0$ case. We have seen in Part Three that b_{ν_μ} doesn't depend much on the PDF choice which can amount for a variation $\Delta b_{\nu_\mu} \simeq 0.02$, but shows

a larger uncertainty ($\Delta b_{\nu_\mu} \simeq 0.03 - 0.1$) due to our "calibration" of the charm production model.

Further more we have remarked that the linear relation

$$\alpha_{\nu_\mu} \simeq b_{\nu_\mu} - \lambda \tag{5.11}$$

holds with an uncertainty of about 0.03, so that, compounding all these errors, we evaluated the final uncertainty on λ to be (summing the errors linearly)

$$\Delta\lambda \simeq 0.08 - 0.15. \tag{5.12}$$

We should now consider also the uncertainty due to the primary cosmic ray flux. This can be seen from the bottom part of Fig. 5.4, especially in the left part for the $\lambda = 0$ case, where the plotted α_{ν_μ} gives directly b_{ν_μ}. We see that the spectral indices calculated with the WBM and TIG models can be rather different, as we have already noticed the different shape of the primary and leptonic fluxes. However, if we disregard the TIG model results and just consider the WBM as the most reliable model, we notice that the error band of WBM induces an additional uncertainty $\Delta b_{\nu_\mu} \simeq 0.1$, for energies in the range $10^6 - 10^8\ GeV$. We have therefore to include this error in our estimate of $\Delta\lambda$ which now we argue to be in the range (adding the errors linearly)

$$\Delta\lambda \simeq 0.18 - 0.25. \tag{5.13}$$

We can conclude that this analysis adds more difficulties to an actual measurement of λ with neutrino telescopes: the overall uncertainty is now somewhat around

$$\Delta\lambda \sim 0.2 \tag{5.14}$$

over a possible range for λ of 0.5; further more the fluxes calculated with WBM are now much lower than our previous estimates giving a very small atmospheric signal for the neutrino telescopes to observe.

5.4 Conclusions for Part Four

We have considered the dependance of our simulation for prompt atmospheric neutrinos and muons on the primary cosmic ray model. We have compared the cosmic ray flux we used so far, the same used by TIG, with one of the more recent models appeared in the literature: the WBM model. We have computed the equivalent nucleon flux coming from this model, together with the related uncertainty, and found it to be considerably lower than the TIG one for energies beyond the knee(s). As a consequence, all our differential and integrated prompt atmospheric fluxes are lowered, by almost one order of magnitude, in the region where the prompt flux dominates. Other features of the results, like the critical dependence on λ, appear to remain the same.

We have also detailed the uncertainty of the final fluxes due to the errors quoted in the WBM model; this uncertainty affects also the spectral indices of the fluxes, determining an increase of our previous estimate of the overall theoretical uncertainty for the measurement of λ, that we now argue to be about $\Delta\lambda \sim 0.2$. The relatively low fluxes obtained with this analysis, together with this new estimate of $\Delta\lambda$, indicate that "neutrino telescopes" will probably not be able effectively to set bounds for λ, unless the current uncertainties in our model can be reduced by new experimental data, either for the primary cosmic rays or the charm production

mechanism at high energy.

On the contrary, the lower atmospheric fluxes obtained here, would indicate a lower background for "neutrino telescopes", increasing their possibility of an effective detection of signals from astrophysical sources.

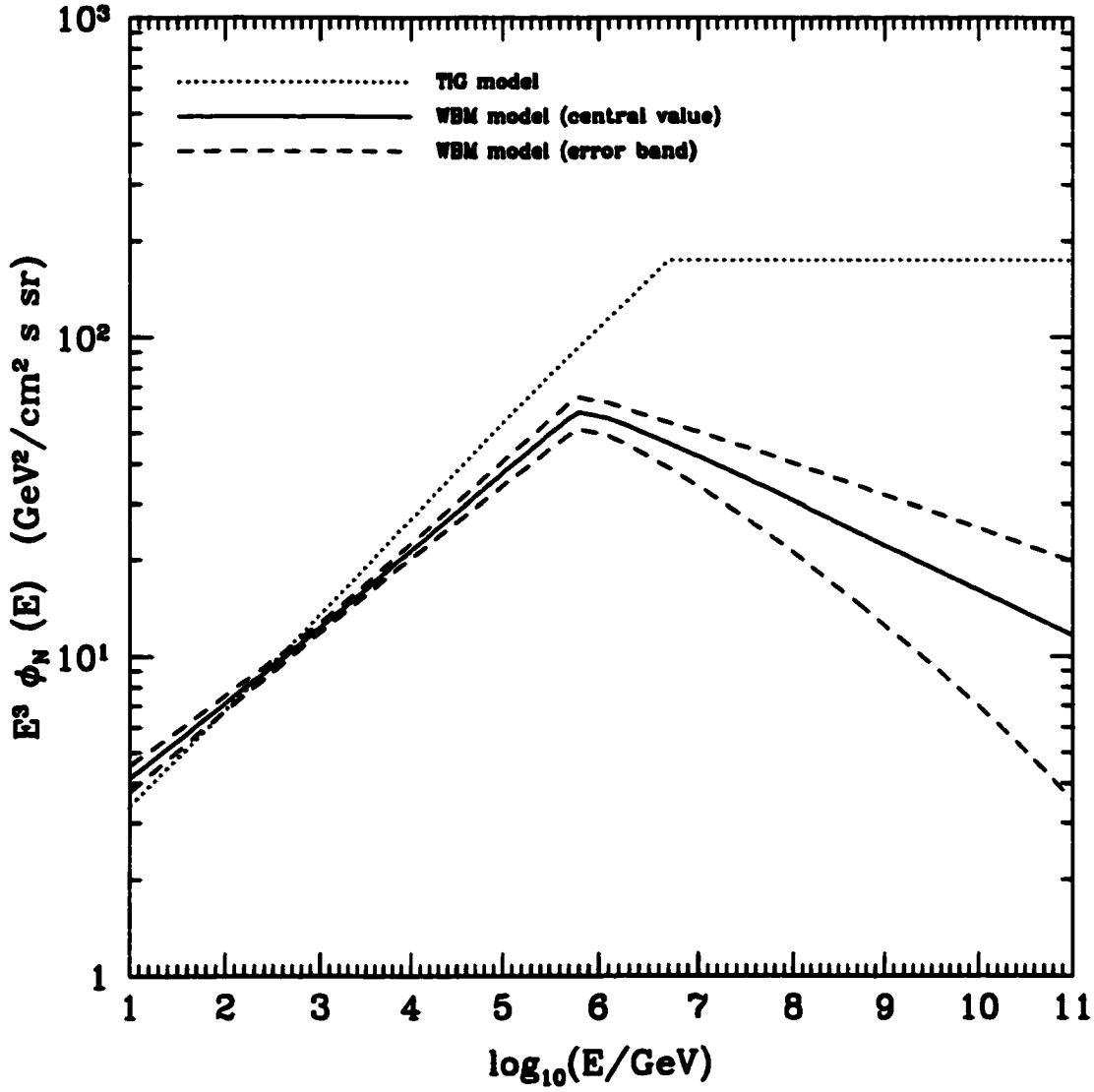

Figure 5.1: Primary cosmic ray models. We show the E^3-weighed equivalent nucleon fluxes for the models used: the TIG model and the WBM model (with related error band).

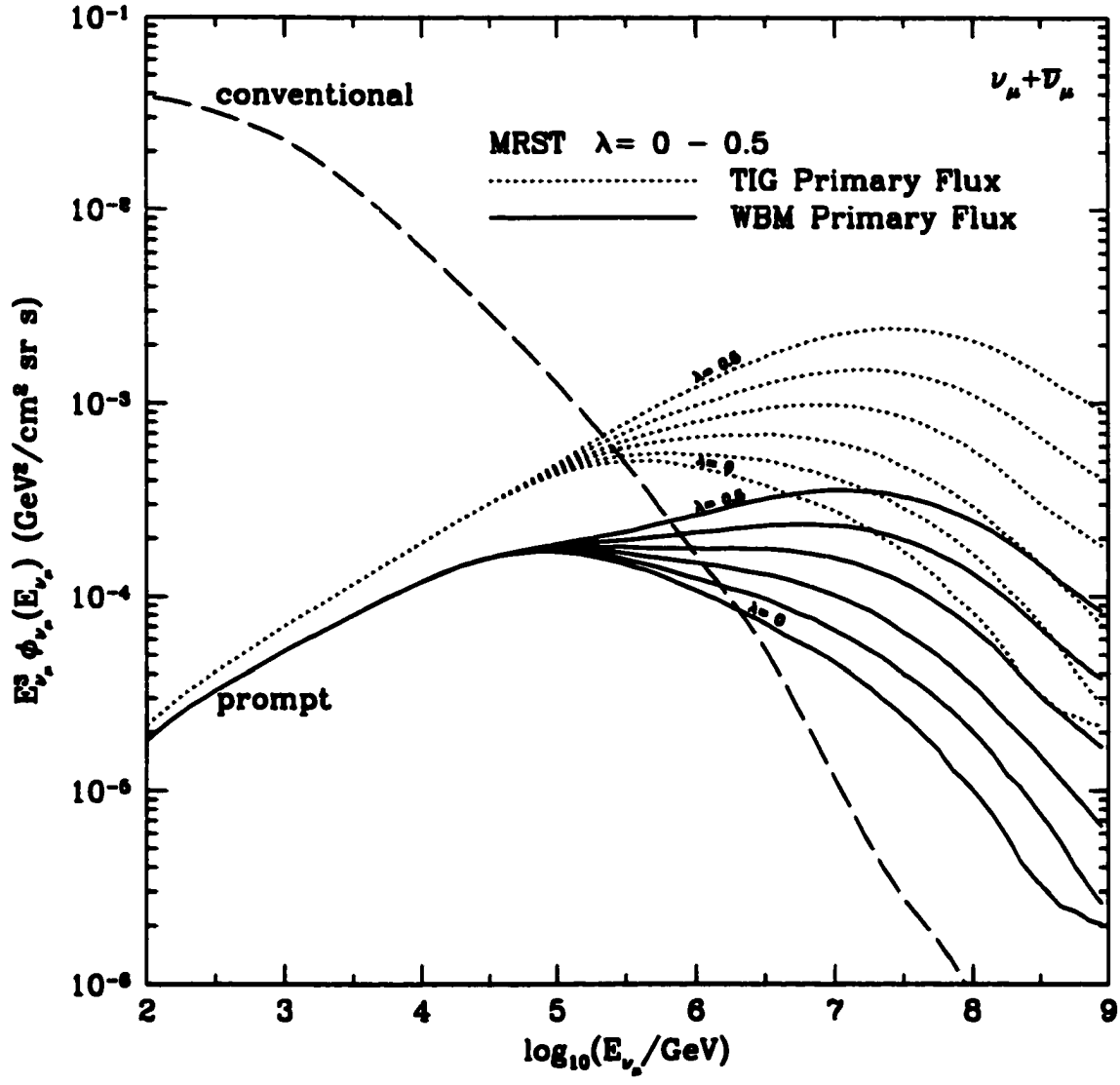

Figure 5.2: Results for MRST, $\lambda = 0 - 0.5$. E^3-weighed vertical prompt fluxes, at NLO, for muon neutrinos, are calculated using the TIG and WBM primary fluxes (also shown the conventional flux from the TIG model).

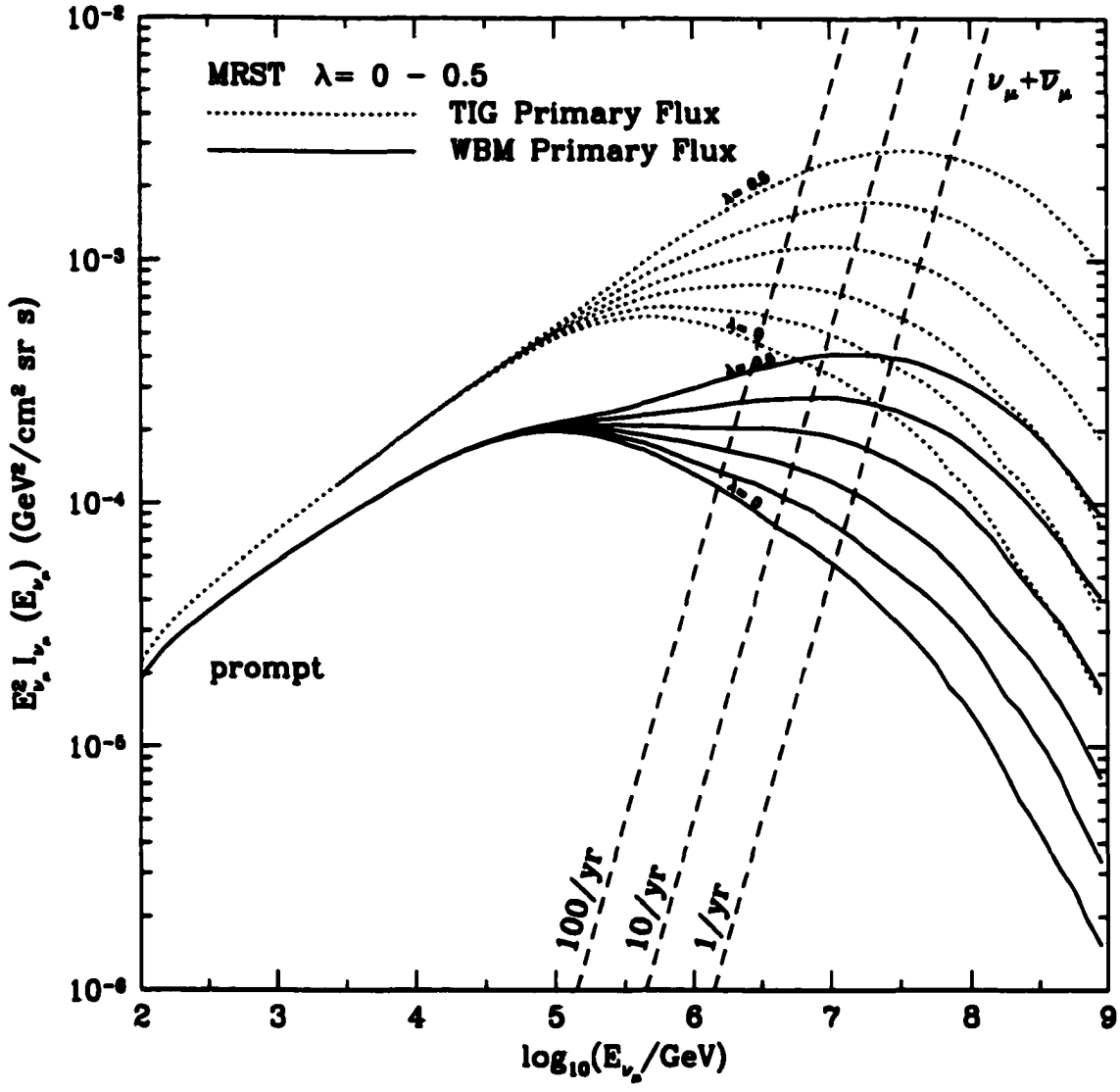

Figure 5.3: Results for MRST, $\lambda = 0 - 0.5$. E^2-weighed integrated vertical prompt fluxes, at NLO, for muon neutrinos, are calculated using the TIG and WBM primary fluxes. Also shown the number of particles traversing a $km^2\ 2\pi\ sr$ detector per year (dashed lines).

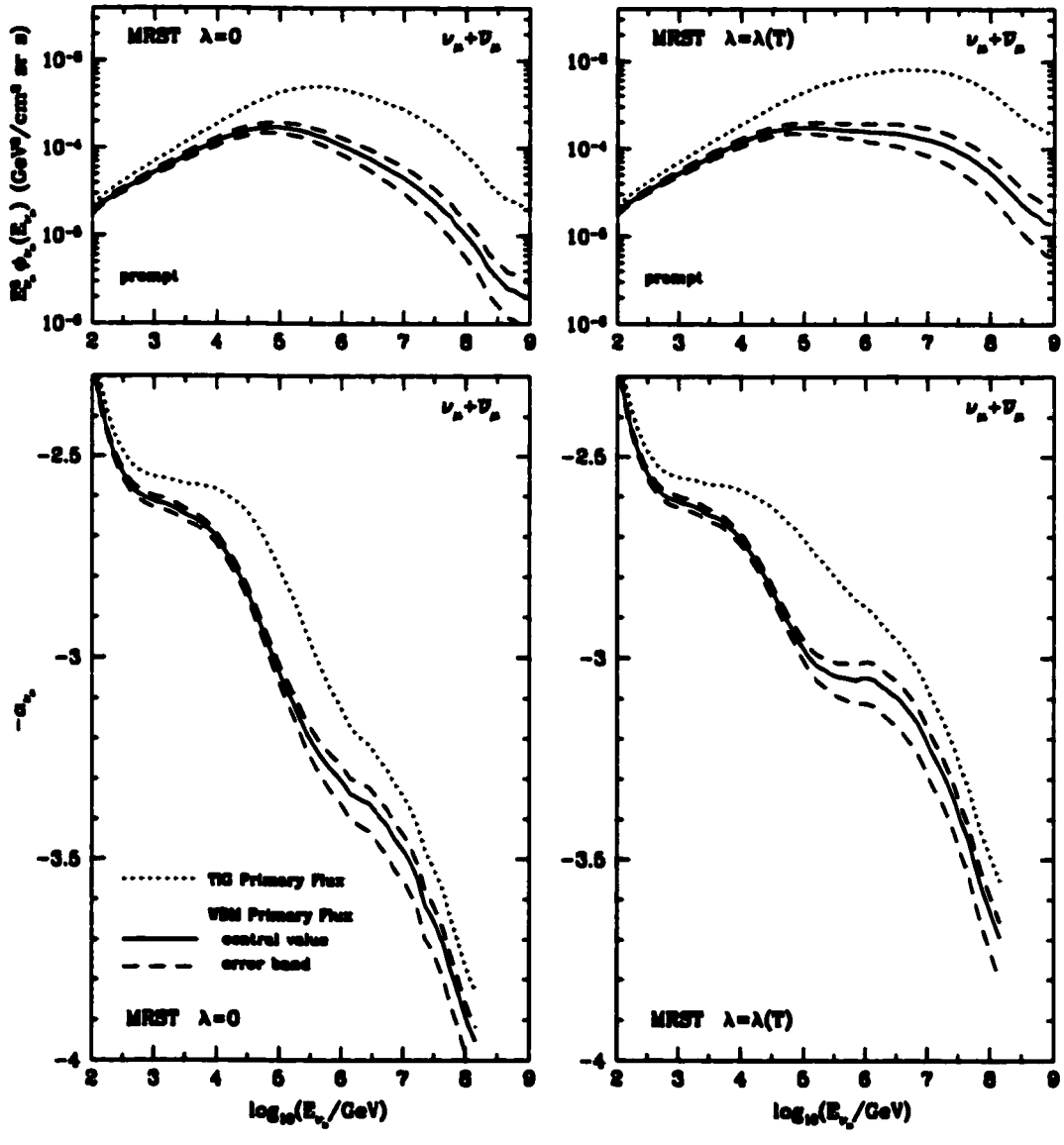

Figure 5.4: Results for MRST, $\lambda = 0$, $\lambda(T)$, calculated using the TIG and WBM primary fluxes (for the WBM model also the related error band is calculated). Top part: $E^3_{\nu_\mu}$-weighed vertical prompt fluxes, at NLO. Bottom part: related spectral indices $-\alpha_{\nu_\mu}$ (for the $\lambda = 0$ case $-\alpha_{\nu_\mu} = -b_{\nu_\mu}$).

Bibliography

[1] R. Wischnewski *et al.*, *Nucl. Phys. Proc. Suppl.* **75A**, 412 (1999); E. Andres *et al.*, preprint astro-ph/9906205; E. Andres *et al.*, preprint astro-ph/9906203; F. Halzen, preprint astro-ph/9904216; E. Andres *et al.*, *Nucl. Phys. Proc. Suppl.* **70**, 448 (1999); F. Halzen *et al.*, *Nucl. Phys. Proc. Suppl.* **77**, 474 (1999).

[2] V.A. Balkanov *et al.*, preprint astro-ph/0001151; V.A. Balkanov *et al.*, preprint astro-ph/0001145; V.A. Balkanov *et al.*, preprint astro-ph/9910133; C. Spiering *et al.*, *Nucl. Phys. Proc. Suppl.* **48**, 463 (1996).

[3] L. Trasatti *et al.*, *Nucl. Phys. Proc. Suppl.* **70**, 442 (1999); L. J. McNutt *et al.*, *Nucl. Phys. Proc. Suppl.* **48**, 469 (1996); L.K. Resvanis *et al.*, *Nucl. Phys. Proc. Suppl.* **35**, 294 (1994).

[4] F. Montanet *et al.*, preprint astro-ph/0001380; J.J. Hernandez *et al.*, *Acta Phys. Polon.* **B30**, 2283 (1999); P. Amram *et al.*, *Nucl. Phys. Proc. Suppl.* **75A**, 415 (1999).

[5] T.K. Gaisser, *Cosmic Rays and Particle Physics* (Cambridge University Press, Cambridge, England 1990).

[6] A. Kernan and G. Van Dalen, *Phys. Rep.* **106**, 297 (1984); S.P.K. Tavernier, *Rep. Progr. Phys.* **50**, 1439 (1987).

[7] H. Inazawa and K. Kobayakawa, *Progr. Theor. Phys.* **69**, 1195 (1983).

[8] E. Zas, F. Halzen, and R.A. Vázquez, *Astropart. Phys.* **1**, 297 (1993).

[9] E.V. Bugaev *et al.*, in *3rd NESTOR International Workshop*, Pylos, Greece, 1993, edited by L.K. Resvanis, p. 268.

[10] J.A. Appel, *Annu. Rev. Nucl. Part. Sci.* **42**, 367 (1992); S. Frixione, M.L. Mangano, P. Nason, and G. Ridolfi, *Nucl.Phys* **B431**, 453 (1994); P.E. Karchin, *LISHEP95*, Rio de Janeiro, 1995, FERMILAB-Conf-95.053-E; L. Rossi, *Nucl. Phys. B* (Proc. Suppl.) **50**, 172 (1996).

[11] E769 Collaboration, G.A. Alves *et al., Phys. Rev. Lett.* **77**, 2388 (1996).

[12] E769 Collaboration, G.A. Alves *et al., Phys. Rev. Lett.* **77**, 2392 (1996).

[13] WA92 Collaboration, M.I. Adamovich *et al., Nucl. Phys.* **B495**, 3 (1997).

[14] S. Frixione, M.L. Mangano, P. Nason, and G. Ridolfi, Report No. CERN-TH/97-16, hep-ph/9702287.

[15] M. Thunman, G. Ingelman, and P. Gondolo, *Nucl. Phys. B* (Proc. Suppl.) **43**, 274 (1995); P. Gondolo, G. Ingelman, and M. Thunman, *Nucl. Phys. B* (Proc. Suppl.) **48**, 472 (1996); M. Thunman, Ph.D. thesis, Uppsala University, 1996; M. Thunman, G. Ingelman, and P. Gondolo, *Astropart. Phys.* **5**, 309 (1996).

[16] E.V. Bugaev, V.A. Naumov, S.I. Sinegovsky, and E.S. Zaslavskaya, *Nuovo Cimento C* **12**, 41 (1989).

[17] C. Castagnoli *et al., Nuovo Cimento A* **82**, 78 (1984).

[18] M.C. Gonzalez-Garcia, F. Halzen, R.A. Vázquez, and E. Zas, *Phys. Rev. D* **49**, 2310 (1994).

[19] M.L. Mangano, P. Nason, and G. Ridolfi, *Nucl. Phys.* **B373**, 295 (1992); *Nucl. Phys.* **B405**, 507 (1993).

[20] P. Nason, S. Dawson, and R.K. Ellis, *Nucl. Phys.* **B303**, 607 (1988); *Nucl. Phys.* **B327**, 49 (1989); *Nucl. Phys.* **B355**, 260(E) (1990).

[21] L. Pasquali, M.H. Reno, and I. Sarcevic, *Phys. Rev. D* **59**, 034020 (1999).

[22] A.D. Martin, R.G. Roberts, and W.J. Stirling, *Phys. Lett.* **387**, 419 (1996).

[23] H.L. Lai *et al.*, *Phys. Rev. D* **51**, 4763 (1995).

[24] H.L. Lai *et al.*, *Phys. Rev. D* **55**, 1280 (1997).

[25] P. Harriman *et al.*, *Phys. Rev. D* **42**, 798 (1990); P. Sutton *et al.*, *Phys. Rev. D* **45**, 2349 (1992).

[26] J. Kwiecinski, A.D. Martin, and P.J. Sutton, *Phys. Lett. B* **264**, 199 (1991); *Phys. Rev. D* **44**, 2640 (1991); A.D. Martin, *Acta Phys. Pol. B* **25**, 256 (1994); J. Kwiecinski, *Phys. Rev. D* **52**, 1445 (1995).

[27] E.A. Kuraev, L.N. Lipatov, and V.S. Fadin, *Zh. Eksp. Teor. Fiz.* **72**, 377 (1977) [*Sov. Phys. JETP* **45**, 199 (1977)]; Ya.Ya. Balitsky, and L.N. Lipatov, *Yad. Fiz.* **28**, 1597 (1978) [*Sov. J. Nucl. Phys.* **28**, 822 (1978)].

[28] T. Sjöstrand, *Comput. Phys. Commun.* **82**, 74 (1994).

[29] K. Goulianos, *Phys. Rep.* **101**, 169 (1983).

[30] Particle Data Group, R.M. Barnett *et al.*, *Phys. Rev. D* **54**, 1 (1996).

[31] A.D. Martin, R.G. Roberts, W.J. Stirling, and R.S. Thorne, *Eur. Phys. J.* **C4**, 463 (1998).

[32] J.C. Collins, and R. K. Ellis, *Nucl. Phys. B* **360**, 3 (1991); R.K. Ellis, and D.A. Ross, *Nucl. Phys. B* **345**, 79 (1990); S. Catani, M. Ciafaloni, and F. Hautmann, *Nucl. Phys. B* **366**, 135 (1991).

[33] M.L. Mangano, Report No. CERN-TH/97-328, hep-ph/9711337.

[34] M.L. Mangano, LHC98 Workshop, CERN-TH (unpublished).

[35] CDF Collaboration, F. Abe *et al., Phys. Rev. Lett.* **79**, 584 (1997); *Phys. Rev. D* **56**, 3811 (1997); and references therein.

[36] L. Durand, and H. Pi, *Phys. Rev. Lett.* **58**, 303 (1987).

[37] Particle Data Group, C. Caso *et al., Eur. Phys. J. C* **3**, 1 (1998).

[38] LEBC-EHS Collaboration, M. Aguilar-Benitez *et al., Z. Phys. C* **40**, 321 (1988).

[39] ACCMOR Collaboration, S. Barlag *et al., Z. Phys. C* **39**, 451 (1988).

[40] LEBC-EHS Collaboration, R. Ammar *et al., Phys. Rev. Lett.* **61**, 2185 (1988).

[41] E653 Collaboration, K. Kodama *et al., Phys. Lett. B* **263**, 573 (1991).

[42] JACEE Collaboration, K. Asakimori, *et al.*, Astrophys. J. **502**, 278 (1998); UWSEA-PUB-95-07, in 24th International Cosmic Rays Conference (ICRC 95), Rome, Italy, 1995, p707, astro-ph/9509091.

[43] CASA-MIA Collaboration, M.A.K. Glasmacher, *et al., Astropart. Phys.* **10**, 291 (1999); *Nucl. Phys. B* (Proc. Suppl.) **75A**, 241 (1999).

[44] HEGRA Collaboration, F. Arqueros, *et al.*, astro-ph/9908202.

[45] B. Wiebel-Sooth, P.L. Biermann, and H. Meyer, *Astron. Astrophys.* **330**, 389 (1998).

[46] W. Rhode, T. A. Enßlin, and P. L. Biermann, astro-ph/9811361; P. L. Biermann, T. K. Gaisser, and T. Stanev, *Phys. Rev.* **D51**, 3450 (1995).